Characterization of Structure and Dynamics
of Submicrometric Systems
via Fluorescence Correlation Spectroscopy

Dissertation

zur Erlangung des Grades

Doktor der Naturwissenschaften

im

Fachbereich Physik, Mathematik und Informatik

der Johannes Gutenberg-Universität Mainz

vorgelegt von

Riccardo Raccis

geboren in Florenz, Italien

Mainz, im Dezember 2010

Die vorliegende Arbeit wurde am

Max-Plank-Institut für Polymerforschung in Mainz

unter Anleitung von

Prof. Dr. Wolfgang Knoll,

Prof. Dr. Georg Fytas,

Prof. Dr. Hans-Jürgen Butt,

Bernhard Menges und

Prof. Dr. Werner Steffen

in der Zeit von Oktober 2007 bis September 2010 angefertigt.

Dekan: Prof. Dr. Manfred Lehn

1. Berichterstatter: Prof. Dr. Hans-Jürgen Butt

2. Berichterstatter: Prof. Dr. Thomas Palberg

Übrige Mitglieder der Prüfungskommission:

Prof. Dr. Friederike Schmid

Prof. Dr. Thomas Basché

Tag der mündlichen Prüfung: 8. Dezember 2010

"There are more things in heaven and earth, Horatio,

Than are dreamt of in your philosophy."

- William Shakespeare, *Hamlet*

To Eva, and Mariona.

I miss you girls

Summary

1. List of abbreviations

BP	Benzophenone
C	Celsius, degrees
CMP	Counts per molecule
c_P	PNIPAAm concentration
c_R	Rh6G concentration
D	Diffusion coefficient
DLS	Dynamic Light Scattering
d_P	PNIPAAm-PNIPAAm center of mass distance
EDC	1-Ethyl-3-(3-dimethylaminopropyl)carbodiimide
ETA	Ethanolamine
FCS	Fluorescence Correlation Spectroscopy
g	Grams
Hz	Hertz
iOpal	Inverse opal
J	Joule
K	Kelvin, degrees
k_D	Dissociation constant
L	Liter
LCST	Lower critical solution temperature
m	Meter
M	mol/L
min	Minute
mol	Mole
MABP	4-benzoylphenyl methacrylate
n	Refractive index
N	Number of particles in the focal volume

NIPAAm	N-isopropylacrylamide
PBS	Phosphate buffered saline
PCS	Photon Correlation Spectroscopy
pI	Isoelectric point
PNIPAAm	Poly-N-isopropylacrylamide
PS	Polystyrene
R_A	$R_{HP} + R_{HR}$
R_H	Hydrodynamic radius
R_{HP}	PNIPAAm hydrodynamic radius
R_{HR}	Rh6G hydrodynamic radius
rWKB	Reversed Wentzel-Kramers-Brillouin
Rh6G	Rhodamine 6G
RPM	Rotations per minute
s	Seconds
SEM	Scanning electron microscopy
TEM	Transmission electron microscopy
TFPS	Sodium para-tetrafluorophenol-sulphonate
VLD	Vertical lifting deposition
V_{foc}	Focal volume
WKB	Wentzel-Kramers-Brillouin

2. Abstract

2.1. English version

The presented thesis revolves around the study of thermally-responsive PNIPAAm-based hydrogels in water/based environments, as studied by Fluorescence Correlation Spectroscopy (FCS).

The goal of the project was the engineering of PNIPAAm gels into biosensors. Specifically, a gamma of such gels were both investigated concerning their dynamics and structure at the nanometer scale, and their performance in retaining bound bodies upon thermal collapse (which PNIPAAm undergoes upon heating above 32 ºC).

FCS's requirements, as a technique, match the limitations imposed by the system. Namely, the need to intimately probe a system in a solvent, which was also fragile and easy to alter. FCS, on the other hand, both requires a fluid environment to work, and is based on the observation of diffusion of fluorescents at nanomolar concentrations. FCS was applied to probe the hydrogels on the nanometer size with minimal invasivity.

Variables in the gels were addressed in the project including crosslinking degree; structural changes during thermal collapse; behavior in different buffers; the possibility of decreasing the degree of inhomogeneity; behavior of differently sized probes; and the effectiveness of antibody functionalization upon thermal collapse.

The evidenced results included the heightening of structural inhomogeneities during thermal collapse and under different buffer conditions; the use of annealing to decrease the inhomogeneity degree; the use of differently sized probes to address different length scale of the gel; and the successful functionalization before and after collapse.

The thesis also addresses two side projects, also carried forward via FCS. One, diffusion in inverse opals, produced a predictive simulation model for diffusion of bodies in confined systems as dependent on the bodies' size versus the characteristic sizes of the system. The other was the observation of interaction of bodies of opposite charge in a water solution, resulting in a phenomenological theory and an evaluation method for both

the average residence time of the different bodies together, and their attachment likelihood.

2.2. German version

Die vorgelegte Dissertation beschäftigt sich mit dem Studium thermisch ansprechbarer, auf PNIPAAm-basierender Hydrogele in einer wässrigen Umgebung. Die dabei durchgeführten Untersuchungen fanden mit Hilfe der Fluoreszenz-Korrelations-Spektroskopie (FCS) statt.

Das Ziel dieses Projektes war die Implementierung von PNIPAAm-Gelen in Biosensoren. Hierbei wurde insbesondere eine Serie dieser Gele im Hinblick auf ihre dynamischen und strukturellen Eigenschaften auf der Nanometer-Skala und ihre Fähigkeit, angebundene Korpuskel im Falle des thermischen Kollapses festzuhalten, untersucht. Diesen durchläuft PNIPAAm im Falle einer Erwärmung über 32 °C.

Die Anforderungen an FCS als Technik entsprechen hierbei den durch das System verhängten Einschränkungen, das heißt die exakte Untersuchung eines Systems in einem Lösungsmittel, welches sowohl empfindlich als auch leicht veränderbar ist. Auf der anderen Seite benötigt FCS eine flüssige Umgebung zum Arbeiten und basiert auf der Beobachtung der Diffusion fluoreszierender Partikel in einer nanomolaren Konzentration. FCS wurde somit angewandt, um Hydrogele auf einer Nanometerskala minimalinvasiv zu untersuchen.

Die im Verlauf des Projektes adressierten Variablen beinhalteten unter anderem den Grad der Vernetzung, strukturelle Veränderungen und die Effektivität einer Antikörper-Funktionalisierung im Falle des thermischen Kollapses, das Verringern der Heterogenität und das Verhalten in unterschiedlichen Puffern und bei Verwendung unterschiedlich großer Probekörper.

Die Ergebnisse zeigen die Erhöhung der strukturellen Heterogenität während des thermische Kollapses und unter verschiedenen Pufferbedingungen, den Nutzen höherer Temperaturen während der Darstellung zur Verringerung der Heterogenität, die Verwendung verschieden großer Probekörper, um unterschiedliche Längenskalen des

Gels anzusprechen und die erfolgreiche Funktionalisierung vor und nach dem thermischen Kollaps.

Diese Dissertation geht des Weiteren auf zwei Nebenprojekte ein, welche ebenfalls mit FCS durchgeführt wurden. Zum einen führte die Beobachtung der Diffusion in inversen Opalen zu einem Simulationsmodell für die Diffusion von Korpuskeln in begrenzten Systemen, welche vom Verhältnis des Körpergröße zu den charakteristischen Dimensionen des Systems abhängt. Zum anderen beschäftigte sich das zweite Nebenprojekt mit der Wechselbeziehung zwischen Korpuskeln unterschiedlicher Ladung in einer wässrigen Lösung. Dies führte zu einer phänomenologischen Theorie und einer Auswertungsmethode für die durchschnittliche gemeinsame Verweildauer verschieden großer Korpuskel und die Wahrscheinlichkeit ihrer gegenseitigen Anlagerung.

3. Introduction and motivation

The worlds of material science and current-generation technology development are linked to each other more and more as time progresses. For technology, highly specialized scientific research has become a base necessity, as the high performances and very specific properties required for novel outlets in product development can only be provided by refined material engineering; and for the research, technology development offers both a practical incentive in the form of funding, and a source of inspiration for new directions to take.

As common experience suggests, easier things are achieved sooner. Thusly, new advancements in material synthesis follow a direction towards increased structural complexity and finesse. Of course, material synthesis is only half of the process, characterization of the new systems being the other, which leads to further refinement of the next synthesis iterations, and so forth in the familiar life cycle of research.

Some systems present especially specific challenges for characterization, calling for equally specialized measurement techniques. Some of such techniques are themselves situated in the experimental field of study, in their implementation and data interpretation if not in their practical application. For these, the development of a more precise data analysis theory may be of great benefit, and specific cases and effects can be addressed to further refine future data analysis. Finally, the limits of the said techniques can be tested on especially unusual study subjects, to address fine-scale material analysis of processes otherwise measurable with more traditional methods.

Possible outlets such as described in the previous paragraph form the study subject of the present thesis, the core of which is Experiment 3 (Section 8, page 117). In Experiment 3, the physical properties of water-swollen poly-N-isopropylacrylamide (PNIPAAm) hydrogels are investigated on the nanometric scale, the aim being the refinement and implementation of said hydrogels for biosensing applications.

In biosensors, a population of one or more specific biological receptors (usually antibodies) is permanently attached to a three-dimensional permanent matrix, in which a solvent (most often of biological nature) is diffused, which contains specific to the

receptors the matrix is functionalized with. The presence of the targeted body in the matrix is then evidenced by measuring the difference in specific properties of it, such as the refractive index *n* by means of a small surface plasmon resonance (SPR) apparatus, between the matrix before and after entrapping the targeted body.

Stimuli-responsive ("smart") hydrogels[1] are permanent polymer networks capable of imbibing huge quantities of water. Hydrogels are formed by permanently, chemically binding ("crosslinking") highly hydrophilic polymer chains.

The implementation of smart hydrogels as biosensors[2,3,4,5,6] has a twofold advantage: first, said gels' capability of collapsing to almost dry thickness under specific stimuli can be used to squeeze diffusing bodies other than the targeted ones - now bound to the functionalization sites - out of the gel; second, the same mechanism allows for the bound, targeted bodies to achieve a high concentration in the collapsed gel, thusly enhancing the biosensor's sensitivity. Both effects are shown in Fig. 1 below.
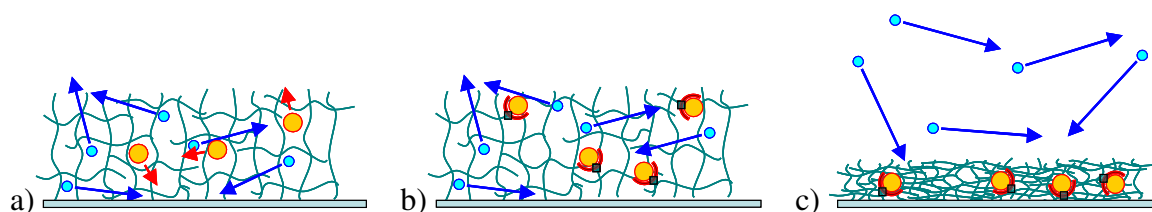
Fig. 1. Working principle of a smart hydrogel based biosensor. a) Swollen gel in biological solution: various bodies diffuse through; b) swollen functionalized gel: a specific kind of body is entrapped; c) stimulus-collapsed functionalized gel: bodies are expelled except the specific body, which is entrapped and in a high concentration. Both specificity and high sensitivity are achieved

In the case of the gel at the center of this thesis, PNIPAAm, the stimulus causing the collapse is a lower critical solution temperature of 32 ℃ in water, making the collapse achieved simply by moderate heating. As reported in literature[7,8,9,10,11], PNIPAAm switches to hydrophilic to hydrophobic upon heating above 32 ℃. In a solution, this causes phase separation. In a permanent network like a hydrogel is, this tendency is paired with the bounds of the permanent structure, causing the aforementioned collapse.

The aim of this thesis presented a challenge, since the structure we needed to investigate was very fine (mesh size being on the nanometer scale range), of a non

necessarily trivial geometry, fragile, charged, and required to be observed in a fluid with minimal invasivity.

A solution to the narrow conditions above came from the application of Fluorescence Correlation Spectroscopy (FCS), a method to study the average diffusional mobility of fluorescent bodies in solution.

By using FCS, and diffusing nanometer-sized fluorescent probes in the gels, we could deduce the gels' structure via a method that is essentially complementary to the imposed limitations, since it requires a fluid environment to be applied and relies on the diffusion of small bodies in expressly small numbers (the optimal concentration for a good signal is in the nM concentration range).

Although FCS has been in recent years used for environmental probing similar[12] to what we performed, such application itself can be said to constitute an experimental method, since although diffusion theory itself dates back to the Einstein age, it has been mostly used to characterize diffusant bodies in well-known environment[13] - pure solvents or buffer solutions - to detail biological and/or chemical interactions[14,15,16,17,18,19], and diffusing bodies' conformational changes[20]. In this respect, what we applied was an inversion of the more traditionally established use: probing an unknown environment with known, non-interacting diffusants.

More specifically, we wanted to observe diffusion of monodisperse, nanometer-sized fluorescents in the swollen gels, being slowed down by the polymer chain-crowded environment. In this context, we wanted to observe such slowdown devoid of additional interactions, chief of which electrostatic ones. This lead to a further narrowing of experimental conditions (fluorescent probes being chosen as feebly repelling each other and gel chains) on one hand, and on the other to a study of what a heavily (positively) electrostatically interacting system would look like. To the latter end, we simplified the experimental conditions, and investigated via FCS solutions of the heavily charged Rhodamine 6G dye (Rh6G) and uncrosslinked PNIPAAm chains in various solvent mixtures. This constituted Experiment 1, and is described in section 6, page 47.

Also, an attempt was made to build a basic, self-consistent theory of non interacting probe diffusion in crowded environment, thus attempting to establish the relationship between probe size, typical sizes of the probed environment, and probe mobility. To do

this, we studied the diffusion of fluorescents ranging one order of magnitude in size in ordered inverse opals via FCS, whose characteristic sizes and structure we knew. The characteristics of diffusants and environment both being fixed, we used this experiment, Experiment 2, to build a theory of slowed down diffusion (section 7, page 97).

The present thesis shows how a relatively insular method like FCS can be applied to an extensive degree to investigate complex systems and obtain a model thereof. This fulfills an aim of (relative) simplicity - to derive complex informations mostly through a single method, with little additional contribution from other techniques - and non-invasivity.

4. FCS: general theory and practical application

4.1. Theory

The term Correlation Spectroscopy describes the ensemble of techniques aimed at extracting sets of data (the aforementioned spectra) from the analysis of correlation of signals. Of these, the most widespread use is correlation of light signals. Dynamic Light Scattering (DLS), also referred to as Photon Correlation Spectroscopy (PCS), is historically the basis for and provides the foundation for the general theory.

In correlation spectroscopy, the time-dependent, recorded intensity from a signal is multiplied by the recorded intensity from a second signal (a reference signal in the case of *heterodyne* spectroscopy, the same signal in the case of *homodyne* spectroscopy, also referred to as *autocorrelation*) delayed by a time τ. The result is then integrated over all measured time intervals and normalized to the total measurement time. For a homodyne correlation experiment, the autocorrelation is thusly provided by

$$\left\langle A(t_0)A(t_0+\tau)\right\rangle = \lim_{T\to\infty}\frac{1}{T}\int_{t_0}^{t_0+T}A(t)A(t+\tau)dt \tag{4.1}$$

where t_0 is the integration starting point and T is the total measurement time. Such expression provides an expression of the average tendency of the signal to keep similar to itself as a function of the delay time τ. Under general, stationary conditions, the result is independent of t_0, and therefore the autocorrelation becomes purely a function of τ:

$$\left\langle A(0)A(\tau)\right\rangle = \left\langle A(t_0)A(t_0+\tau)\right\rangle = \lim_{T\to\infty}\frac{1}{T}\int_0^T A(t)A(t+\tau)dt \tag{4.2}$$

In PCS, $A(t)$ is the light intensity, $I(t)$, from a laser light being scattered by an ensemble of particles in a transparent liquid. Such a signal will be comprised by an average scattered intensity, plus random fluctuations due to the particles entering and exiting the illuminated volume:

$$A(t) = I(t) = \langle I \rangle + \delta I(t) \tag{4.3}$$

Naturally, the larger the average $\langle I \rangle$, the less relevant the fluctuations $\delta I(t)$. A simple calculation[21], however, shows how

$$\langle I(0)I(t) \rangle = \langle \delta I(0)\delta I(t) \rangle + \langle I \rangle^2 \tag{4.4}$$

In other words, the desired information is contained in the fluctuations, and the average simply defines a baseline. Furthermore, the smaller $\langle I \rangle$ is, the better $\delta I(t)$ can be recorded. This characterizes correlation spectroscopy, and autocorrelation in particular, as a way to obtain information from noise, and possibly the only technique where source signals are desired to have a high *noise to signal* ratio. The optimal concentration is 1 particle per focal volume at any given time.

The larger part of PCS is performed under the *dilute solution* regime. That is, we assume the solution to be diluted enough not only to consider particle interactions negligible, but also to have each scattered photon being scattered by a single body (*single scattering* regime). Under these assumptions, $I(t)$ is linearly dependent on the diffusants concentration c. c, in turn, is linearly dependent on the average diffusants number in the illuminated volume. Rewriting the previous formula in normalized form yields:

$$\frac{\langle I(0)I(t) \rangle}{\langle I \rangle^2} = \frac{\langle I(0)I(t) \rangle}{\langle I(0)I(0) \rangle} = \frac{\langle \delta I(0)\delta I(t) \rangle}{\langle I(0)I(0) \rangle} + 1 = \frac{\langle \delta n(0)\delta n(t) \rangle}{\langle n(0)n(0) \rangle} + 1 \tag{4.5}$$

The expression above represent the most general formulation of the *autocorrelation function*, $G(t)$.

FCS theory has its basis in PCS theory, the difference lying in the source of the employed signal and the experimental setup's resulting geometric characteristics. As

depicted in Fig. 2 below, FCS signal is generated by focusing laser light in the region to be probed.
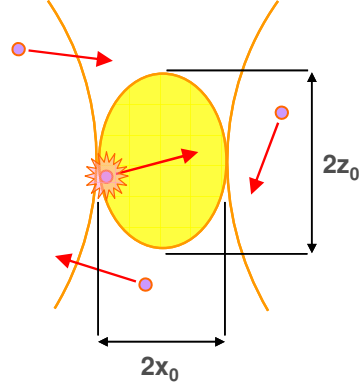
Fig. 2. Scheme of diffusion of fluorescents through the focal volume (yellow). Diffusants' entering and exiting the volume generate $I(t)$ fluctuations. Reported also are the dimensions of the focal volume as per standard FCS terminology

The resulting *focal volume*, located at the laser's waist, is the region of maximal intensity, which can be described with a three-dimensional Gaussian distribution:

$$I(\vec{r}) = I_0 e^{-\frac{x^2+y^2}{2\sigma_1^2}} e^{-\frac{z^2}{2\sigma_2^2}} \tag{4.6}$$

where σ_1 and σ_2 are the distribution's widths respectively in the z axis and the x-y plane. The emitted light, $I_f(t)$, is then recorded and autocorrelated. As in PCS, it is a direct function of the concentration:

$$I_f(t) = Q\varepsilon \int I(\vec{r})c(\vec{r},t)d^3r \tag{4.7}$$

In the former, Q and ε are respectively the fluorescent probes' quantum efficiency and extinction coefficient, and $c(\vec{r},t)$ is of course their concentration. As for the dilute solution regime assumption, the analogous still stands while being founded on a different physical basis - while in PCS we assume a single scattering process per photon, in FCS

we have, as physical fact, that each fluorescence photon is - naturally - to be emitted by one single body. In this respect, FCS hinges on a more solid principle than PCS does.

Applying now the general $G(t)$ formulation to FCS, we have that

$$G(t) = \frac{\left\langle \delta I_f(0) \delta I_f(t) \right\rangle}{\left\langle \delta I_f(0) \delta I_f(0) \right\rangle} \tag{4.8}$$

A brief calculation of which yields

$$G(t) = \frac{\int |I(\vec{q})|^2 F(\vec{q},t) d^3 q}{\int |I(\vec{q})|^2 F(\vec{q},0) d^3 q} \tag{4.9}$$

where $I(\vec{q})$ is the spatial Fourier transform of $I(\vec{r})$ and $F(\vec{q},t)$ the correlation functions of the spatial Fourier transform of the concentration fluctuations.

Under the assumption of concentration fluctuations purely due to particle diffusion in and out of the focal volume we have

$$F(\vec{q},t) = \left\langle \delta c^*(\vec{q},0) \delta c(\vec{q},t) \right\rangle = \left\langle |\delta c(\vec{q},0)|^2 \right\rangle e^{-q^2 D t} \tag{4.10}$$

where D is a particle's self-diffusion coefficient, defined in Fick's Law:

$$\left(\frac{\partial c}{\partial t} \right)_x = D \frac{\partial}{\partial x} \left(\frac{\partial c}{\partial x} \right)_t \tag{4.11}$$

D can be expressed by the Stokes-Einstein formula as $D = \dfrac{k_B T}{6 \pi \eta a}$, where k_B is Boltzmann's constant, T the temperature in Kelvin degrees, η the solution's viscosity (usually in Centipoises) and a the particle's radius (usually in cm).

For $I(\vec{q})$ we have:

$$I(\vec{q}) = (2\pi)^{\frac{3}{2}}\left(\sigma_1{}^2\sigma_2\right)I_0 e^{-\frac{1}{2}\left(q_x{}^2+q_y{}^2\right)\sigma_1{}^2} e^{-\frac{1}{2}q_z{}^2\sigma_1{}^2} \tag{4.12}$$

Factoring now $I(\vec{q})$ and $F(\vec{q},t)$ into the expression for $G(t)$ and integrating, one arrived to the general expression for the autocorrelation function in FCS:

$$G(t) = 1 + \frac{1}{N}\frac{1}{\left(1+\dfrac{t}{\tau_D}\right)\sqrt{1+\dfrac{t}{S^2\tau_D}}} \tag{4.13}$$

In the above, N is the average number of fluorescents present at any given moment in the focal volume, τ_D is the average diffusion time of a single fluorescent through the focal volume, and S is the structural parameter of the focal volume, that is the ratio between its axial and radial dimensions, as in $S = \dfrac{z_0}{x_0}$. z_0 and x_0 are the common denominations used in FCS for same quantities we previously referred to as σ_2 and σ_1, and respectively describe the half-thickness and half-width of the focal volume.

x_0 in particular is of crucial importance for the determination of the observed fluorescents' diffusion coefficient, D. Given the nature of the signal observed, it is impossible for the experimenter to observe a fluorescent's trajectory inside the focal volume: only the moments when it starts to fluoresce and when it stops are available as information. Additionally, since the z-axis of the focal volume is - naturally - coincident with the axis of the objective, the z-contribution of the observed diffusion is not accessible. D can, however, be very simply calculated from the measured τ_D through the expression

$$D = \frac{x_0{}^2}{4\tau_D} \tag{4.14}$$

To this end, x_0 needs to be known. On a practical level, as the system is extremely sensitive, calibration is routinely performed before every measurement session by measuring τ_D for a known fluorescent in a known solvent at a known T, therefore allowing the experimenter to calculate the known fluorescent's D via the Stokes-Einstein equation and, through (4.14), easily calculate the system's x_0 for the measurement session.

Noteworthy is the fact that z_0 doesn't factor into the expression for D, neither explicitly or implicitly through S. In this sense, x_0 represents in FCS the statistically average *half-length a fluorescent diffuses through during its diffusion time*. In other words, one can think of diffusion of fluorescents through the focal volume in two ways: 1) the real-life case: diffusion through the whole possible gamma of sections of the ellipsoid the focal volume consists of; or 2) a schematized case: diffusion through the center of a sphere of radius x_0.

Alternatively, the autocorrelation can be found expressed without baseline:

$$G'(t) = \frac{1}{N} \frac{1}{\left(1 + \dfrac{t}{\tau_D}\right)\sqrt{1 + \dfrac{t}{S^2 \tau_D}}} \tag{4.15}$$

or, after the previous passage, normalized to unity:

$$C(t) = \frac{1}{\left(1 + \dfrac{t}{\tau_D}\right)\sqrt{1 + \dfrac{t}{S^2 \tau_D}}} \tag{4.16}$$

The previous are described in literature in different ways. In the present thesis, $G(t)$, $G'(t)$ and $C(t)$ will be used to indicate them. Additionally, $C(t) + 1$ will be utilized, in order to compare curve independently of N, but without excluding the baseline feature. To this, I'll be referring to as normalized $G(t)$.

Multiple monodisperse populations can easily be detected at the same time, each characterized by a τ_D. The result is pretty straightforward, and the FCS autocorrelation function is generalized into:

$$G(t)=1+\frac{1}{N}\sum_{i=1}^{n}\frac{F_i}{\left(1+\dfrac{t}{\tau_{Di}}\right)\sqrt{1+\dfrac{t}{S^2\tau_{Di}}}} \tag{4.17}$$

Notice that, in the previous, N refers to the total average number of particles in the volume. The number belonging to the i-th population, or more generally involved in the i-th diffusion process, is given by

$$N_i = NF_i \tag{4.18}$$

Finally, a number of non-diffusive effects can add up to the measured $G(t)$. The most common for molecular, dipole-based fluorescents such as the ones employed in the presented set of experiments is the *triplet* effect, in which a fraction of the fluorescent population's is excited from ground state to triplet state rather than singlet state. Since triplet state excitation is forbidden by quantum mechanics, a flickering is generated in the emitted fluorescence due to the longer time required for the fluorescent to relax to the ground state.

Autocorrelation theory posits a general[21] treatment of $G(t)$ in chemically active systems, which has been adopted[21,22] into common practice to model the triplet artifact. Conceptually, the triplet effect is treated as a chemical reaction inducing non-translational fluctuation on $c(t)$. As a result, under the assumption that the fluorescents' diffusion is not altered by intrinsic effects such as triplet, it is possible to separate the overall $G'(t)$ into independent contributions[23,24]:

$$G'_{total}(t) = G'_{motion}(t) X(t)$$

where $X(t)$ is the autocorrelation function for the fluorescents' intrinsic, non-translational signal. For triplet, the result is given by

$$X(t) = 1 - T_r + T_r e^{-\frac{\tau}{\tau_T}} \tag{4.19}$$

where T_r is the fraction of particles affected and τ_T the triplet's relaxation time. The above is usually applied in normalized form to have it display a baseline of 1:

$$X(t) = \frac{1 - T_r + T_r e^{-\frac{\tau}{\tau_T}}}{1 - T_r} = 1 + \frac{T_r}{1 - T_r} e^{-\frac{\tau}{\tau_T}} \tag{4.20}$$

The established autocorrelation fit formula for dipole-based fluorescents is therefore

$$G(t) = 1 + \frac{1}{N} \left(\sum_{i=1}^{n} \frac{F_i}{\left(1 + \frac{t}{\tau_{Di}}\right)\sqrt{1 + \frac{t}{S^2 \tau_{Di}}}} \right) \left(1 + \frac{T_r}{1 - T_r} e^{-t/\tau_T}\right) \tag{4.21}$$

The typical time scale for the triplet effect is 0.1 to 10 µs, which makes it well distinct from the diffusional slope of most systems, and thusly easily accounted for.

Other non-diffusive effects of note are rotational fluctuations (typically 10 ns – 0.1 µs) and antibunching (~ ns and below). The first is generated by fast-time dipole rotation; the second, by the intrinsic statistics of the fluorescents emission. Since the FCS setup by us employed has a first detectable τ of 0.2 µs, these two effects are of marginal concern to us.

It is also common practice, such as it normally was during the run of the presented experiments, to exclude the initial points from an autocorrelation curve's fitting, in order to avoid accounting for non diffusive processes.

4.2.   Practical application

Given the discrete nature of both the signal from the discriminator, and of the correlation process itself, the $\langle I(t)I(t+\tau)\rangle = \lim_{T\to\infty}\frac{1}{T}\int_0^T I(t)I(t+\tau)dt$ integral is approximated with a discrete succession of M channels, each the product of light intensity sampled at times t and $t+\tau_j$, with $j = 1, 2, 3, \ldots , M$.

The intensity is expressed through the number of impulses to the correlator, the product mentioned above is performed between the n_i impulses in the sampling interval centered around t and the n_j impulses in the sampling interval around $t+\tau_j$:

$$G(\tau_j) = \left(n_1 n_{1+j} + n_2 n_{2+j} + \ldots + n_{N-j}n_N\right)\frac{1}{N-j} = \frac{1}{N-j}\sum_{i=1}^{N-j}n_i n_{i+j} \qquad (4.22)$$

with N the total number of samplings.

The basic assumption of FCS - random intensity fluctuations around an average - implies an average number of particles during the measurement. For this reason, it is essential to consider systems at their thermal, chemical and mechanical equilibrium.

Additionally, and similar to the previous, practical implementation of FCS hinges on the assumption that the on-off signal of fluorescents be determined purely by their diffusion time in the focal volume, plus intrinsic fluorescent fluctuations (such as triplet effect). In other words, we assume each particle to be spending small enough a time in the focal volume so as not to be bleached. This assumption, although easily met by the diffusional processes in our experiments (particles diffusion times being in the 10^{-5} - 10^{-3}

s range) comes to fall when observing entrapped fluorescents (section 8.3.2.2, page 156). However, although traditionally a hindrance for FCS, the bleaching effect observed in such cases can be used to further estimate the gel properties, and was in the specifically presented cases actively sought.
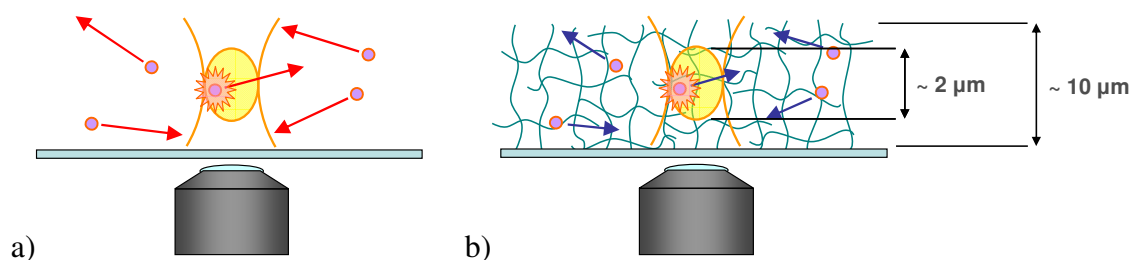

Fig. 3. Practical implementation of FCS. a) Diffusion in a measurement chamber. Bottom to top: inverted microscope objective; glass slide / disposable chamber bottom; solvent in which fluorescents' diffusion is measured. b) Application of a) to a complex system (a hydrogel in this example, as will be seen in Experiment 3). Typical $2z_0$ size is reported. If smaller than the overall size of the system, the system can be studied as an average. Also reported is an example of the typical size of the systems studied. Notice fluorescents diffusing slower in b) than in a), as denoted by the shorter arrows. This difference can be exploited to drive information about the system, and is the basis of the treated Experiments

Practically, all the experiments reported in the present thesis hinge on the comparison between the mobility of fluorescent tracers (also referred to as probes, diffusing bodies, fluorescents) in a pure solvent versus their mobility slowed down by the systems being studied. Namely, the experimentally determined altered diffusion coefficient, D, of the probes will be compared to the unaltered free solvent diffusion coefficient, also experimentally determined. Based on these data, the treatment of Experiments 1 (section 6, page 47) and 2 (section 7, page 97) focuses on deriving analytical methods and predictive models of a general nature, while in the case of Experiment 3 (section 8, page 117), which comprises the original motivation for this project, the focus is shifted on adopting previously established models to the study of a specific system.

The basics of the experimental process are exemplified in Fig. 3 for what will be described in the treatment of Experiment 3. Experiments 2 and 3 present experimental conditions in which the altered mobility is determined by diffusion in a complex, non-

interactive environment (inverse opal in Experiment 2, PNIPAAm-based hydrogel in Experiment 3), in which therefore the statistical presence of obstacles cause a systematic deflection of the probes' Brownian motion and, as a consequence, an increase of the average diffusion time / diffusion coefficient. In Experiment 1, on the contrary, the probes diffuse in the absence of a fixed structure, and the diffusion alteration is determined specifically by interaction with a non-fluorescent population, also in solution (PNIPAAm).

The entirety of experiments treated in the present thesis was conducted via FCS or, in case of Z-scan measurements, via the same FCS setup as used for the FCS measurements. Additional measurements, such as the SPR-based, were performed by colleagues as referenced to in the thesis, and references are provided for the specific techniques for a better comprehension, the detailed explanation of which is beyond the scope of this thesis.

5.   Experimental ensemble

5.1.   FCS setup

All measurements were performed on a commercial FCS setup (Carl Zeiss, Jena, Germany) consisting of the module, ConfoCor 2, and an inverted microscope, Axiovert 200 model. A 40x Plan Neofluar objective (numerical aperture 1.2; working distance 0.29 mm) and MilliQ water (filtered through a MilliQ purifaction system, resistivity 18.2 MΩ cm) as immersion liquid were used the described Experiments.

Laser light was focused in a three-dimensional Gaussian focal volume, and the emitted fluorescence recorded and autocorrelated. The fluorescence species were excited by three different lasers depending on the Experiments.

Experiment 1 (section 6, page 47) required the use of a single laser to excite Rhodamine 6G (Rh6G), for which a HeNe laser was employed providing a wavelength λ = 543 nm.

Experiment 2 (section 7, page 97) and 3 (section 8, page 117) required the use of a more complex setup, involving two separate wavelengths to excite two different fluorescent populations diffusing at the same time. For these Experiments, a He-Ne laser emitting at λ = 633 nm (Cy5 for calibration, Alexa 647 for measurement) and an Argon ion laser emitting at λ = 488 nm (Rh6G for calibration, Qdots for measurements in Experiment 2, GFP for measurement in Experiment 3) were employed.

In Experiment 2 and 3, both lasers were in use at the same time for measurements involving two tracers, and both tracers were diffused in the same session. However, even if signals from the two probes could be measured simultaneously, it was preferred to measure them one at the time, shutting close the laser corresponding to the probe not being measured. This was done in order to eliminate the little, but otherwise present, cross-talk between the two measuring channels. Thusly, for the case of simultaneous two-probe measurement, different probe diffusion was recorded in the same spot but at slightly delayed times. The emission was collected after splitting the signal by means of a NFT635 dichroic mirror, and filtering with a long-pass LP655 filter for the fluorescence

light from the $\lambda = 633$ nm excitation (channel 1) and with a band pass filter (BP560-615) for the fluorescence light from the $\lambda = 488$ nm excitation (channel 2). For detection, avalanche photodiodes capable of single-photon counting were employed.

5.2. Chambers

The chambers employed were NUNC disposable chambers for Experiment 1 (section 6, page 47), and reusable steel Attofluor chambers (cat. no. A7816) for Experiment 2 (section 7, page 97) and 3 (section 8, page 117). Assistant glass slides (cat. no. 1001/25, 25 mm diameter, 160 μm thickness) supporting the inquired environment (hydrogels, iOpals) were mounted in the Attofluor chambers. In order to prevent solvent evaporation during Experiments 2 and 3 the sample chamber being used was covered with an additional glass slide.

The use of NUNC chambers and Assistant slides was dictated by the need to minimize refractive index mismatch in the laser's path between the confocal objective, the chamber's bottom, and the probed environment, with the ultimate goal of preserving the Gaussian quality of the focal volume, upon which or data fitting relies. As both probed environment and immersion liquid share a refractive index as close as possible, especially thin chambers and slides were chosen.

5.3. Materials employed

5.3.1. Gel constituents

5.3.1.1. PNIPAAm
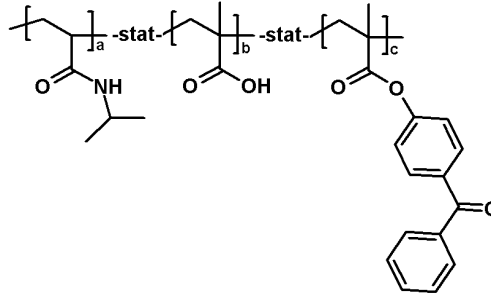
Fig. 4. Structure of employed statistical PNIPAAm (a ~94%, b ~5%, c ~1%). M_W = 265 kg/mol. Polydispersity = 2.2

Poly-N-isopropylacrylamide (PNIPAAm) was synthesized in house at the MPIP by Robert Roskamp via radical terpolymerization. The specific variant employed is a statistical copolymer, the comprising monomers of which are:

- N-Isopropylacrylamide (NIPAAm). 94% of monomers. The bulk of the studied system, exhibits LCST around 32 ºC.

- Methacrylic acid (MMA). 5% of monomers. Provides multiple features:

  • Enhanced solubility of the system in water below the LCST

  • Increased polarity of the system, thus limiting the skin effect of PNIPAAm[25,26,27] and increasing R_S

  • Allowed functionalization of the system prior or after gel crosslinking

- 4-benzoylphenyl methacrylate (MABP). 1% of monomers. Provides crosslinking upon UV irradiation.
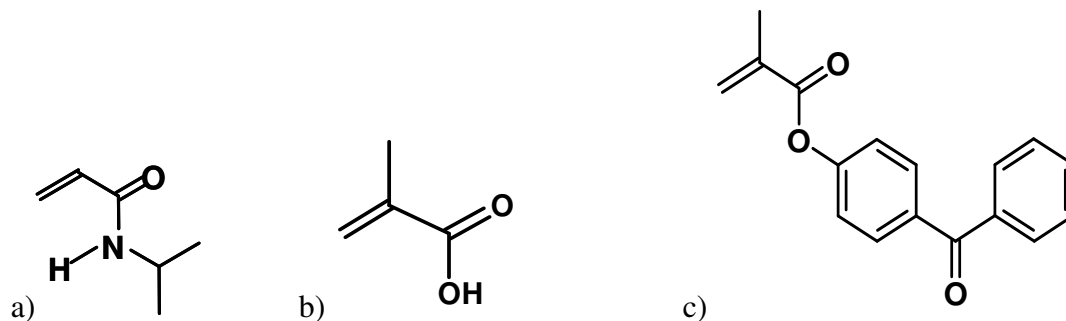
Fig. 5. Monomers comprising the employed PNIPAAm. a) NIPAAm; b) MMA; c) BP crosslinker

Synthesis is described in Robert Roskamp's thesis[28], page 37, and together with PNIPAAm's composition it's also touched in publications[29,29b] by our group.

5.3.1.2. BP-silane

Gel grafting onto glass substrates was achieved by treating glass with a 5 mg/ml solution of 4-(3-triethoxysilyl)propoxybenzophenone (BP-silane) in ethanol. BP-silane was synthesized in house at the MPIP by Robert Roskamp.

Synthesis is described in Robert Roskamp's thesis[28], page 45, as well as in publications[30] by our group.

5.3.2. Solvents
5.3.2.1. Water

All water employed in cleaning procedures, sample preparation and the described experiments is MilliQ water, provided by MilliQ Gradient A10 apparati by Millipore.

5.3.2.2. Ethanol

All ethanol employed in cleaning procedures, sample preparation and the described experiments is Chromasolv ethanol by Sigma-Aldrich (cat. no. 34852).

In many of our procedures, such as gel synthesis or glass slides rinsing and treating, disposable Braun Injekt syringes were employed. Because such syringes were originally developed for medical use, though, they were treated with both an anticoagulant (needle) and a lubricant (needle and syringe body) which could be a source of contamination for our systems once dissolved by ethanol. To avoid this, syringes were rinsed (and needles rinsed and previously cleaned on the outside) with ethanol.

5.3.2.3.   Water-based buffers

5.3.2.3.1.   PBS

PBS buffer employed in the majority of the reported experiments was purchased in dry tablet form from Sigma-Aldrich (cat. no P4417) and reconstituted in MilliQ water for a pH of 7.4 and a concentration of 0.01 M.

For the functionalized hydrogel section of Experiment 3 (section 8.3.2.2, page 156) a sterile PBS variant was employed, provided by Invitrogen (cat. no. 14190094).

5.3.2.3.2.   HEPES

HEPES buffer employed in the described experiments was purchased in dry form from Sigma-Aldrich (cat. no. H7006) and reconstituted in MilliQ water for a pH of 7.4 and a concentration of 0.01 M.

5.3.2.3.3.   Acetate

Sodium acetate buffer employed in sample preparation and the described experiments was purchased from Biacore in liquid form. 4.0 pH (cat.no. BR-1003-49) and 5.0 pH (cat. no. BR-1003-51) variants were employed, both exhibiting a concentration of 0.01 M.

5.3.3. Fluorescent probes
5.3.3.1. Molecular dyes
5.3.3.1.1. Rh6G
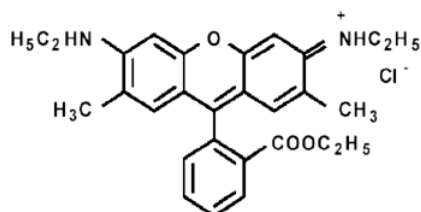
Fig. 6. Structure of Rhodamine 6G $M_W = 479.02$ g/mol

Rhodamine 6G (Rh6G) employed in measurements was purchased from Invitrogen in dry form and dissolved in MilliQ water for a concentration of 20 μM, which was used as stock solution for further dilution. Rh6G was used for calibration in Experiments 1 to 3 and as tracer for the measurements themselves in Experiment 1.

5.3.3.1.2. Cy5

Cy5 was purchased from Invitrogen in dry form and dissolved in MilliQ water to a stock solution concentration of 4 μM. Molecular structure was unavailable due to it being copyrighted by Invitrogen. Cy5 was used for calibration in Experiments 2 and 3.

5.3.3.1.3. Alexa 647

Alexa 647 (disodium salt cadaverine variant, cat. no. A-30679) was purchased in dry form from Invitrogen and dissolved in MilliQ water for a stock solution concentration of 4 μM. Alexa 647 was used as tracer in the measurements of Experiments 2 and 3.
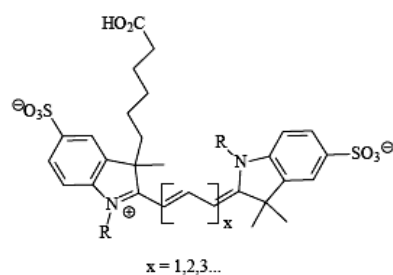
Fig. 7. Structure of Alexa 647. M_W = 1250 g/mol

5.3.3.2. Green Fluorescent Protein

Recombinant Enhanced Green Fluorescent Protein (GFP) was purchased from BioVision (cat. no. 4999-100-BV; Source: E.Coli; stated purity: >97%; 35 mM in PBS; long-term storage temperature: -80 ℃). Upon arrival, GFP was allowed to thaw by progressive warming (-80 to -20 ℃; -20 to 0 ℃; 0 ℃ to room temperature), subdivided in aliquotes and stored at -80 ℃. Upon measurement, an analogous thawing process was applied to a single aliquote, which was then diluted in sterile PBS to the concentration of 30 nM used in measurements. GFP was used as tracer in measurements in Experiment 3.
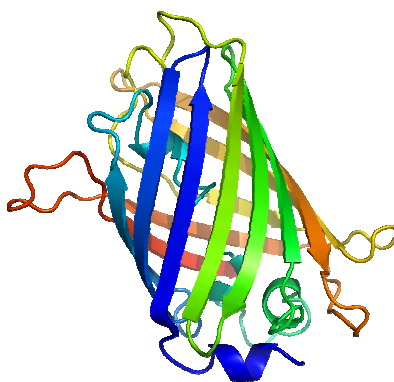
Fig. 8: Structure of GFP. M_W = 29 kg/mol

Fig. 9 depicts a summary of the spectral characteristics of the employed molecular dyes and GFP, together with the other experimental conditions under which they were

employed. As shown, Rh6G is excited by both $\lambda = 488$ nm and $\lambda = 543$ nm. However, of the two only $\lambda = 488$ nm can excite both Rh6G and GFP, and therefore is the one used for channel 2 in Experiment 3 (section 8.3.2.1, page 151). On the contrary, in Experiment 1, which involves Rh6G as the only tracer, $\lambda = 543$ nm is preferred due to the higher excitation provided.

The emission signal splitting determines the recorded excitation for channels 1 and 2 in two-color experiments (Experiments 2 and 3). Concerning this, notice how both Rh6G and (in a much feebler way) GFP emission spectra bleed out into channel 1. This effect is present for Experiment 3 concerning both GFP and Rh6G and Experiment 2 (section 7.2, page 98) concerning Rh6G alone. Because of this, signals from the two channels are not recorded simultaneously, but rather one channel is closed via a shutter while the other is recorded, thus eliminating the bleedout effect.
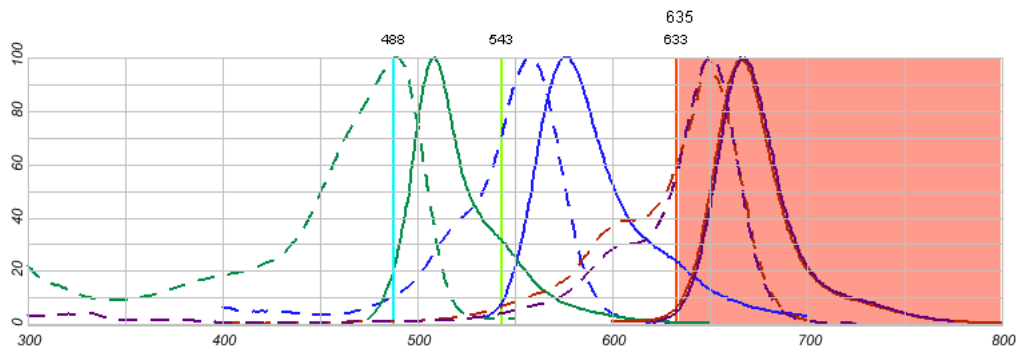
Fig. 9. Normalized excitation (dashed lines) and emission (continuous lines) spectra for GFP (green), Rh6G (blue), Cy5 (red) and Alexa 647 (purple). Vertical lines: employed excitation wavelengths. Dark pink region / white region: dichroic mirror emission signal splitting. Source: www.invitrogen.com

5.3.3.3.   Quantum dots

All quantum dots were purchased from Invitrogen in liquid suspension form (8 μM in borate buffer, 8.0 pH, 0.05 M). They were functionalized with carboxylic groups (c/a 100 per quantum dot), which for our purposes provided the required electrostatic charge to

both prevent aggregation and attractive interaction with the probed systems (both anionic, as is the case of PNIPAAm and the employed inverse opals, the latter being made of silica).
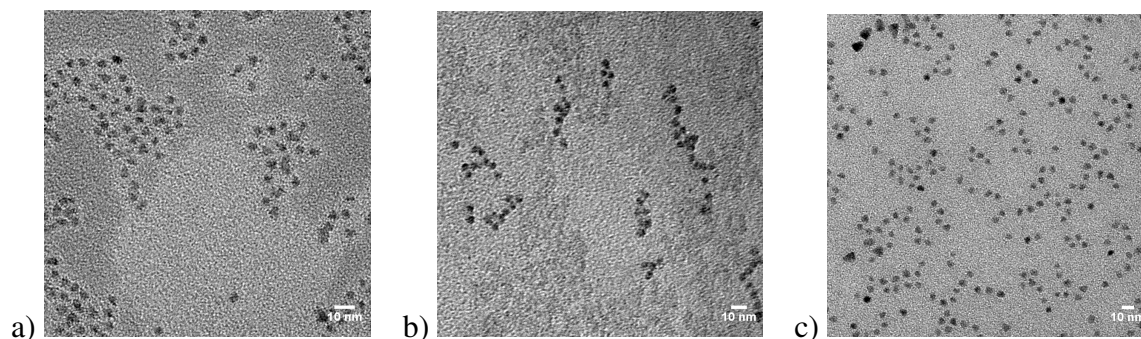
Fig. 10. TEM imaging of the employed quantum dots: a) Qdots 525; b) Qdots 545; c) Qdots 585

As easily observed in Fig. 10, dry size for the Qdots is of difficult determination, skirting the edges of TEM resolution. Additionally, their observed radii in the dry condition, necessary to perform TEM, is around one order of magnitude than what calculated via FCS data. Concerning the latter, one must remember that the Qdots core is surrounded by a water-soluble polymer shell, the thickness of which in the dry state is not provided. In light of this, the TEM pictures at Fig. 10 are reported in order to ensure about their spherical shape (which ensures a single size parameter apported to the diffusion process and parameterization); as for the actual size in the liquid phase, R_H values as calculated through FCS are taken.

Qdots were used as tracers in Experiment 2 (section 7, page 97). Fig. 11 illustrates the Qdots' spectra compared with the other fluorescent diffused at the same time in Experiment 2, Alexa 647, together with the other experimental conditions. As shown, $\lambda = 543$ nm as a wavelength is unfit to excite our Qdots, and $\lambda = 488$ nm is used.
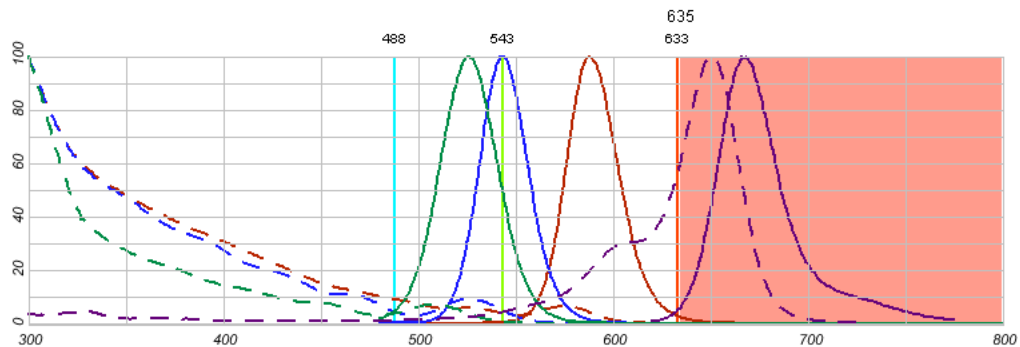
Fig. 11. Normalized excitation (dashed lines) and emission (continuous lines) spectra for the employed Qdots and Alexa647. Green: Qdots 525; blue: Qdots 545; red: Qdots 585; purple: Alexa 647. vertical lines: employed excitation wavelengths. Dark pink region / white region: dichroic mirror emission signal splitting. Source: www.invitrogen.com

Before each experiment three calibration measurements of 5 min duration each were performed (for both channels 1 and 2 for Experiments 2 and 3). For the calibration measurements, cy5 was chosen for channel 1 and Rh6G was chosen for channel 2 on the account of their well-established size (R_H =0.8 nm for Rh6G, 1 nm for Cy5), allowing their *D* to be calculated a priori via the Stokes-Einstein equation and, through this, an easy calibration to be achieved.

5.3.4. Gel functionalization material
5.3.4.1. GFP antibodies

GFP antibodies employed were polyclonal Goat antibodies, with affinity to both enhanced and non-enhanced GFP version. They were produced by Meridian Life Science, Inc. and purchased through Dunn Labortechnik GmbH (cat. no. K59261G) in frozen, PBS-dispersed form (1 mg/ml). Upon delivery, they were subdivided in 20 µl aliquotes according to the method described for GFP and stored at -20 ℃.

5.3.4.2.   TFPS

The employed Sodium para-tetrafluorophenol-sulphonate (TFPS) was synthesized in-house by Robert Roskamp at the MPIP and long-term stored at 4 ℃.

Synthesis is described in Robert Roskamp's thesis[28] at page 46.

5.3.4.3.   EDC

The employed 1-Ethyl-3-(3-dimethylaminopropyl)carbodiimide (EDC) was purchased in dry form from Sigma-Aldrich (cat. no. 03450-1G) and long-term stored at -20 ℃.

5.3.4.4.   Ethanolamine

The employed ethanolamine (ETA) was purchased from Acros Organics (cat. no. 149580010) and stored at room temperature. It featured a nominal 99% purity.

5.3.5.   Inverse opals

Inverse colloidal crystals (inverse opals, or iOpals for short) were prepared in house at the MPIP by Markus Retsch[31,31b], by codeposition of monodisperse colloidal polystyrene (PS) and silica (SiO_2) nanoparticles (LUDOX SM, Sigma Aldrich) on Assistant glass slides. PS particles with a diameter of 180 nm and 130 nm in aqueous suspension were used at a concentration of 1 wt%, the concentration of the silica nanoparticles (LUDOX SM, radius 7 nm) was adjusted to be 0.3 wt%[32]. Vertical lifting deposition (VLD) was conducted at 20 °C, 50 % RH at a lifting speed of 400 nm/s. The films were deposited on plasma treated glass slides (150 µm thickness). After VLD the PS particles were removed by calcination for a few hours in a tube oven at 450 °C in air (heating rate ~10 K/min). The resulting structures are the employed inverse opals (iOpals for short) comprised of fused silica.

The quality of the resulting inverse opal was characterized by SEM on a LEO Gemini 1530 machine (Carl Zeiss AG, Oberkochen, Germany) with acceleration voltage of 1kV in secondary electrons InLens detection mode.
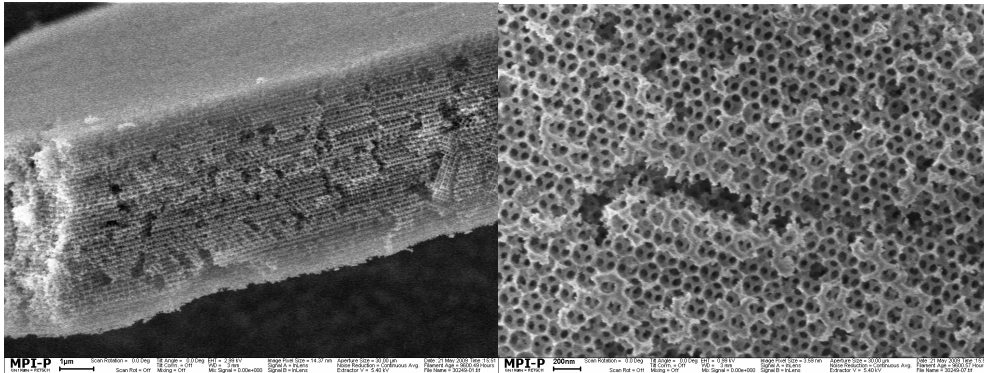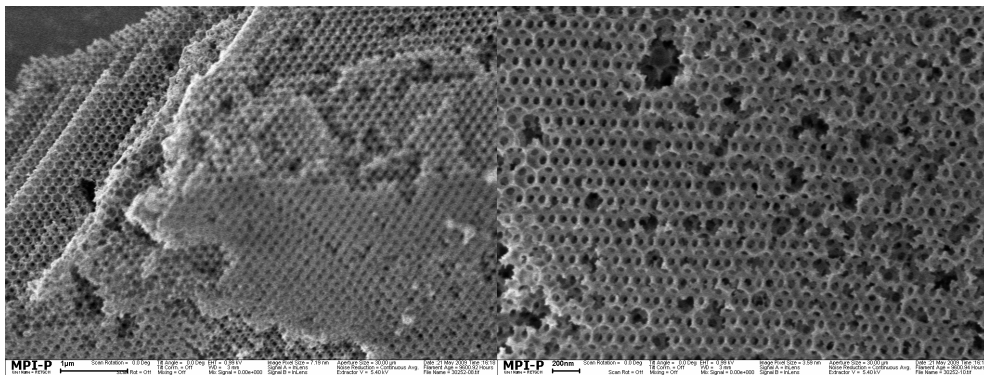

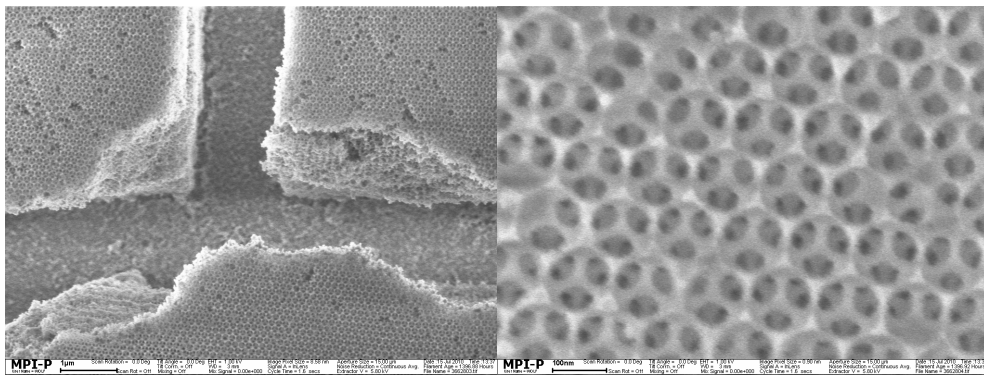Fig. 12. SEM imaging: $180SiO_2$

Fig. 13. SEM imaging: $180SiO_2SolGel$

Fig. 14. SEM imaging: $130SiO_2$

The resulting iOpals, pictured above, are named $180SiO_2$ (180 nm PS particles used), $180SiO_2SolGel$ (as the previous, but with the added inclusion of SolGel previous to calcination) and $130SiO_2$ (180 nm PS particles used). These specimens were employed as systems to be probed in Experiment 2 (section 7, page 97), thus allowing for an observation of diffusion dependent on a 3 independent sizes: the probes', the system's voids, and the system's holes.

The intention behind the use $180SiO_2$ and $130SiO_2$ was to observe diffusion in systems with sensibly different void size but comparable hole size, the latter ideally provided by the low dependence on the PS particle radius of the holes, enhanced by the granular nature of the filler material (the aforementioned silica particles).

Conversely, the intention behind the use of $180SiO_2$ and $180SiO_2SolGel$ was to observe diffusion in systems with same void size but different hole size, the latter achieved by filling the interstitial spaces between the silica particles with SolGel. Specifically, the space delimiting the edge of the iOpals' holes, thus creating a smaller-holes specimen for the $180SiO_2SolGel$ variant.

However, since the calcination process is - obviously - not instantaneous, the actual resulting diameter of the voids is less than that of the employed PS particles, as evidenced by SEM imaging. Worth noting, as described in the following Table 1, is the achieved equal size for voids and different size for holes in $180SiO_2$ and $180SiO_2SolGel$, as well as the missed equal size for the holes in $180SiO_2$ and $130SiO_2$. In the following, R indicates the voids' *radius*, while L indicates the holes' *diameter*. This follows the formalism introduced in order to produce a simulation of diffusion in the system, as it will be detailed in the Experiment's treatment (section 7.3, page 100).

	$180SiO_2$	$180SiO_2SolGel$	$130SiO_2$
Thickness (µm)	7.4	4.6	5
R (nm)	75	75	55
L (nm)	60	50	45

Table 1. Specifics of the employed iOpals

At any rate, concerning the $180SiO_2$ and $130SiO_2$ L disparity, and since our analysis is based on size ratios rather than absolutes, the obtained iOpals were anyway viable for

Experiment 2 and, as it will be shown in the treatment of Experiment 2, the Experiment's results were unimpeded by the difference in hole size between $180Si0_2$ and $130Si0_2$.

Since evaluation of the iOpals' typical lengths implied observation along edges or fracture lines, in detailed SEM measurement defects were to be observed (pictures on the right). However, if one observes the structures at large (pictures on the left) the regular and vastly defect-free structure appears evident.

6. Experiment 1: PNIPAAm-Rhodamine interactions in a water solution

6.1. Motivation

The PNIPAAm-Rhodamine interaction Experiment was the first spawned from the main hydrogel study project (section 8, page 117). Previous successful PNIPAAM gel evaluations experiments[12] via FCS were conducted in ethanol, since in ethanol the gel's charges fail to hydrolyze, therefore leading to a relatively simple system, virtually devoid of electrostatic interactions with charged fluorescent probes. Rh6G itself, a notoriously heavily cationic dye, was observed diffusing with Fickian time dependence in ethanol-swollen PNIPAAm. However, upon swelling of the same gels in water, Rh6G diffusion was much more complex and problematic to interpret. However, since the aim of the project was geared towards the development and improvement of biosensor systems, it was necessary to study the gels in water.

On one side, this heavily restricted the fluorescent probes' choice. Since the studied systems are already complex and - obviously - partially unknown, it was deemed necessary to probe them starting from the simplest interaction possible: collisional/frictional slowdown, raising the experiments' complexity in a second moment. This, of course, barred cationic and generally attractively interacting probes like Rh6G from the study, and in the end led us to the choice of the weakly anionic Alexa 647 as baseline probe of choice for water-based swelling experiments.

On the other side, it was deemed optimal to study PNIPAAm interaction with cationic entities, in order to be able to recognize its impact on tracer diffusion and possibly quantify it in our systems.

Additionally, the question of different body interaction, in solution as well as in different systems[33], has found theoretical[34] and practical[35] interest and was approached from many different experimental[36], and numerical[37] fronts, and has as well been addressed via FCS[14,15,16,17,18,19]. However, to the best of my knowledge, a simple, reliable model for the quantification of small-range, short-time interactions is still to be

implemented. In this context, the Experiment treated in this section was an attempt at developing a relatively simple, practical tool to evaluate said interaction from FCS data.

To this end, the little understood, charge-driven Rh6G-PNIPAAm interaction was studied in a system simpler than crosslinked gels and, indeed, the simplest available. The tracer, Rh6G and uncrosslinked PNIPAAm chains were diffused in water, and D of Rh6G analyzed.

6.2. Experimental

The FCS setup employed was the one described in section 5.1 (page 33) for Experiment 1. The system studied consisted in Rh6G diluted at the fixed concentration of 20 nM in a water-PNIPAAm solution spanning a gamma of 6 concentrations, from comparable to Rh6G to little below the overlapping concentration[12], as the interest of the experiment was to observe the effect of PNIPAAm presence in Rh6G diffusion without the imposition of an actual, albeit non-crosslinked, network structure. The solutions were placed in NUNC chambers and studied at room temperature (nominally 21 ± 1 ºC).

$I(t)$ was typically recorded for 5 min, for diffusion in pure solvent with strong fluorescence, to 10 minutes in the case of diffusion in dense gels where few particles could penetrate. These total accumulation times were subdivided in 30-seconds intervals in order to enable removal of occasionally erroneous signals due to abnormally large aggregates. Since the presence of interactions, and therefore possible aggregation, was the entire scope to this Experiment, anomalous contributions were excluded only when making the resulting overall $G(t)$ unfittable, an eventuality which only verified in a number of cases in the units.

Prior to the measurements, calibration was performed in NUNC chambers on a 20 nM solution of Rh6G in MilliQ water. Three values were taken and averaged for each calibration session.

All $G(t)$ curves were fitted excluding the data points up to ~ 10 μs, beyond the triplet effect time range, thus allowing for an exclusion of the triplet contribution parameters from the fit.

Concerning Rh6G concentration, although the solutions were prepared at 20 nM Rh6G concentration (c_R), this was partially altered during the experiment due to two effect.

The first was the high charge of Rh6G, which although pivotal in the experiment, caused a fraction of it to routinely stick to the bottom of the NUNC chambers, therefore lowering the effective c_R in the solutions.

The second effect consisted in the sought-after interactions with PNIPAAm. Although lowered by the chamber interaction effect, the observed c_R was found to increase with increasing PNIPAAm concentration, c_P. This is explained as Rh6G-PNIPAAm interactions can render the deposition of the Rh6G molecules on the chamber walls less favored. Indeed this possibility can be taken as a first quantitative effect of the interaction phenomenon.

The altered concentration is observed in the values for N as obtained from fitting $G(t)$. Similarly, the focal volume V_{foc} could be calculated[21] from fitted data via

$$V_{foc} = \pi^{\frac{3}{2}} x_0{}^2 z_0 = \pi^{\frac{3}{2}} S x_0{}^3 \tag{6.1}$$

The actual c_R can now be evaluated, where the error can be estimated under the assumption of independent variables through

$$\frac{\Delta c_R}{c_R} = \frac{\Delta N}{N} + \frac{\Delta S}{S} + 3\frac{\Delta x_0}{x_0} \tag{6.2}$$

The actual c_R values ad different c_P are reported in Table 2 below. Here c_P is reported both in g/ml and mol/L (M), and the actual c_R values in M. As one can see, c_R is routinely different from the initial value of 20 nM as aimed at during solutions preparation. $\dfrac{c_P}{c_R}$ (actual) is therefore the number ratio between PNIPAAm and Rh6G

molecule in solution. $\dfrac{c_P}{c_R}$ (initial), i.e. the theoretical number ratio between PNIPAAm

and Rh6G molecule in solution if c_R were 20 nM, is also added for comparison.

Sample	c_P (g/ml)	c_P (M)	c_R (M)	c_P / c_R (initial)	c_P / c_R (actual)
1	2.87E-06	1.15E-08	4.4E-09 ± 4.6E-10	0.574	2.6 ± 0.3
2	1.76E-05	7.04E-08	9.2E-09 ± 3.8E-10	3.52	7.7 ± 0.3
3	5.55E-05	2.22E-07	4.9E-08 ± 2.5E-08	11.1	4.6 ± 2.3
4	1.94E-04	7.76E-07	2.9E-08 ± 9.9E-10	38.8	26.8 ± 0.9
5	5.60E-04	2.24E-06	7.2E-08 ± 3.2E-09	112	31.0 ± 1.4
6	2.28E-03	9.12E-06	7.2E-08 ± 5.5E-09	456	125.8 ± 9.5

Table 2. Concentrations of PNIPAAm and Rh6G in the Samples

Fortunately, the Experiment revolved around c_P, and the condition of c_P being routinely larger than c_R, which is still met, and even enhanced at small PNIPAAm concentrations.

In addition to what already described, a third and fourth effects are worth noting.

The third effect consists in the c_R above Sample 3 being actually *larger* than 20 nM. The fourth effect consists in Sample 3 itself marking an anomaly in the experimental c_R due to the abnormally high average (for the c_P range it's in) and error.

Concerning the fourth effect, the obtained values stem from both the statistic procedure employed - average over 3 different points in the sample - and the especially high concentration fluctuations observed in said points for Sample 3.

Both the third and fourth effect can be explained, again, in light of the competition between Rh6G-chamber and Rh6G-PNIPAAm interaction: due to the first, Rh6G is attracted to the chamber's walls and bottom, thus creating a region near the chamber's bottom where $c_R > 20$ nM, with a statistical gradient leading to a zone, far above the bottom, where $c_R < 20$ nM; due to the second, adifferent c_P, the effect just described is weakened to a different degree. Therefore, at low c_P, one can expect a high c_R near the bottom, with a sharp gradient leading to a constant concentration region with $c_R < 20$ nM in a short space interval. As c_P is increased, the competition mechanism described as the

second effect causes the gradient to be less sharp, and the region with $c_R > 20$ nM to extend farther in the vertical direction.

Since the sample was probed at a constant height of 200 μm above the chamber's bottom, both the $c_R > 20$ nM and $c_R < 20$ nM regions were probed as c_P was increased. Sample 3 marks an inversion point between these two regimes, meaning that for c_P of Sample 3, tracer diffusion is probed in the middle of the threshold region, which accounts both for the inversion in $c_R > 20$ nM versus $c_R < 20$ nM, and for the larger fluctuations in c_R in said Sample.

a)   b)   c)
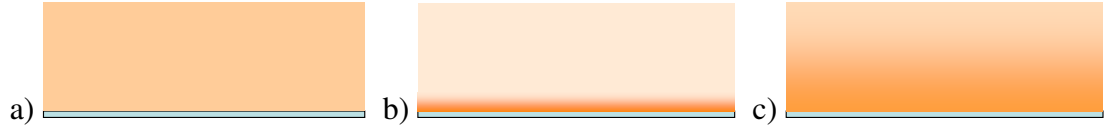
Fig. 15. Scheme of dye concentration in a chamber: a) uniform dye concentration in the absence of dye-chamber interaction; b) dye attracted to the chamber leading to a sharp concentration gradient in the chamber bottom region; c) dye attracted to the chamber's walls in the presence of additional attracting species (PNIPAAm, in this case) in solution leading to a broad concentration gradient

In analogy to Table 2, the average number of PNIPAAm chains can be calculated in relation to such quantities as V_{foc} or fixed volumes, such as 1 nm^3.

Sample	V_{foc} (ml)	c_P (N/vol)	c_P (N/nm^3)	d_P (nm)	d_P - $2R_{HP}$ (nm)
1	1.95E-13 ± 2.E-15	1.35 ± 0.01	6.91E-09	524.94	490.14
2	1.98E-13 ± 2.E-15	8.39 ± 0.09	4.24E-08	286.79	251.99
3	2.10E-13 ± 2.E-15	28.0 ± 0.3	1.34E-07	195.57	160.77
4	2.14E-13 ± 2.E-15	100.0 ± 0.9	4.67E-07	128.86	94.06
5	1.66E-13 ± 2.E-15	224 ± 2	1.35E-06	90.50	55.70
6	1.67E-13 ± 2.E-15	915 ± 12	5.49E-06	56.68	21.88

Table 3. Focal volume estimation and numerical estimation of PNIPAAm-PNIPAAm distances

where the PNIPAAm-PNIPAAm average distance (d_P for short) was estimated from c_P, (hereafter expressed in N/nm^3) as

$$d_P = c_P^{-\frac{1}{3}} \qquad (6.3)$$

The last column deserves some attention. It reports the calculated d_P, minus $2 \cdot R_{HP}$, where R_{HP} is the hydrodynamic radius, R_H, for PNIPAAm in water, which as reported in the data analysis section (6.3, page 52) has been measured as 17.4 ± 0.3 nm, lower than the measured R_{HP} for the same specimen in ethanol[12] (19 ± 1 nm). This is consistent with PNIPAAm possessing a better solvency in ethanol than in water, thus leading in ethanol to more swollen chains, larger R_{HP}, and subsequent earlier overlapping.

The last column therefore represents the average distance between the surfaces of two adjacent spheres representing PNIPAAm chains. As seen in Table 3, the distance between the chains is larger than R_{HP} even at the highest c_P (Sample 6). Therefore, we can consider the system to be still below the overlap concentration, c_P^* (albeit this method of estimation is, admittedly, qualitative more than quantitative).
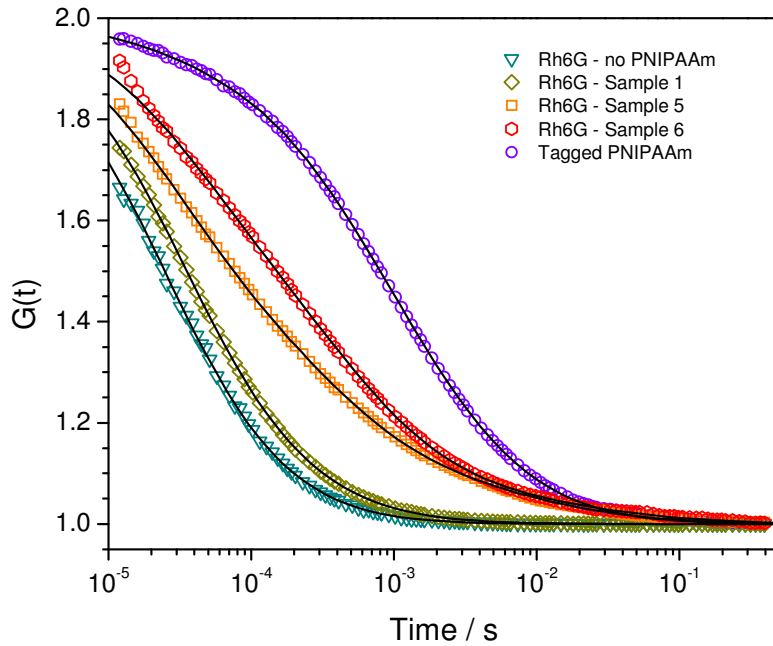
6.3. Diffusion and possible Models

Fig. 16. $G(t)$ curves in water. Solid lines: fit curves according to Model 1

Described in Fig. 16 are selected $G(t)$ curves for the Samples. Samples 1, 5 and 6 are reported, together with Rh6G in absence of PNIPAAm and Rh6G-labelled PNIPAAm for comparison. The behaviour of Rh6G in the different Samples is situated in between Rh6G alone and PNIPAAm. One can also notice how, while the measurement of Sample 1 yields a $G(t)$ fairly similar, if slightly slowed down, to Rh6G alone and PNIPAAm, the $G(t)$ profiles of high-c_P Samples measurement feature a different kind of behaviour, clearly differing from a simple Fickian behaviour. As for the exact nature of said behaviour, it is the pivotal element of this analysis, and two possible models were considered:

Model 1: Fickian diffusion.

More specifically, multi-component Fickian diffusion. This Model was adopted through attempts to fit the obtained $G(t)$, which could not be fitted with one Fickian component. Instead, three components are necessary to fit one $G(t)$ properly. The criterion for a good fitting, in this case like in the rest of the thesis, is whether the yielded fitting residuals (fitted curve values minus experimental curve values) display the following characteristics, in decreasing order of importance:

1. Distribution around 0;
2. Horizontal, flat, featureless pattern plus random noise;
3. Small values.

For all Samples, the two major components were roughly one order of magnitude apart in D, the first one displaying a D consistent with free Rh6G and the second, slower one, D between that of Rh6g and PNIPAAm. The third component was much feebler in signal fraction, and one to two orders of magnitude slower than the second component. As mentioned, all components are Fickian.

Reported values, in this Experiment as well as in the rest of the thesis, are obtained via weighted average, where the parameter used in the weighting is the relative error. This partially deviates from the more common weighting via absolute error, but was deemed a

more correct evaluation method due to the fluctuating dispersion of data within the same Experiment. For example, data with comparable absolute error have been shown to differ for the same sample by a factor 2 in the present Experiment at high c_P, or in the more confined iOpals or in gels of more complex structure respectively in Experiment 2 (Section 7, page 97) and Experiment 3 (Section 8, page 117). Thus, it has been adopted for the averages:

$$\overline{A} = \frac{\sum_i w_i A_i}{\sum_i w_i} \tag{6.4}$$

where A_i are the individual measured or calculated values, $\overline{A}$ their average, and $w_i = \left(\frac{\Delta A_i}{A_i}\right)^{-2}$ the weights as obtained from the individual values' relative errors. As for the error over $\overline{A}$, the same weighting method was applied to the calculation of the standard deviation, which was assumed as error:

$$\Delta\overline{A} = \sigma\overline{A} = \sqrt{\frac{\sum_i w_i \left(A_i - \overline{A}\right)^2}{\sum_i w_i}} \tag{6.5}$$

Weighted average was performed for this Experiment over a minimum of 3 different individual values, measured for each Sample in different XY positions and at 200 μm above the chambers' bottom.

Fig. 17 and Fig. 18 detail Model 1 analysis on the Samples.

As seen in Fig. 17, Component 1 (compatible with free Rh6G diffusion values) keeps a virtually constant D throughout the whole PNIPAAm concentration range, with what appears to be a possible minor slowdown effect, easily attributed to the increasing solution viscosity. We identify this datum as D_R. As for Component 2, its D keeps consistent over the first three (possibly the first four) Samples (c_P ranging from 11.5 nM to 222 nM in the first case, or to 776 nM in the second), and then drops to non-

54

compatible values for Samples 5 and 6, which are close to PNIPAAm's D (D_P). We'll refer to this second diffusion process as *hybrid diffusion* and identify its D as D_h.
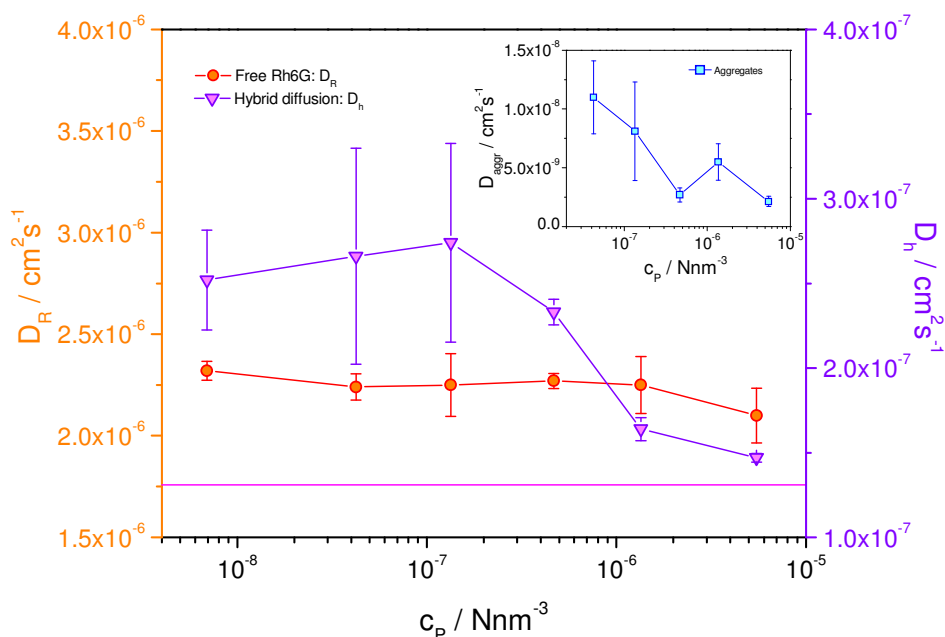
Fig. 17. Multi-component Fickian diffusion observed in the Samples, as fitted according to Model 1: diffusion coefficients. Free Rh6G D values (D_R) are to be read on left Y axis, hybrid D values (D_h) on right Y axis. The pink horizontal line is D for tagged PNIPAAm, measured with the same setup, and its value is also to be read on the right Y axis. Inset: The diffusion of the third, slowest process

Similarly, as seen in Fig. 18, a moderate increase in F_h at the expenses of F_R can be observed up to Sample 4, above which the F_h dependency on c_P appears more steep.

A third component had also to be introduced in the fitting, displaying D values one order of magnitude lower than D for PNIPAAm and decreasing with increasing c_P together with signal fraction increasing with c_P but keeping below 10%. Due to the high size, c_P dependency and (obviously) fluorescence, this third component has been identified as given by multi-chain aggregates of PNIPAAm and Rh6G – essentially, the

result of Rh6G effectively gluing together multiple PNIPAAm chains. We therefore refer to its D and fraction as D_{aggr} and F_{aggr}.

Whether these aggregates were permanent or transient was not clear, but their existence was corroborated by the observation of white specks in the solution, visible with the naked eye.
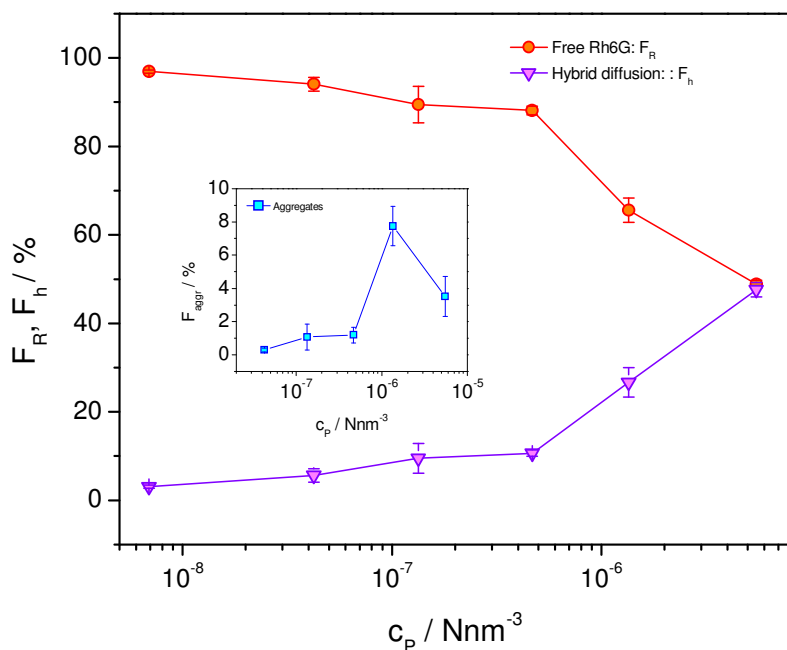
Fig. 18. Multi-component Fickian diffusion observed in the Samples, as fitted according to Model 1: components' fractions (fast and intermediate processes in the main plot and third process in the inset)

Model 2: non-Fickian diffusion.

According to this second Model, adopted as a possible alternative to Model 1, during the early theorization stages of the system data, $G(t)$ for the Samples can be fitted with two components: a dominant non-Fickian one ($\langle \Delta r^2 (t) \rangle \propto t^x$, with $x < 1$) and a second, Fickian, feebler one analogous to the aggregates component in Model 1.

Whether Model 1 or 2 is to be preferred was a central question in the study of this Experiment, and pivotal in identifying the mechanism of the observed interaction.

In order to discriminate between the Models, let's simplify them for a moment to a situation where PNIPAAm chains are envisaged as hard spheres, randomly distributed in fixed positions in the solution. That is, we neglect PNIPAAm motion, on the basis of D_P being one order of magnitude smaller than D_R. In this picture, two outcomes appear possible for the altered Rh6G diffusion. These two outcomes correspond to the two Models:

Model 1 (Fickian): Rh6G-PNIPAAm interaction verifies at short length range. In this Model, Rh6G possesses a certain likelihood to stick to PNIPAAm. The analysis here is purely phenomenological: the distance dependence and specific mechanics underlying the electrostatic interaction are not investigated, and we simply consider Rh6G-PNIPAAm interaction as a rigid-spheres model in Brownian motion, where the different bodies can, upon collision, stick to one another for an average attachment time τ_a, after which detachment occurs. In this model, Rh6G diffuses Brownianly with D_R until it comes into contact and attaches to a (fixed in this approximation) PNIPAAm chain. After τ_a, detachment happens and Brownian diffusion resumes until Rh6G comes into contact and is captured again by a new PNIPAAm fixed point, and so on. If the system is observed on a large scale relatively to the PNIPAAm-PNIPAAm distance, given the random distribution of PNIPAAm, attachment in this model merely acts as a reducer of the overall Rh6G mobility, not altering the Brownian character of diffusion. Since FCS derives diffusion coefficients from overall diffusion times, the waiting times τ_a Rh6G spends on the fixed PNIPAAm chains during observation simply reduce the average observed D_R to a smaller value. Reintroducing PNIPAAm motion in the model merely introduces additional Brownian motion during τ_a, during which Rh6G actually diffuses with D_P, thus mitigating the D_R reduction from the "immobile PNIPAAm" approximation.

If observed on a scale small enough relatively to the PNIPAAm-PNIPAAm distance, motion in this model will appear again Brownian, but the average observed D will exhibit larger deviations from a single average value the smaller the scale considered, both in terms of space an time intervals. When considering the system on a scale comparable (or

smaller) than the typical motion scale of Rh6G during its attached / free diffusion, one would actually observe a splitting of the observed D, since a concrete chance would come into being of: 1) observing a part of the Rh6G population diffusing freely in between detachment and subsequent attachment to a PNIPAAm chain for the whole observation time (thus giving a diffusional process possessing D_R); 2) observing a part of the Rh6G population diffusing attached for the whole observation time, if the average distance for attached diffusion became comparable with the system observation size (D_P observed). The chance of observing Rh6G diffusing partly attached, partly free would of course remains (it would always be possible to observe Rh6G detaching or attaching during observation). This is what we've referred to as hybrid diffusion, and its D is of course again D_h.

As it is characteristic of FCS to observe a system, like in the present case, on especially limited time and length scales, Model 1 would explain the multi-component Fickian fitting of the data as an effect of said limitation: the observation of D_h, plus D_R for those Rh6G molecules happening to be observed in between PNIPAAm encounters.

As it will be shown further in the treatment, the limitations described can nonetheless be turned into a useful tool to analyze the interaction itself.

Model 2: Rh6G-PNIPAAm interaction verifies at long length range. In this model, the attaching/detaching mechanism for Rh6G is again at work, just as seen in Model 1. Also, in addition to it, Rh6G molecules are deviated from Brownian motion long before they get to stick to PNIPAAm, as their trajectory is influenced by PNIPAAm chains near and far. Although in this model immobile PNIPAAm chains would impose vinculi to a large-scale Brownian motion of Rh6G (trajectories of Rh6G molecules would be systematically be deviated towards fixed points), reintroducing Brownian motion in the chains would again allow for a large-scale Brownian behavior of Rh6G, again displaying an average D.

If observed on a small scale, however, the deviation from the single diffusion of this Model predicts both Brownian and non-Brownian motion for Rh6G: Rh6G observed while attached to PNIPAAm would move with Brownian D_P as in Model 1, but free Rh6G would now exhibit trajectories influenced by surrounding PNIPAAm, thus

deviating from random Brownian behavior. Indeed, while the chaotic Brownian behaviour leads in a solution to Fickian trajectories, which can be approximated on a scale long enough with linear trajectories, the presence of far-interacting PNIPAAm would generate curved (i.e. non-Fickian) trajectories.

Concerning hybrid diffusion again, an additional feature of Model 2, as opposed to Model 1, is that Model 2 allows for the relaxation of the condition of Rh6G actually attaching to PNIPAAm: simple long-range attraction without a residence time such as τ_a would still generate Fickian diffusion on the large length scale and non-Fickian on the small length scale, while the additional small-scale PNIPAAm-attached diffusions (both the Fickian diffusion and the hybrid non-Fickian diffusion) would come to vanish.

Model 2 would explain the single-component (excluding the aggregates component) non-Fickian fitting of the data as a system where attached (if present) and non-attached Rh6G diffusion happen on a smaller length scale than the observation length scale, thusly not triggering signal splitting. Under this hypothesis, curved Rh6G trajectories induced by long-range PNIPAAm-Rh6G interactions suffice to explain the data fitted according to the non-Fickian method.

We'll refer to the D of the non-Fickian diffusional component in Model 2 as D_{nF}.

In order to develop a coherent theory of the interaction, a Model had to be chosen over the other.

From a point of view of pure data analysis, common fitting wisdom suggests the solution with less parameters to be preferred. In the present Experiment, 6 independent parameters were necessary to fit $G(t)$ for the samples according to Model 1 (N, τ_R, τ_h, τ_{aggr}, F_R and F_h; $F_{aggr} = 1 - F_R - F_h$, and therefore non-independent. Indexes for the various τ refer to the matching diffusional processes). Model 2 requires 5 parameters (N, τ_{nF}, τ_{aggr}, x_{nF} and F_{nF}, since for the Fickianly-moving aggregates we have $x_{aggr} = 1$, and of course $F_{aggr} = 1 - F_{nF}$). This apparently points Model 2 as more favorable.

However, numerical considerations such as the number of parameters should be secondary to physical significance. In this sense, the presence of Rh6G-PNIPAAm aggregates in the Samples posits a possible contradiction in Model 2: the presence of

aggregates means that Rh6G and PNIPAAm indeed attach to each other, a phenomenon which is not seen in the one-component non-Fickian diffusion in Model 2.

Conversely, it could be argued that aggregates could actually be the only outcome of Rh6G-PNIPAAm attachment – that is, that no Rh6G-PNIPAAm *pairs* exist. This would solve the apparent Model 2 contradiction. Then again, if this were the case, then the same mechanism would likely result in an impediment to the very presence of non-attached (i.e. under the very same hypothesis, non-aggregate) Rh6G at high c_P, or at least to a progressively decreasing presence of such. On the contrary, the Samples were stored and observed stable over week-long spans of time.

A quantitative point towards the choice of a Model over the other comes in the form of residual analysis. Reported in Fig. 19 below are residuals for Samples 1, 5 and 6 of the series, fitted according to Model 1 and 2. As one can see, $G(t)$ curves show better residuals if fitted with Model 1. This feature can be taken as a first physical datum corroborating a Model. Also, combined with the possible contradiction in Model 2 featured in the previous paragraph, motivated the following inquiry into the detailing of Model 1, which is therefore the Model I'll be testing for the rest of this Experiment's treatment.
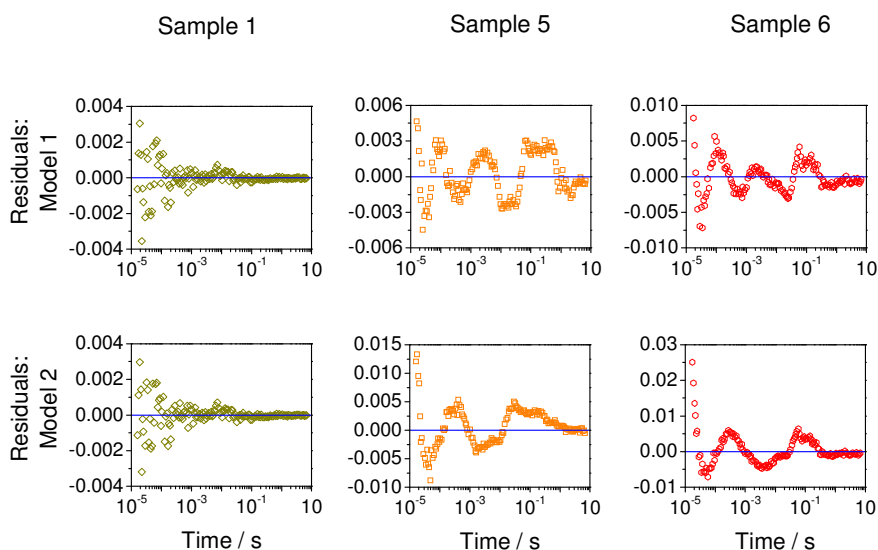

Fig. 19. Residuals for Samples at low and high c_P, fitted according to the two Models

6.4.   Data analysis and theory development
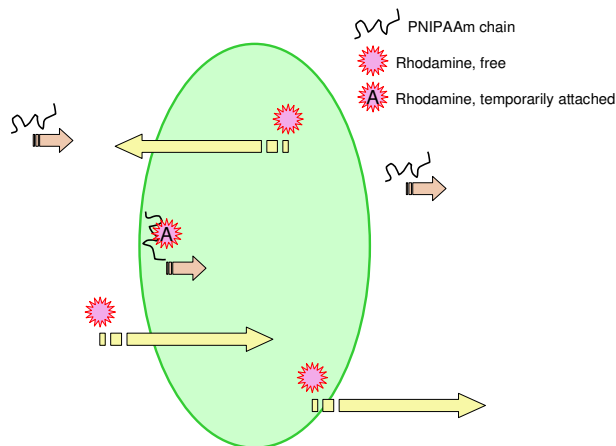
Fig. 20. A scheme of Rh6G diffusion in the focal volume

Fig. 20 illustrates the general concept of Model 1: large PNIPAAm chains move at low D_P / long τ_P; small Rh6G molecules move at high D_R / short τ_R. Whenever Rh6G encounters PNIPAAm, a chance occurs that the two attach temporarily due to electrostatic interaction. As described before, this generates a double signal in a limited volume such as ours: free signal plus hybrid signal. It bears stressing again that, in the Model used, *every* Rh6G molecule attaches and detaches from PNIPAAm chains during its diffusion and, thusly, a large enough focal volume would guarantee only a single, hybrid signal to be observed: the free Rh6G signal is observed in the actual experiments purely due to the restricted observation space.

About the chance of attaching upon contact, one can apply a first refinement to the Method's developing formalism by introducing the likelihood of a Rh6G molecule to attach to a PNIPAAm chain upon contact, l_a. l_a is a function of the two interacting bodies' charge - or charge distribution - as well as the solvent's properties. It is, in the general case, $1 > l_a > 0$. We can now introduce the effective average PNIPAAm-PNIPAAm center of mass distance, d'_P, as

61

$$d'_P = \frac{d_P}{l_a} \qquad (6.6)$$

d'_P is the average PNIPAAm-PNIPAAm center of mass distance sensed by Rh6G molecules for the purpose of attachment; In other words, the length scale over which attachment events occur in the system. Small l_a leads to large d'_P and vice versa.

d'_P can be compared with the length scale over which the system is observed, i.e. the effective diameter of the focal volume, $2x_0$. Two different Regimes can now be delineated:

$d'_P > 2x_0$ Regime: in this Regime, d'_P is too large to be observed within the boundaries of the observation method. As a result, any Rh6G observed interacting will either attach to/detach from a single PNIPAAm chain, and all the remaining Rh6G molecules will be observed diffusing free. One can formally describe this by introducing n_a, the *average number of Rh6G-PNIPAAm encounters which will be observed being experienced by those Rh6G molecules contributing to hybrid diffusion*. As I described, in the $d'_P > 2x_0$ Regime, it is identically $n_a = 1$.

$d'_P \le 2x_0$ Regime: in this Regime, d'_P is comparable with the length scale of the observation volume. As a result, the chance arises for Rh6G molecules to be observed interacting with more than one PNIPAAm chain each. At the same time, the chance still exists for Rh6G molecules to not interact with any PNIPAAm chain during observation. Hence, the free Rh6G signal will still be present, while for the molecules generating the hybrid signal, we'll observe $n_a > 1$.

Based on these considerations, we can now attempt a formal rationalization of the observed diffusion coefficients.

We can write the hybrid diffusion coefficient D_h as a sum of two contributions:

$$D_h = F_f D_R + F_a D_P \qquad (6.7)$$

where the dimensionless F_f and F_a are the time fractions Rh6G spends free and attached respectively while in the focal volume. These are given by

$$F_f = \frac{\tau_f'}{\tau_f' + n_a \tau_a'} \tag{6.8}$$

$$F_a = \frac{n_a \tau_a'}{\tau_f' + n_a \tau_a'} \tag{6.9}$$

in relation to the average times, τ_f' and τ_a', that Rh6G spends respectively free and attached to one PNIPAAm chain while in the focal volume. As a result,

$$D_h = \frac{\tau_f' D_R + n_a \tau_a' D_P}{\tau_f' + n_a \tau_a'} \tag{6.10}$$

As a reminder, here τ_a' and τ_f' are intended as the average time interacting Rh6G spends respectively attached on PNIPAAm and free *during observation*. These are generally different from the average times it spends in the same states regardless of the observation length and time, which I'll refer to, more simply, as τ_a and τ_f.

In fact, one must at this point further differentiate the theory, similarly to what done with the $d_P' > 2x_0$ and $d_P' \leq 2x_0$ Regimes. While the former established a threshold, as it is, for the observed length scales, we must now approach the relation between the typical time scales of the observed processes, that is the way τ_a and τ_f relate to the typical length and time scales of the focal volume and environment.

<u>Case 1:</u> $\tau_R > \tau_a$: Rh6G stays attached to PNIPAAm for a shorter time it would take free Rh6G to diffuse through the volume. In this situation, it is easily seen how $\tau_a \cong \tau_a'$. We can now set ourselves to calculate τ_f. τ_f can be calculated from the known expression

$$D = \frac{x_0{}^2}{4\tau} \qquad (6.11)$$

By substituting here D with the actual D_R, τ with τ_f, and x_0 with the half-distance Rh6G diffuses free, we can calculate τ_f as a function of said half-distance, x_f, and known values. I'm calling x_f the half-distance in this treatment for reasons of consistency with the half-width of the focal volume, x_0.

Here I'd like to remark on the difference between τ_R and τ_f: τ_R is the time free Rh6G spends traveling through $2x_0$ (and thusly dependent on the observation conditions); τ_f is the time free Rh6G spends traveling between two PNIPAAm attachment/detachments. (and thus independent of the observation conditions).

As we're assuming diffusion to be Fickian, a Rh6G molecule's diffusion can be schematized in a first approximation to be following a linear trajectory.

This is a relatively heavy simplification, but justified by the system's conditions: 1) Brownian diffusion; 2) absence of Rh6G-Rh6G collisions due to low concentration; 3) absence of long-range interactions with PNIPAAm. Under these conditions, we can expect trajectory fluctuations to be due to thermal noise alone, and therefore Rh6G trajectory to be random on a scale smaller than the one considered (until, of course, interaction with PNIPAAm verifies).

As a result of the linear trajectory schematization, x_f will be directly proportional to $\frac{d'_P}{2}$ (since x_f is a half-distance), the difference between the two being an additional, geometrical parameter, which must now be introduced.

Consider a Rh6G molecule diffusing for a distance d'_P after detaching from a PNIPAAm chain. Such distance, as we mentioned, is the average effective (i.e. normalized to l_a) PNIPAAm-PNIPAAm distance, and therefore in our Model the Rh6G molecule would stick to a new PNIPAAm chain disting d'_P from the previous one. However, such event occurs only when a PNIPAAm chain actually is on Rh6G's

trajectory. Since both PNIPAAm and Rh6G are small compared to d'_P, this is much less than certain.

In other words, in our Model Rh6G cannot attach to any PNIPAAm chain before diffusing a distance d'_P. Once diffusing for d'_P, it will attach, on the condition that it actually encounters (collides with) a PNIPAAm chain.

Therefore, the new parameter we need is a geometrical likelihood of contact, l_c. l_c will depend on the sizes of both Rh6G and PNIPAAm. Indeed, supposing a fixed concentration, the larger the objects in solutions, the easier it will be for them to collide, while small entities like PNIPAAm chains and a molecular tracer like Rh6G will need to find themselves on very similar diffusional trajectories to encounter each other.

It will be, analogously to l_a, $1 > l_c > 0$, and like l_a will act as an additional normalization modifier to d'_P. In other words, d_P accounts for PNIPAAm concentration, l_a for Rh6G-PNIPAAm electrostatic interaction, and l_c for the sizes of the involved objects. We can write x_f as

$$x_f = \frac{d_P}{2 l_a l_c} \tag{6.12}$$

While l_c can be deduced through geometrical considerations, as shown further in the Experiment's treatment, l_a is an intrinsic property of the involved bodies, and of the solvent, and therefore x_f cannot be calculated without first calculating l_a (actually, as I'll be showing, l_c itself is dependent on l_a).

Luckily enough, as again will be shown further in this treatment, l_a itself can be calculated in a first place through observable data, and specifically from the signal fraction of the hybrid diffusion, F_h.

As a first *quantitative* step in our analysis, though, let us get back to the diffusion coefficients of the $\tau_R > \tau_a$ Case. Let us place ourselves in the $d'_P > 2x_0$ Regime: as I mentioned, in such a Regime it is $n_a = 1$.

Given the length and time scale of the system, it is for D_h:

$$D_h = \frac{\tau'_f D_R + \tau_a D_P}{\tau'_f + \tau_a} \tag{6.13}$$

In this Case, $\tau'_f + \tau_a$ is a measured quantity, that which we can called hybrid diffusion time, $\tau_h = \tau'_f + \tau_a$. D_R, D_P and D_h are also quantities directly obtained from the measurements: D_R and D_h from τ_R and τ_h as fitted from the same $G(t)$ curve, and D_P obtained from a separate measurement. By writing $\tau'_f = \tau_h - \tau_a$ one has

$$D_h = \frac{(\tau_h - \tau_a)D_R + \tau_a D_P}{\tau_h - \tau_a + \tau_a} = \frac{(\tau_h - \tau_a)D_R + \tau_a D_P}{\tau_h} \tag{6.14}$$

which can easily be rewritten as

$$\tau_a = \left(\frac{D_R - D_h}{D_R - D_P}\right)\tau_h \tag{6.15}$$

With this, one can directly calculate the residence time τ_a from easily fitted values. As a confirmation, one can see that in the $D_h \to D_R$ limit, $\tau_a \to 0$ (0 residence time equals vanishing hybrid signal). At the other end of the spectrum, in the $D_h \to D_P$ limit, $\tau_a \to \tau_h$: hybrid diffusion entirely comprised of attached diffusion, which the additional meaning $\tau_a = \tau_h = \tau_P$. This last limit actually requires a relaxation of the $\tau_R > \tau_a$ condition into a less restrictive $\tau_P > \tau_a$.

Additionally, the fact that we are in the $d'_P > 2x_0$ Regime, and therefore $n_a = 1$, makes τ_h actually independent on c_P: while in the $d'_P > 2x_0$ Regime, increasing c_P will increase the fraction of Rh6G which will attach/detach to PNIPAAm, therefore contributing to F_h. However, every single Rh6G contributing to F_h will still attach/detach to only one PNIPAAm chain ($n_a = 1$). As a result, the diffusion time of each Rh6G molecule will be altered by only one PNIPAAm interaction event *regardless of c_P*, until the threshold $d'_P = 2x_0$ (itself dependent on c_P through d'_P) is reached.

The relative error to τ_a is, factoring in the independent quantities involved:

$$\frac{\Delta \tau_a}{\tau_a} = \frac{\Delta D_R}{D_R} + \frac{\Delta D_P}{D_P} + \frac{\Delta \tau_h}{\tau_h} \qquad (6.16)$$

The $d'_P \leq 2x_0$ Regime adds complexity to this scheme, since while it's still $\tau_a \cong \tau'_a$, n_a is now a function depending on d'_P. It is, analogously to what seen in the $d'_P > 2x_0$ Regime,

$$\tau'_f = \tau_h - n_a \tau_a \qquad (6.17)$$

Analogously, the *cumulative* attached diffusion time (that is, the accumulated residence time for the n_a statistically observed PNIPAAm encounters per interacting Rh6G molecule) $\tau_a^* = n_a \tau_a$ is easily calculated as:

$$\tau_a^* = n_a \tau_a = \left(\frac{D_R - D_h}{D_R - D_P} \right) \tau_h \qquad (6.18)$$

Deriving τ_a or n_a from such is not possible unless the other is known beforehand. Luckily, one can experimentally obtain τ_a simply by measuring the system at lower c_P, that is in the $d'_P > 2x_0$ Regime. Given this, n_a can now be easily calculated as a ratio:

$$n_a = \frac{\tau_a^*}{\tau_a} \tag{6.19}$$

where of course τ_a is the value already calculated from the $d_P' > 2x_0$ Regime.

The $d_P' \leq 2x_0$ Regime adds, with respect to the $d_P' > 2x_0$ Regime, a n_a-mediated c_P dependency to τ_a^*, and therefore to τ_h. We have that, for sufficiently high c_P, and barring for a moment the eventuality of passing c_P^*, that n_a will rise from the $n_a = 1$ asymptote of $d_P' > 2x_0$ to a maximum value for which c_P is high enough that the considered Rh6G molecule immediately attaches to a new PNIPAAm chain upon detaching from the previous. Indeed, since in such a case Rh6G would be seen diffusing with τ_P, n_a will present a second asymptote value at $n_a = \frac{\tau_P}{\tau_a}$. As an additional note, in such a PNIPAAm-crowded environment, the free diffusion coefficient would most likely come to vanish.

As for the n_a error, it is easily

$$\frac{\Delta n_a}{n_a} = \frac{\Delta D_R}{D_R} + \frac{\Delta \tau_a}{\tau_a} + \frac{\Delta \tau_h}{\tau_h} \tag{6.20}$$

Further, it useful to stress again that $n_a > 1$ as seen in this Regime is a *statistical* value. As an example, an experimental situation presenting a free diffusion and a hybrid component with $n_a = 2$ would *not* mean that each Rh6G molecule attached either to 0 or 2 PNIPAAm chains during observation, but rather that Rh6G molecules either attached to 0 chains (due to either lack of collision or $l_a < 1$) or, in case of attachment, attached to a distribution of chains ranging from 1 to a number larger than 2, with 2 being the statistical average.

A further refinement of our analysis can be made now with the explicit calculation of l_c, which is necessary to the analysis of F_h. The l_c parameter can be thought of as the likelihood of one Rh6G molecule to come into contact with one PNIPAAm chain the center of which is not directly placed on Rh6G's trajectory. In the general sense, the larger the bodies involved in this kind of event, the higher the likelihood. Let's schematize Rh6G's trajectory as a line, and Rh6G as a sphere of hydrodynamic radius R_{HR}. A PNIPAAm chain, schematized as a sphere of hydrodynamic radius R_{HP}, can come into contact with such only in the case the two centers are at a distance $R_{HP} + R_{HR}$ or less. Let's call this cumulative radius R_A.

Since we placed ourselves in a Fickian model, our schematization of a Rh6G molecule's trajectory is a line. This is a relatively heavy simplification, but justified by the system's conditions: 1) Brownian diffusion; 2) absence of Rh6G-Rh6G collisions due to low concentration; 3) absence of long-range interactions with PNIPAAm. Under these conditions, we can expect trajectory fluctuations to be due to thermal noise alone, and therefore Rh6G trajectory to be random on a scale smaller than the one considered (until, of course, interaction with PNIPAAm verifies).

Let's consider a random Rh6G molecule entering the focal volume. As we already mentioned, we are placing tin a first approximation under the condition that we can consider Rh6G trajectories linear until interaction takes place.

Two situations can be delineated, again depending on the Regimes.

$d_P' \leq 2x_0$ Regime. In this Regime, the fraction F_h of observed Rh6G molecules which contribute to the hybrid signal is determined by c_P, l_a and l_c. Let's proceed by steps. Under our approximations, we can the product, $\dfrac{2x_0}{d_P}$, between $2x_0$ and the linear numeric PNIPAAm density $d_P^{-1} = c_P^{\frac{1}{3}}$, is the *maximum* number of PNIPAAm chains (under the very improbable condition that they are linearly distributed on Rh6G's trajectory) that a Rh6G can *encounter* - but not necessarily interact with - during diffusion in the focal volume. $\dfrac{2x_0}{d_P}$, if factored by l_c (the geometrical likelihood for one Rh6G molecule to

come into contact with a neighboring PNIPAAm chain), gives $l_c \dfrac{2x_0}{d_P}$, which is the *actual*

number of PNIPAAm chains that Rh6G will be likely come into contact with. Again, coming into contact doesn't necessarily mean attachment, for which we need to factorize

$l_c \dfrac{2x_0}{d_P}$ by l_a. The resulting expression for F_h is obtained:

$$F_h = l_c l_a \frac{2x_0}{d_P} = l_c \frac{2x_0}{d_P'} \qquad (6.21)$$

Going back now to the calculation of l_c, as our molecule enters the focal volume it will be, in a first approximation, at an effective distance between 0 and d_P' from the first neighboring PNIPAAm chain. The average effective distance to be traveled before such encounter is therefore $\dfrac{d_P'}{2} - R_A$, as shown in Fig. 21. Also shown in the same is how merely diffusing for $\dfrac{d_P'}{2} - R_A$ doesn't ensure an encounter.
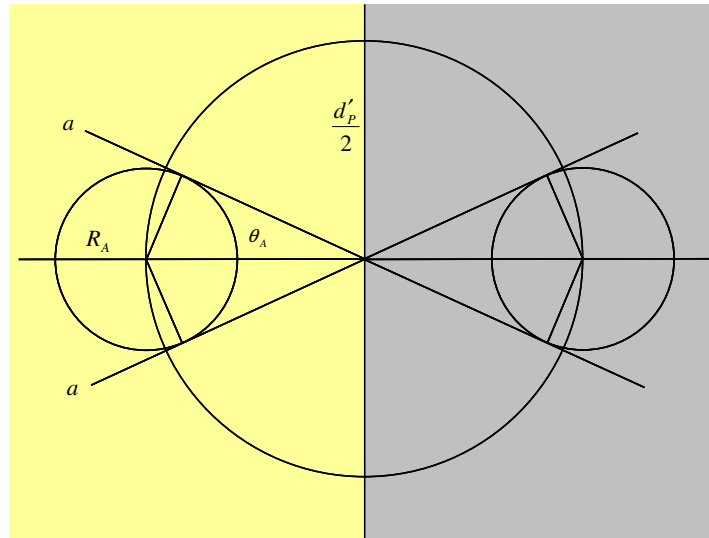

Fig. 21. Scheme of Rh6G diffusion into the focal volume, $d_P' \leq 2x_0$ case. Yellow half: focal volume; Grey half: unilluminated space. Rh6 diffuses from grey to yellow

As seen in Fig. 21, when at a distance $\frac{d'_P}{2}$ from the center of mass of particles disting d'_P, only two particles are allowed as closest neighbors, since the centers of mass of all other particles residing on the surface of the same sphere of radius $\frac{d'_P}{2}$ would dist less than d'_P from each other.

Since the Rh6G molecule diffuses in a random direction, the chance of encounter with PNIPAAm will be proportional to the angle subtended by the PNIPAAm-Rh6G spheres. Because of the axial symmetry of the system, the dependency is one-dimensional in said angle, and therefore we can restrict our analysis to a plane, as shown in Fig. 21. Symmetry also allows us to restrict the analysis of the upper left quadrant in Fig. 21. Including all the refinements so far, the angle θ_A subtended between the system axis and the edge of a PNIPAAm-Rh6G sphere (a lines in the figure) is

$$\theta_A = \arcsin\left(\frac{R_A}{\frac{d'_P}{2} - R_A}\right) = \arcsin\left(\frac{2R_A}{d'_P - 2R_A}\right) \tag{6.22}$$

The total angle subtended in the considered quadrant is, of course, $\frac{\pi}{2}$. Therefore, according to this model,

$$l_c = \frac{\theta_A}{\frac{\pi}{2}} = \frac{2}{\pi}\arcsin\left(\frac{2R_A}{d'_P - 2R_A}\right) \tag{6.23}$$

The same formula is also found to be valid in the case our diffusing molecule doesn't encounter the first neighboring sphere after entering the volume: in a general point inside the volume, the molecule will still be at an average $\frac{d'_P}{2}$ from neighboring spheres. Due to the already mentioned symmetry, Fig. 21 can again be used, calculation for l_c can again

be restricted to its upper left quadrant of the same figure, and therefore the same result stands.

As seen, l_c itself is a function of both l_a and c_P. Also, the general formula for F_h can now be used to factorize l_c out of it: if F_h is the overall fraction of Rh6G molecules contributing to the hybrid signal, and l_c is the geometrical likelihood of one Rh6G molecule to come into contact with a neighboring PNIPAAm chain, then $\dfrac{F_h}{l_c}$ can be thought of as *the number of PNIPAAm chains available for interaction with a Rh6G molecule within the focal volume assuming $l_c = 1$*. Which means, the number of chains that each Rh6G molecule belonging to F_h will statistically interact with during observation. In other words, $\dfrac{F_h}{l_c} = \dfrac{2x_0}{d'_P} = n_a$. This hypothesis will be tested further in this Experiment's treatment.

Explicitly it is for F_h:

$$F_h = l_c n_a = \frac{2x_0}{d'_P} \cdot \frac{2}{\pi} \arcsin\left(\frac{2R_A}{d'_P - 2R_A}\right) \tag{6.24}$$

simplifying and expressing which in terms of c_P:

$$F_h = \frac{4x_0 l_a c_P^{\frac{1}{3}}}{\pi} \arcsin\left(\frac{2l_a R_A c_P^{\frac{1}{3}}}{1 - 2l_a R_A c_P^{\frac{1}{3}}}\right) \tag{6.25}$$

l_c being, of course,

$$l_c = \frac{2}{\pi} \arcsin\left(\frac{2l_a R_A c_P^{\frac{1}{3}}}{1 - 2l_a R_A c_P^{\frac{1}{3}}}\right) \tag{6.26}$$

Since it is, generally, $d'_P - 2R_A > 2R_A$, F_h can also be linearly simplified to

$$F_h = \frac{4x_0 l_a c_P^{\frac{1}{3}}}{\pi} \frac{2l_a R_A c_P^{\frac{1}{3}}}{1 - 2l_a R_A c_P^{\frac{1}{3}}} = \frac{8x_0 l_a^2 R_A c_P^{\frac{2}{3}}}{\pi \left(1 - 2l_a R_A c_P^{\frac{1}{3}}\right)} \tag{6.27}$$

the dominant term of which has a $F_h \propto c_P^{\frac{2}{3}}$ dependency. If we now call this F_h $F_{h,C}$ to denote the fact that it is calculated, and we call $F_{h,M}$ its measured equivalent, we can directly calculate l_a by equating them:

$$F_{h,C} = \frac{8x_0 l_a^2 R_A c_P^{\frac{2}{3}}}{\pi \left(1 - 2l_a R_A c_P^{\frac{1}{3}}\right)} = F_{h,M} \tag{6.28}$$

The relative errors for such can be calculated under the hypothesis of independent variables as to obtain

$$\frac{\Delta F_{h,C}}{F_{h,C}} = \frac{\Delta x_0}{x_0} + 2\frac{\Delta R_A}{R_A} \tag{6.29}$$

The error for c_P wasn't factored in as the values where taken as nominal and therefore not measured *in situ*.

$d'_P > 2x_0$ Regime: In this case the effective PNIPAAm-PNIPAAm center of mass distance is effectively too large to be observed inside the focal volume, and therefore only a maximum of one PNIPAAm chain can be encountered by a linearly diffusing Rh6G molecule (i.e. $n_a = 1$, as already stated). The remarks concerning the general formulation

$F_h = l_c \dfrac{2x_0}{d'_P}$ are still valid, with the difference that, opposite to what seen in the $d'_P \leq 2x_0$

Regime, in the $d'_P > 2x_0$ Regime $\dfrac{2x_0}{d'_P}$ cannot be though of as n_a.

It is worth to elaborate on this last point before going further. As previously mentioned, n_a is a statistical value in the $d'_P \leq 2x_0$ Regime. However, such statistical value is the expression of a statistical distribution of finite, *integer* values: as an example, a $d'_P \leq 2x_0$ Regime system in which 50% of the hybrid diffusion is given by Rh6G interacting with 1 PNIPAAm chain during observation, and 50% is given by Rh6G interacting with 2 chains during observation will give $n_a = 1.5$. In the $d'_P > 2x_0$ Regime, on the other hand, the situation is much simpler: the only number of chains (again, an integer) that a Rh6G contributing to the hybrid signal can interact with is 1. There is no such thing as "interaction with less than one chain". If one wants, it's a quantization effect. Also, in the $d'_P > 2x_0$ Regime it is $\dfrac{2x_0}{d'_P} < 1$. Given that $n_a < 1$ is nonsensical, $\dfrac{2x_0}{d'_P}$

can't be taken as an estimate for n_a in this Regime.

We're now going back to the explicit calculation of l_c.

As we have said, a molecule entering the volume will not, for $d'_P > 2x_0$, perceive d'_P. Instead, the length scale involved will be $2x_0$: the one PNIPAAm chain which can be encounter will have its center of mass at a distance between 0 and $2x_0$ from Rh6G's entrance into the volume. As done for the $d'_P \leq 2x_0$ case, we take as average distance the half of the maximum one: x_0, as schematized in Fig. 22.
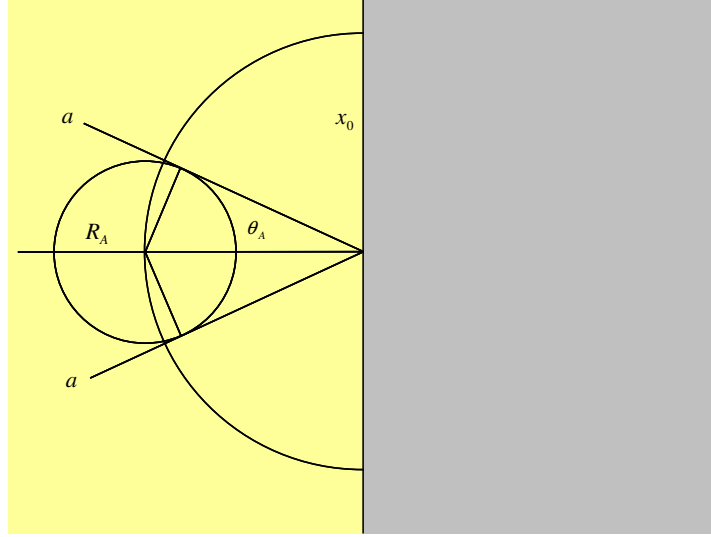
Fig. 22. Scheme of Rh6G diffusion into the focal volume, $d'_P > 2x_0$ case. Yellow half: focal volume; Grey half: unilluminated space. Rh6 diffuses from grey to yellow

Thanks to the system's symmetry, we again can restrict our calculation to the upper left quadrant shown in figure, and thus we have for the subtended angle:

$$\theta_A = \arcsin\left(\frac{R_A}{x_0 - R_A}\right) \tag{6.30}$$

so that l_c is now defined as

$$l_c = \frac{2}{\pi}\arcsin\left(\frac{R_A}{x_0 - R_A}\right) \tag{6.31}$$

In the $d'_P > 2x_0$ Regime, as opposed to the $d'_P \leq 2x_0$ one, the model cannot be extended beyond the chance of a first Rh6G-PNIPAAm encounter, since only one encounter is statistically possible. We have therefore, for $F_{h,C}$:

$$F_{h,C} = l_c \frac{2x_0}{d'_P} = \frac{4x_0 l_a c_P^{\frac{1}{3}}}{\pi}\arcsin\left(\frac{R_A}{x_0 - R_A}\right) \tag{6.32}$$

75

the linearly simplified version of which is

$$F_{h,C} = \frac{4x_0 l_a c_P^{\frac{1}{3}}}{\pi} \frac{R_A}{x_0 - R_A}$$

(6.33)

Notice how, in the $d'_P > 2x_0$ Regime, $F_{h,C} \propto c_P^{\frac{1}{3}}$, as opposed to the $F_{h,C} \propto c_P^{\frac{2}{3}}$ dependency observed for $d'_P \leq 2x_0$. That is, the focal volume size acts as a *threshold for the observed behavior*.

By equating the expression above to $F_{h,M}$, l_a can be calculated for $d'_P > 2x_0$ as

$$l_a = \frac{\pi}{4} \frac{F_{h,M} c_P^{-\frac{1}{3}}}{x_0 \arcsin\left(\dfrac{R_A}{x_0 - R_A}\right)}$$

(6.34)

or, in the linearly simplified version,

$$l_a = \frac{\pi}{4} \frac{F_{h,M} c_P^{-\frac{1}{3}}}{x_0 \dfrac{R_A}{x_0 - R_A}} = \frac{\pi}{4}\left(\frac{1}{R_A} - \frac{1}{x_0}\right) F_{h,M} c_P^{-\frac{1}{3}}$$

(6.35)

Analogously to what seen previously, the errors for the calculated quantities are

$$\frac{\Delta F_{h,C}}{F_{h,C}} = \frac{\Delta x_0}{x_0} + 2\frac{\Delta R_A}{R_A}$$

(6.36)

$$\frac{\Delta l_a}{l_a} = \frac{\Delta x_0}{x_0} + \frac{\Delta R_A}{R_A} + \frac{\Delta F_{h,M}}{F_{h,M}}$$

(6.37)

76

<u>Case 2</u>: $\tau_a > \tau_P$. In this case, τ_a is larger than the maximum diffusion time observed in the volume. As a result, τ_a cannot be determined from measurements. τ_a' for hybrid diffusion varies continuously from τ_R to τ_P. Again, the two Regimes can be differentiated:

$d_P' > 2x_0$ Regime: $n_a = 1$. In this Regime, d_P' is as invisible to the measurement as is τ_a. Excluding aggregate contribution, three diffusional behaviors will now in principle be observed for Rh6G: 1) free diffusion (D_R); 2) attached diffusion the entire observed time (D_P); 3) one attachment or detachment event during observation, leading to hybrid diffusion (D_h).

Under the described conditions, D_h is independent on d_P' (and therefore on c_P).

The equation,

$$D_h = F_f D_R + F_a D_P \qquad (6.38)$$

is still valid, but since neither τ_a and τ_f, can be fully observed during the observation time (the first due to $\tau_a > \tau_P$, the second due to $d_P' > 2x_0$) nothing can be inferred about the system's dynamics from diffusion coefficient analysis.

As for F_h, the same considerations stand as seen in the $\tau_R > \tau_a$ Case and $d_P' > 2x_0$ Regime, with the additional complication that, since it is now $\tau_a > \tau_P$, a non-negligible contribution is made to F_h by those Rh6G molecules attaching to PNIPAAm outside the focal volume and diffusing in before τ_a. Since, however, τ_a cannot be evaluated in the first place, this contribution is again unknown, and again nothing can be said about the system.

From an experimental point of view, what allows the measurer to qualitatively distinguish the $\tau_R > \tau_a$ Case from the $\tau_a > \tau_P$ Case under the $d_P' > 2x_0$ Regime is that, where for $\tau_R > \tau_a$ D_h will be very well defined, and closer to D_R than it is to D_P, in the $\tau_a > \tau_P$ its distribution is much wider, covering the whole range from D_R to D_P.

77

An intermediate Case, that is $\tau_P > \tau_a > \tau_R$, will show for $d'_P > 2x_0$ a behavior in between the previous two or, if one wants, a modification of the $\tau_R > \tau_a$ behavior in which D_h will exhibit an average value closer to D_P than in the $\tau_R > \tau_a$ Case, a broader distribution, but the values of which will always be higher than D_P.

$d'_P \leq 2x_0$ Regime. In this Case, as I mentioned, once a Rh6G molecule attaches to a PNIPAAm chain, it will travel attached to it until it exits the focal volume. Therefore, each Rh6G molecule either: 1) diffuses free; 2) spends its entire time through the volume attached to a chain; 3) attaches or detaches from one chain, spending the rest of time free; 4) detaches from one chain, diffuses freely, and then attaches to a second chain before exiting the focal volume. All the latter three possibilities depict a situation where Rh6G travels attached the whole observation time, except for the time it takes to travel between chains or between a chain and the edge of the focal volume. This distance varies from 0 to d'_P, and therefore the maximum time interacting Rh6G can spend free during observation is the already mentioned τ_f.

The situation in the system will appear similar to the $\tau_P > \tau_a > \tau_R$ Case, $d'_P > 2x_0$ Regime: the D_h distribution will exhibit a relatively large width, with the difference that D_h values will indeed reach as low as D_P.

Explicitly, the calculations here follow closely what seen for the $\tau_R > \tau_a$ Case, $d'_P > 2x_0$ Regime. Due to the $\tau_a > \tau_P$ condition, we have that the $n_a > 1$ condition has now a cap in $n_a = 2$. That is, $2 \geq n_a > 1$. Two Subcases must at this point be differentiated: Subcase 1, in which $2 > n_a > 1$, and Subcase 2, in which c_P is high enough to ensure $n_a = 2$. In Subcase 1, again nothing can be inferred about the system, since neither τ_a nor τ_f are visible to the system. In Subcase 2, however, we'll now have $\tau_f \cong \tau'_f$, similarly to what seen with τ_a and τ'_a in the $d'_P > 2x_0$ Regime. We'll just put ourselves then in Subcase 2, for which it is now $\tau_h = \tau_f + \tau'_a$. We have for the calculation of D_h:

$$D_h = \frac{\tau_f D_R + \tau_a' D_P}{\tau_f + \tau_a'} \tag{6.39}$$

We have, substituting $\tau_a' = \tau_h - \tau_f$, and again through calculations analogous to the $\tau_R > \tau_a$ Case, $d_P' > 2x_0$ Regime:

$$\tau_f = \left(\frac{D_h - D_P}{D_R - D_P} \right) \tau_h \tag{6.40}$$

the relative error of which can be calculated as, analogously to what seen in the $d_P' > 2x_0$ Regime:

$$\frac{\Delta \tau_f}{\tau_f} = \frac{\Delta D_R}{D_R} + \frac{\Delta D_P}{D_P} + \frac{\Delta \tau_h}{\tau_h} \tag{6.41}$$

Concerning $F_{h,C}$, its calculation is pointless, since in this Subcase, a system for which the $n_a = 2$ condition is ensured is a system for which the free diffusion component vanishes. If it weren't so, that is if there still existed the chance for Rh6G molecules to not attach to PNIPAAm during observation (0 attachment events) then, since n_a is a statistical value, and a continuous function of c_P, there would exist a residual fraction of the Rh6G population as well which only attached to / detached from 1 PNIPAAm chain during observation. This would, in turn, lower the overall statistical value of n_a to below 2, reverting the system to Subcase 1. Therefore, in Subcase 2 we have identically $F_{h,C} = 1$.

We can now apply the theory developed to the actual case of our measurements. As a first step, since we're attempting a quantitative analysis of the system, some data discrimination is necessary. Namely, we must decide how to handle the one experimental feature which we haven't touched so far in the Model's characterization: the aggregate

signal fraction. Since said aggregates comprise only a minor fraction of the signal (less than 10% for all Samples) and their contribution is not directly quantifiable, I opted for excluding them from the treatment. To this end, a correction is applied to $F_{h,M}$ in the form of a normalization to the total $F_{h,M} + F_{R,M}$, where $F_{R,M}$ is the measured signal fraction of the free Rh6G component. This way, excluding the aggregate component, $F_{h,M}$ is corrected to reflect the hybrid signal fraction of the total of Rh6G molecules *contributing to the sought after interaction*, and it is to this that I'll be referring to as $F_{h,M}$ in the rest of the treatment. Results are shown in Fig. 23 below.
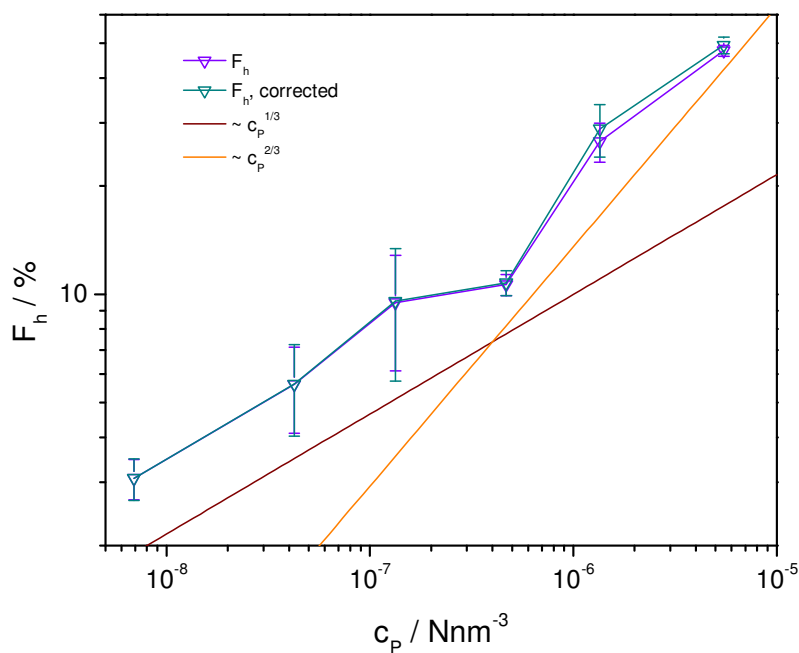
Fig. 23. Values for $F_{h,M}$, corrected and uncorrected with respects to aggregates presence. Although minor, the difference is felt more at high c_P

We can now delve into our quantitative analysis.

From a first observation of Fig. 17, two different behavior in D_h are observed: Samples 1 to 3 present a D_h apparently independent of c_P, with rather large error bars, a situation consistent with the $\tau_P > \tau_a > \tau_R$ Case, $d'_P > 2x_0$ Regime. For the same Samples,

one has in Fig. 23 that $F_{h,M}$ presents a c_P dependency which can be easily fitted as

$$F_{h,M} \propto c_P^{\frac{1}{3}}.$$

Samples 4 to 6, on the other hand, present a different behavior. In Fig. 17, a clear dependency on c_P is shown for D_h. Consistently, in Fig. 23 $F_{h,M}$ can be fitted as

$$F_{h,M} \propto c_P^{\frac{2}{3}}.$$

Also, as Fig. 17, Fig. 18 and Fig. 23 show, a signal consistent with free Rh6G diffusion is present in every Sample.

To summarize, overall behavior is consistent with the $\tau_P > \tau_a > \tau_R$ Case and, more in detail, Samples 1 to 3 behave according to $d_P' > 2x_0$ both in D_h and $F_{h,M}$, while Samples 4 to 6 behave according to $d_P' \leq 2x_0$.

The first step of the quantitative analysis of the studied system can then be performed on diffusion coefficient data. Assuming $d_P' > 2x_0$, $n_a = 1$ for Samples 1 to 3, the corresponding equation, (6.15), was applied for the calculation of τ_a. As for Samples 4 to 6, equation (6.18) was applied, and n_a calculated as $n_a = \dfrac{\tau_a^*}{\bar{\tau}_a}$, where $\bar{\tau}_a$ is the weighted average of τ_a over Samples 1 to 3. Results are shown in Fig. 24 below. While and independent confirmation of said values is lacking at this point in the calculations, a confirmation of the theory's coherence the physical significance of n_a will come further during the F_h analysis. For now, one can see how the obtained τ_a value indeed matches the first, qualitative $\tau_P > \tau_a > \tau_R$ hypothesis based on the simple observation of Fig. 17.

As we'll see further in the treatment, these values will require further adjustment and a further refinement of the model. For now, though, they can be taken as a good approximation in need of independent confirmation.
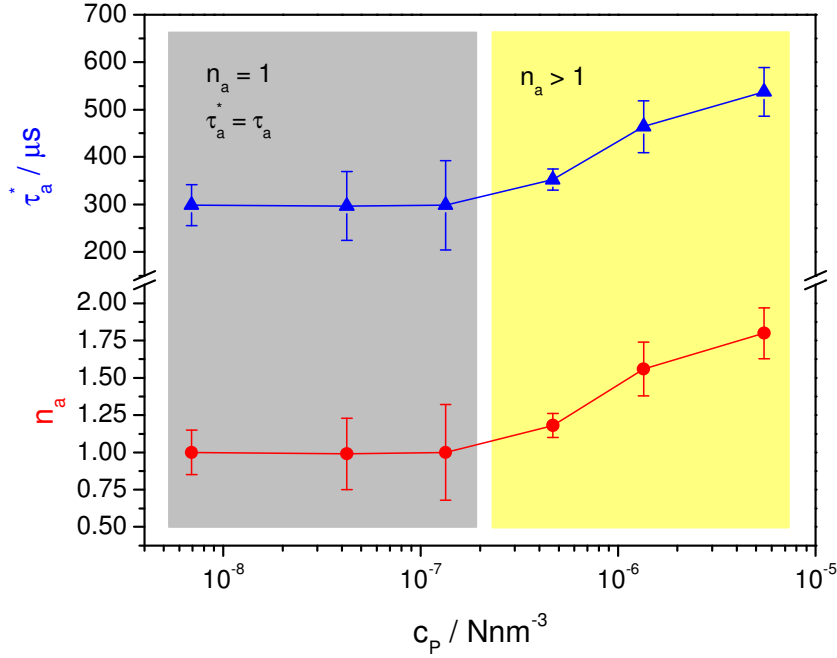
Fig. 24. Comparison of calculated τ_a^* (top half); comparison of calculated n_a, where $\bar{\tau}_a$ required for n_a calculation was averaged from the first 3 τ_a^* data points. Data uncorrected for l_s factor. l_s will be addressed further in the treatment

Confirmation of said values can come if we pass from diffusion coefficient analysis to signal fraction analysis. In the signal fraction analysis, a calculation of l_a for the system can at this point be attempted, as presented in Fig. 25, where Samples 1 to 3 have l_a calculated according to the $d_P' > 2x_0$ form.

As expected, l_a appears as a constant over the considered values, with a weighted average value of $l_a = 0.64 \pm 0.03$. On the basis of this piece of theory, I could therefore place the Rh6G-PNIPAAm attachment likelihood upon contact as $l_a = 64 \pm 3\%$. Which is believable, considering the well-known Rh6G tendency towards adhesion to anionic objects. Also, the fact that, although relatively high, l_a is far below 1 accounts for the observed slight decrease in D_R with increasing c_P: at high c_P, as Rh6G is diffusing in an increasingly more viscous medium, the subsequent collisions with PNIPAAm chains

cause attachment and hybrid signal in 64% of the cases, and a very moderate collision-induced slowing down in the remaining 36%.
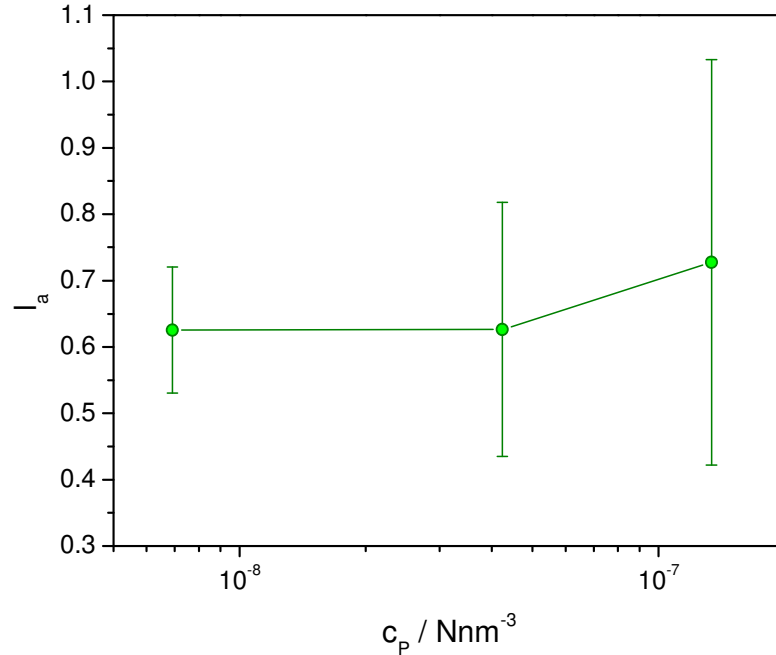

Fig. 25. l_a factor over Samples 1 to 3

It is also noteworthy how $l_a = 0.64 \pm 0.03$ yields the calculated $d'_P = 2x_0$ threshold between the $d'_P > 2x_0$ and $d'_P \leq 2x_0$ Regimes not between Samples 3 and 4 ($d'_P =$ 308 and 203 nm versus $2x_0 = 366$ and 371 nm respectively – the different $2x_0$ values here are due to the experimental setup oscillations between measurement sessions) but rather between Samples 2 and 3 ($d'_P =$ 451 and 308 nm versus $2x_0 =$ 366 and 371 nm respectively). It should be kept in mind once again, however, that the d_P values used in calculation of said d'_P are extracted from purely nominal c_P. Concerning this, one should take into consideration for increasingly high c_P the increasing percentage of increasingly large aggregates observed during diffusion. Said aggregates have been explicitly neglected in this treatment for two reasons: 1) the little signal fraction; 2) the fact that FCS can only provide information on diffusion times and, though this, on diffusion coefficients and radii, but not on mass or density. As a result it was not possible to know

what percentage of the nominal c_P was contributing to the aggregates, being therefore subtracted from the actual chain concentration which generates the hybrid signal. Consequently, as it will be shown further in the treatment of this Experiment, this has a major effect on the calculation at high c_P of highly c_P dependent quantities such as the hybrid signal's fraction - a fact that has to be taken account of.

Also worth noticing is that no model contradiction was apparent in the τ_a and n_a calculations, which were based entirely on data measured *in situ*. Indeed, the major difference between consistent and inconsistent data is the addition of an *a priori* datum (c_P) in the calculation of the latter.

Similarly to what done for l_a, the model can now be tested on an explicit calculation of F_h. Taking $l_a = 0.64 \pm 0.03$, $F_{h,C}$ is now calculated, again basing ourselves on the different $d'_P > 2x_0$ and $d'_P \leq 2x_0$ equations, (6.32) and (6.25), for the two different Regimes.
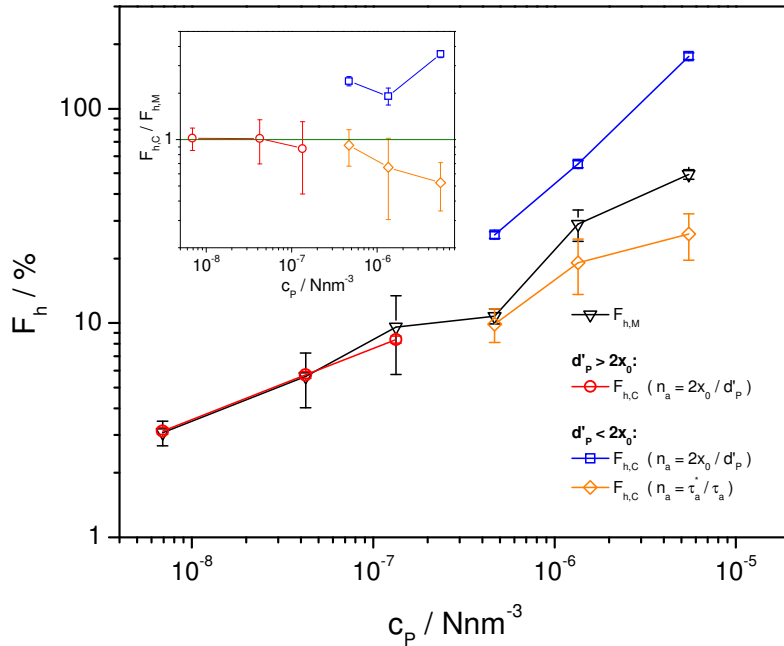

Fig. 26. Comparison between $F_{h,C}$ and $F_{h,M}$ (inverted triangles) over both $d'_P > 2x_0$ and $d'_P \leq 2x_0$ c_P ranges. Inset: $F_{h,C}/F_{h,M}$ ratio. n_a values uncorrected for l_s factor (l_s will be addressed further in the treatment)

84

As seen in Fig. 26, it is easy to see how values for the $d'_P \leq 2x_0$ Regime, calculated as described (blue squares), heavily fail to adhere to experimental data, with values not only inconsistent with experimental data, but physically nonsensical as well ($F_{h,C} > 100\%$ for Sample 6). This is again easily ascribed to the aggregate presence, that is the discrepancy between nominal and factual c_P, as already seen in the treatment of the nominal versus factual threshold between the $d'_P > 2x_0$ and $d'_P \leq 2x_0$ Regimes a couple of pages back. Indeed, not only is the $d'_P \leq 2x_0$ Regime the one where the c_P decrease from its nominal value is highest due to the aggregates' presence, but also the Regime where the c_P dependency on $F_{h,C}$ through l_c is strongest.

The problem can be easily solved by going beyond the limitations imposed by the use of the calculated d'_P. This can be done by substituting the calculated $n_a = \dfrac{2x_0}{d'_P}$ for the $d'_P \leq 2x_0$ Regime with the experimental $n_a = \dfrac{\tau_a^*}{\tau_a}$ as extracted from D_h analysis for the same Regime (see Fig. 24, page 82), so that the forms

$$F_{h,C} = l_c n_a \qquad (6.42)$$

$$l_c = \frac{2}{\pi} \arcsin\left(\frac{2R_A}{d'_P - 2R_A}\right) = \frac{2}{\pi} \arcsin\left(\frac{2R_A}{\dfrac{2x_0}{n_a} - 2R_A}\right) \qquad (6.43)$$

become

$$F_{h,C} = l'_c \frac{\tau_a^*}{\overline{\tau}_a} \qquad (6.44)$$

$$l'_c = \frac{2}{\pi} \arcsin\left(\frac{2R_A}{2x_0 \dfrac{\overline{\tau}_a}{\tau_a^*} - 2R_A}\right) = \frac{2}{\pi} \arcsin\left(\frac{R_A}{x_0 \dfrac{\overline{\tau}_a}{\tau_a^*} - R_A}\right) \qquad (6.45)$$

85

and it is, under the hypothesis of independent variables again,

$$\frac{\Delta F_{h,C}}{F_{h,C}} = \frac{\Delta x_0}{x_0} + 2\frac{\Delta R_A}{R_A} + 2\frac{\Delta n_a}{n_a} \tag{6.46}$$

As again shown in Fig. 26, the adherence to $F_{h,M}$ with the above modified formulas (orange diamonds) is much higher, contributing to confirming the various aspects of the model and theory as consistent. However, we see that the model still fails to correctly mimic the experimental datum at Sample 6, and indeed heavy deviation between $F_{h,C}$ and $F_{h,M}$ can be seen in Sample 5 already.

To further correct this inaccuracy, and refine the model, one can take into account the fact that the simplification $\tau_a \cong \tau_a'$, which the model we use is based upon, holds better the smaller the actual residence time τ_a is, and that, strictly speaking, τ_a will always be larger than the observed τ_a' ($\tau_a > \tau_a'$). Also, one must remember that what we can observe is actually τ_a', not τ_a. In other words, this model is much more accurate for the $\tau_R > \tau_a$ Case than for the $\tau_P > \tau_a > \tau_R$ Case. The smaller τ_a is, both in the $d_P' > 2x_0$ and $d_P' \leq 2x_0$ Regimes, the higher the chance will be to observe τ_a in its entirety during the observation time. Conversely, given a long enough τ_a, a non-negligible chance will arise that the Rh6G molecules we observe contributing to the hybrid signal routinely either exit the focal volume before τ_a is elapsed, or enter the focal volume before τ_a is elapsed; in other words, a non-negligible chance to observe τ_a' sensibly smaller than the real τ_a.

Since the $\tau_P > \tau_a > \tau_R$ Case is that in which we find ourselves, we'll have that the actual estimation of τ_a we make is afflicted by a statistical deviation, which I'll now address.

Since the threshold to the observation times in the system is determined by the size of the volume, $2x_0$, the effect being treated must be reasoned in terms of length scales. Given the equation

$$\tau_a = \frac{x_a{}^2}{4D_P} \qquad (6.47)$$

one easily finds that

$$x_a = 2\sqrt{D_P \tau_a} \qquad (6.48)$$

which is the average half-distance a Rh6G molecule diffuses while attached to PNIPAAm. This can be now compared to the typical length scale of the focal volume, $2x_0$, to obtain a new parameter, l_s, which describes the likelihood that an attached molecule observed attaching either exits the focal volume before τ_a is elapsed, or enters the focal volume before τ_a is elapsed.

$$l_s = \frac{2x_a}{2x_0} = \frac{2\sqrt{D_P \tau_a}}{x_0} \qquad (6.49)$$

In other words, l_s is the likelihood we have of observing a partial τ_a in the interacting Rh6G population. This in turn contributes to the statistics of the system, lowering the average measured τ'_a.

Since a partially-observed τ_a will be comprised between 0 and τ_a, we can place, in a first approximation, the average for such at $\frac{\tau_a}{2}$.

Let's put ourselves in the simple condition of the $d'_P > 2x_0$ Regime, for which $n_a = 1$. As a result of what considered, we'll have for that a fraction l_s of interacting Rh6G will give us $\tau'_a = \frac{\tau_a}{2}$, and the remaining $1 - l_s$ fraction a $\tau'_a = \tau_a$. Adding both fractions, we'll have for the apparent $\tilde{\tau}_a$:

$$\tilde{\tau}_a = \left(1 - l_s\right)\tau_a + l_s \frac{\tau_a}{2} = \left(1 - \frac{l_s}{2}\right)\tau_a \qquad (6.50)$$

That is, the actual τ_a will be

$$\tau_a = \frac{\tilde{\tau}_a}{\left(1 - \dfrac{l_s}{2}\right)} \qquad (6.51)$$

Unluckily, what we have access to is $\tilde{\tau}_a$ alone, and not l_s. However, substituting the explicit expression for l_s in the previous formula we have that

$$\tilde{\tau}_a = \left(1 - \frac{l_s}{2}\right)\tau_a = \left(1 - \frac{x_a}{2x_0}\right)\tau_a = \left(1 - \frac{\sqrt{D_P \tau_a}}{x_0}\right)\tau_a = \tau_a - \frac{\sqrt{D_P}}{x_0}\tau_a^{\frac{3}{2}} \qquad (6.52)$$

By substituting $u = \sqrt{\tau_a}$ this can now be written as a cubic expression:

$$\frac{\sqrt{D_P}}{x_0}u^3 - u^2 + \tilde{\tau}_a = 0 \qquad (6.53)$$

Solutions for the above expression can be calculated numerically, by inserting the so-far obtained values for $\tilde{\tau}_a$ (298.3 ± 0.2 µs), D_P ((1.31 ± 0.02)·10^{-7} cm²s⁻¹) and x_0 (average value: $\bar{x}_0$ = 181 ± 4 nm). 3 different solutions are given for u, leading to 3 different solutions for $\tau_a = u^2$: τ_{a1} = 40.0 ms; τ_{a2} = 275 µs; τ_{a3} = 328 (± 9) µs. Both τ_{a1} and τ_{a2} are unrealistic, since $\tau_{a1} > \tau_P$ (where the average for τ_P is $\bar{\tau}_P$ = 573 ± 8 µs) and $\tau_{a2} < \tilde{\tau}_a$ (which is nonsensical). τ_{a3}, on the other hand, is an allowed value ($\tau_P > \tau_{a3} > \tilde{\tau}_a$), and close enough to $\tilde{\tau}_a$ to realistically represent the sought-after correct

value. One can also calculate $2x_a$ as 262 ± 5 nm according to equation (6.48), where the error was calculated as

$$\frac{\Delta x_a}{x_a} = \frac{1}{2}\frac{\Delta D_P}{D_P} + \frac{1}{2}\frac{\Delta \tau_a}{\tau_a} \tag{6.54}$$

where $\dfrac{\Delta \tau_a}{\tau_a}$ is the relative error of the newly calculated τ_a:

$$\frac{\Delta \tau_a}{\tau_a} = \frac{\Delta \tilde{\tau}_a}{\tilde{\tau}_a} + \frac{1}{2}\frac{\Delta D_P}{D_P} + \frac{\Delta \bar{x}_0}{\bar{x}_0} \tag{6.55}$$

It also follows that the value for l_s is, for this system, can be now calculated for each x_0 seen in the measurement series, as plotted below, in which the errors were calculated as

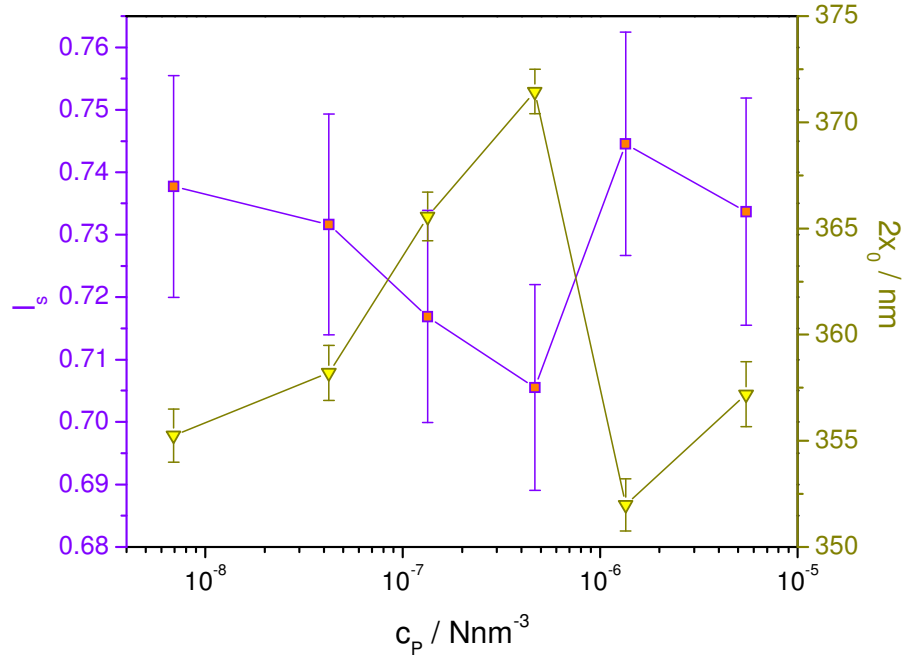$$\frac{\Delta l_s}{l_s} = \frac{\Delta \tau_a}{\tau_a} + \frac{\Delta x_0}{x_0} \tag{6.56}$$

Fig. 27. The inverse proportionality of l_s to $2x_0$ is illustrated. l_s: squares; $2x_0$: triangles

It is worth noting how l_s, as illustrated in Fig. 27, is intrinsically an expression of both the PNIPAAm-Rh6G interaction itself and of the observation length scale, $2x_0$. As a comparison, l_c is a function of the Rh6G-PNIPAAm interaction, of c_P and $2x_0$ combined, while l_a, although it requires knowledge of $2x_0$ to be evaluated, is purely an expression of the interaction.

This said, the new correction for τ_a has to be extended to the $n_a > 1$ Regime, since our evaluation of n_a must now also be revised. Let us call now $\tilde{\tau}_a^*$ the measured collective attached time, as obtained from (6.18). Similarly, let's call $\tilde{n}_a$ the average number of interaction measured as $\tilde{n}_a = \dfrac{\tilde{\tau}_a^*}{\tilde{\tau}_a}$ (what we referred so far as $n_a = \dfrac{\tau_a^*}{\tau_a}$), as opposed to the actual n_a. Two Subregimes need to be described at this point:

$2 \geq n_a > 1$: this is the Subregime in which each interacting Rh6G molecule will, for the purpose of our statistical n_a, interact with a maximum of 2 PNIPAAm chains. Since we don't know at what points in space and time during the diffusion this happens, each of the maximum 2 chains can be affected by the artifact described for $\tilde{\tau}_a$. As a result, the same considerations apply as in the $n_a = 1$ Regime:

$$\tilde{\tau}_a^* = n_a \tilde{\tau}_a \tag{6.57}$$

$$n_a = \tilde{n}_a = \dfrac{\tilde{\tau}_a^*}{\tilde{\tau}_a} \tag{6.58}$$

which can be directly calculated with the values already obtained, and whose error can be calculated as $n_a = \dfrac{\tau_a^*}{\tau_a}$ in the previous iteration of the treatment.

$n_a > 2$: in this Subregime each interacting Rh6G molecule will, for the purpose of our statistical n_a, interact with more than 2 PNIPAAm chains. As a result, only the first and

the last chains in the series of n_a encounters can have their τ_a altered via the effect treated here; all other Rh6G-PNIPAAm interactions (the ones happening in between) will begin and end entirely within the focal volume. As a result, we'll have then that the total $\tilde{\tau}_a^*$ will be given for this Subregime, on average, by the sum of two contributions: the first, coming from those interaction events likely to be affected by the artifact, will be 2 times $\left(1-\dfrac{l_s}{2}\right)\tau_a$ (analogously to what seen for the $n_a=1$ Regime); the second, coming from the n_a-2 interactions unaffected by the artifact, will be $(n_a-2)\tau_a$. Thus,

$$\tilde{\tau}_a^* = 2\left(1-\frac{l_s}{2}\right)\tau_a + (n_a-2)\tau_a = (n_a-l_s)\tau_a \tag{6.59}$$

And as a result, n_a can now be simply derived from previously calculated values as

$$n_a = \frac{\tilde{\tau}_a^*}{\tau_a} + l_s \tag{6.60}$$

where it bears reminding that now τ_a is the corrected, actual residence time value.

To determine whether the system is in the $2 \geq n_a > 1$ or $n_a > 2$ Subregime, the experimenter should first calculate the corrected τ_a from $\tilde{\tau}_a$ in the $n_a=1$ Regime, and l_s from it. Based on this, the experimenter should then calculate n_a as described by the expression above. If above 2, the expression above is the correct one for n_a. If lower than 2, then $\tilde{n}_a = \dfrac{\tilde{\tau}_a^*}{\tilde{\tau}_a}$ should be taken as the correct value for n_a.

Applying the described corrections to our data, we see that $F_{h,C}$ is now consistent with $F_{h,M}$ for all Samples, as illustrated in Fig. 28.
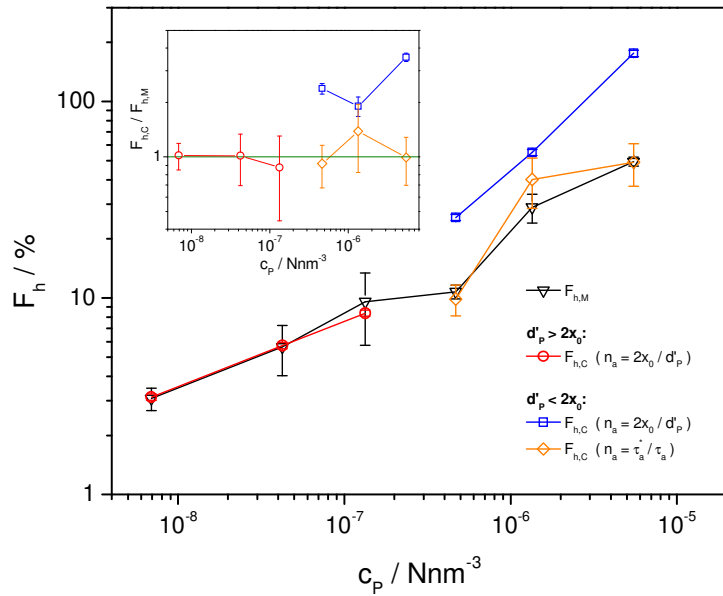
Fig. 28. Comparison between $F_{h,C}$ and $F_{h,M}$ over both $d'_P > 2x_0$ and $d'_P \leq 2x_0$ c_P ranges. n_a corrected for l_s factor
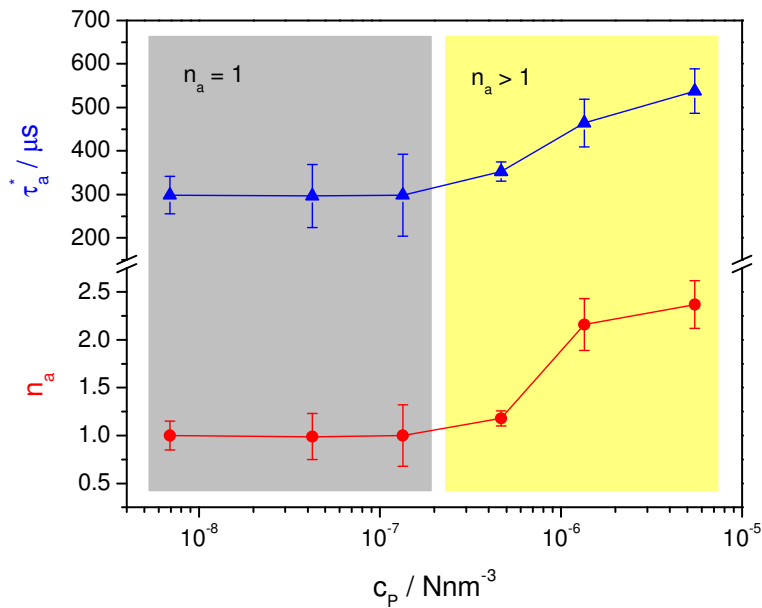

Fig. 29. Comparison of calculated τ_a^* (top half); comparison of calculated n_a, where $\bar{\tau}_a$ required for n_a calculation was averaged from the first 3 τ_a^* data points. Data corrected for l_s factor

Fig. 29 shows the τ_a and n_a data at Fig. 24 including the newly implemented corrections.

As a final parameter evaluation, and confirmation of the theory's consistency, one can now evaluate the average distance Rh6G molecules diffuse between a detachment from a PNIPAAm chain and the attachment to the next, *regardless of the observation span*. This distance, which we call $2x_f$ (twice the half-distance between attachments/detachments, to keep in line with the established "half distances" lingo first established with x_0) will simply be the average distance between PNIPAAm chains, normalized by l_a and l_c. As a result, and keeping to the methods refined so far for the two Regimes, one has for the $d_P' > 2x_0$ Regime ($n_a = 1$):

$$2x_f = \frac{d_P'}{l_c} = \frac{c_P^{-\frac{1}{3}}}{l_a l_c} \tag{6.61}$$

the error of which can be calculated through

$$\frac{\Delta x_f}{x_f} = \frac{\Delta l_a}{l_a} + \frac{\Delta R_A}{R_A} + \frac{\Delta x_0}{x_0} \tag{6.62}$$

For the $d_P' \leq 2x_0$ Regime ($n_a > 1$) one has:

$$2x_f = \frac{2x_0}{l_c' n_a} \tag{6.63}$$

due to the better representation of actual chain-chain distance in this Regime through n_a than through the nominal c_P. n_a is, again, calculated including all the refinements described so far. The error for this expression can be calculated through

$$\frac{\Delta x_f}{x_f} = 2\frac{\Delta n_a}{n_a} + \frac{\Delta R_A}{R_A} + 2\frac{\Delta x_0}{x_0} \tag{6.64}$$

and the values for $2x_f$ can now be plotted for a quick comparison with the typical length scale of the observation volume, as shown in Fig. 30 below, in which the fact that $2x_f$ always keeps above $2x_0$ acts as a support of the experimental persistence of the free Rh6G signal in all Samples:
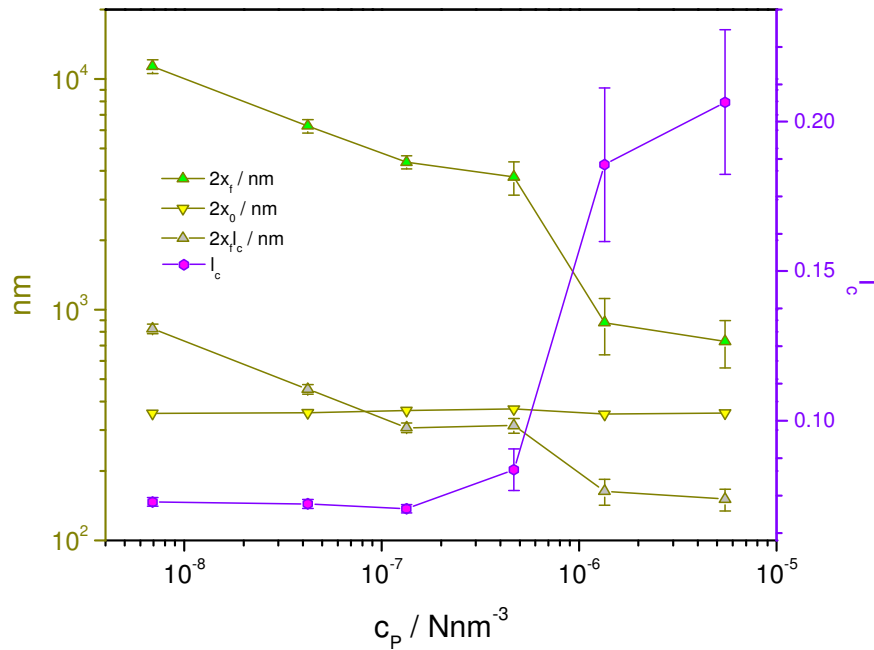
Fig. 30. Comparison between typical length scales as derived from measurement and developed theory and l_c factor. Left Y axis: distances. Right Y axis: l_c

Also for comparison $2x_f l_c$ is added, that is, the simple average chain-chain distance normalized by l_a. One can easily see how the direction single Rh6G can diffuse into plays a crucial role in increasing the length Rh6G molecules will go, on an average, without interacting with chains: if l_c were not a factor, i.e. if it could be put to 1, then the simple l_a-normalized chain-chain distance would result in the free Rh6G component vanishing by Sample 3. Physically, this would imply that every Rh6G would actually be

guaranteed to find PNIPAAm molecules at regular $2x_f l_c$ intervals along its diffusion trajectory, which is of course blatantly unrealistic.

To summarize the results, the model developed and presented in the treatment of this Experiment is internally coherent and fit to evaluate the characteristics of the studied system, with the caveat that the $d'_P \leq 2x_0$ regime present a heightened sensitivity to c_P, and relative deviations between theoretical and practical values. Similar use of the model, and relative caution, can in the future be applied to other systems to be studied.

In this context, observation of c_P dependency in D_h and subsequent n_a evaluation are a more trustable source of data than calculated d'_P is for the purpose of establishing the $d'_P > 2x_0$ and $d'_P \leq 2x_0$ Regimes. Therefore, D_h analysis should be performed as the first step of FCS-based interaction analysis as described in this Experiment.

A protocol is therefore detailed for system interaction characterization:

1. Perform FCS on mixed solution: constant fluorescent or fluorescent-labeled body concentration (Body 1), variable interactive body concentration (Body 2)

2. Perform FCS on labeled Body 2 in absence of Body 1, or obtain D of such through different means, such as PCS

3. Fit signals obtained at point 1 for 2 Fickian components: free Body 1 plus hybrid signal. Include aggregate signal if necessary. Normalize $F_{h,M}$ to $F_{h,M} + F_{1,M}$, where $F_{1,M}$ is the signal fraction of free Body 1

4. *Residence time τ_a extraction*: identify $d'_P > 2x_0$, $n_a = 1$ Body 2 concentration (c_2) range as the range where D_h is independent of Body 2 concentration, c_2. Calculate τ_a through equations (6.15), (6.49) and (6.51) in order to correct for l_s factor

5. *Attachment likelihood l_a extraction*: calculate l_a for the $d'_P > 2x_0$, $n_a = 1$ c_2 range through equation (6.34)

6. *Number of attachment events n_a extraction*: identify $d'_P \leq 2x_0$ range. Calculate τ_a^* from said range through equation (6.18) and n_a through equation (6.58) or (6.60) depending on the Subregime.

6.5.   Conclusions

This study presented in the treatment of this Experiment was successful in providing a method to an estimation of elusive properties such as the statistical attachment time and the likelihood of interaction of different species in a wet environment, and can be anticipated to be useful in analogous systems to characterize the interaction of diffused species in a solution. In short, both a physical model and practical method were developed which can be used to probe a wide variety of systems.

Furthermore, the findings described here can be applied to better characterize the diffusion in more complex systems like, for instance, hydrogels, as was the problem solving aim originally sparking the Experiment. Indeed, properties like the residence time τ_a or the attachment likelihood l_a for a given interactive system, once derived in solution, could be turned from a hindrance to a tool to evaluate other elusive properties typical to gels, such as mesh size and structural inhomogeneities.

The method, although it could benefit from external, independent confirmations, is internally consistent and supported by theoretical calculations, as shown.

As for the immediate purpose of our hydrogel study, the study presented in this chapter excludes interacting (or indeed, attracting) probes for the time being. Completely non-charged dyes, on the other hand, are not soluble in water, and would likely display a tendency towards aggregation if they were (due to minimization of the surface energy). As a result, it was decided to adopt moderately repulsive-interacting - i.e. moderately anionic - probes for the hydrogel project. Although the repulsive interaction could lead to alteration in the perceived mesh size, it was theorized that a zero-sum interaction could be present inside the gel for repulsive diffusants, as opposed to the observed glue-like effect for attractive interaction. As it was to be observed (section 8.3.2.1, page 151), this was the case.

7. Experiment 2: Size-dependent diffusion in inverse opals

7.1. Motivation

The second in our side projects, this study consisted in the modeling of size-dependent diffusion of non-interacting probes in a known environment. The aim of this was to derive a theoretical model for such a phenomenon which, apart from the intrinsic interest, could help us derive a theoretical model with which to interpret slowdown diffusion in the gels. To this end, it was decided to study the diffusion of known objects in a known environment, so as to try and extract a general law of diffusion in confined spaces. The slowdown

The study here described focuses on the modeling of a diffusional process as general as possible and, in this sense, the sought-after conditions were the simplest possible: non-interacting hard sphere diffusing in a regular array.

The environments chosen for diffusion were a series of inverse opals (iOpals) as described in section 5.3.5 (page 43), while the diffusants were chosen as fulfilling the requirements of non-interactivity with the system (both the iOpals and the diffusants possessing negative charge, thus preventing attractive interaction, as per the results of Experiment 1) and being modeled as hard spheres.

The conditions studied in this Experiment (non-interactive diffusion in small-void iOpals) are also complementary to what recently studied in house at the MPIP by Cherdhirankorn et al.[38], whose inquiry focused on diffusion in large-void iOpals (thus making it non-statistical to begin with) of environment-interacting diffusants.

Beyond the starting scope of this Experiment, implications of its results can be of great advantage in the modeling of diffusion in closely confined systems, a field which both has recently raised to major interest and the applications of which are of considerable impact upon new developments in applied science[39,40,41,41b].

7.2. Experimental

The FCS setup employed was the one described in section 5.1 (page 33) for Experiment 2. Attofluor chambers were employed for the measurements. All measurements were conducted at room temperature (nominally 21 ± 1 ℃).

Previous to observation, the iOpals were cleaned in etOH, let dry at room temperature, and mounted in the chambers. Subsequently, 600 µl of HEPES buffer were added, followed by 150 each of Alexa 647 and one of the Qdot species, both at a concentration of 120 nM, thus allowing for optimal FCS concentration for both in the system once diffusion was complete. Diffusion of the fluorescents was monitored at time intervals until a time-constant fluorescence signal was observed in the iOpals. 30 mins was the maximum time necessary for this process to complete.
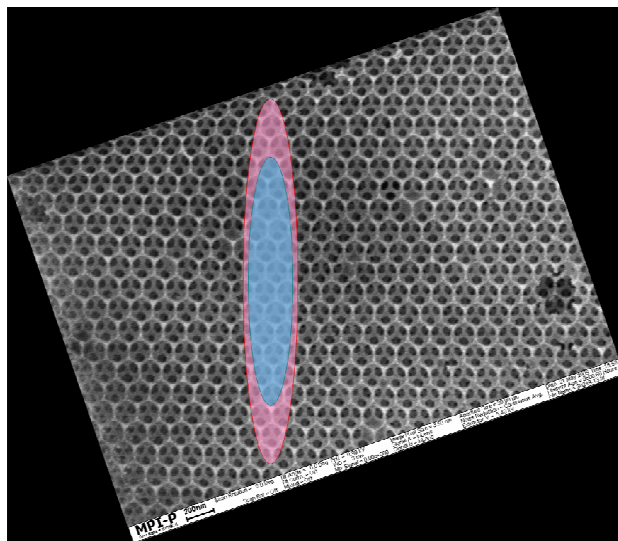
Fig. 31. SEM image of $180SiO_2$. Superimposed in scale are the typical dimensions of the focal volumes employed. Pink: channel 1. Pale blue: channel 2

Fig. 31 pictures the characteristic sizes of the focal volumes for channels 1 and 2 in comparison with typical iOpal dimensions. The iOpal pictured is $180SiO_2$. Dimensions for the focal volumes were calculated with calibration data in the pure solvent. Channel 1 was used to excite Alexa 647, while channel 2 was used to excite Qdots.

The comparatively small voids of the iOpals make it so that a number of voids in the tens was at any moment inside the focal volumes. This allowed for a statistical behavior of the diffusion inside the iOpals which, combined with the regularity of the structures and the larger size of the iOpal compared to the focal volumes, allowed for an independence of the observed phenomena on the probed spot.

All measurements in this Experiment were performed in the described HEPES buffer at room temperature, due to the employed Qdots being stable only in a limited 7 - 9 pH range.

Diffusion experiment were performed with 4 differently-sized tracers, the spherical Qdots 525 to 585, and the molecular tracer Alexa 647, itself approximated as a rigid sphere for modeling purposes, on the 3 different iOpal variants described at 5.3.5 (page 43). Table 4, following here, reports iOpal typical sizes (already reported at 5.3.5) and the diffusants. As for the iOpal characteristic sizes, refer to Table 1 (page 45).

	Alexa647	Qdots525	Qdots545	Qdots585
R_h (nm)	1.3	8.8	9.2	9.8
Core	Molecular dye	CdSe	CdSe	CdSe
Shell	Molecular dye	ZnS	ZnS	ZnS
Coating	Molecular dye	Amphiphilic Polymer (unspecified)	Amphiphilic Polymer (unspecified)	Amphiphilic Polymer (unspecified)
Surface modification	Molecular dye	Carboxylic groups (c/a 100)	Carboxylic groups (c/a 100)	Carboxylic groups (c/a 100)

Table 4. Details of the probes diffusing in the iOpals

Before every measurement session, the FCS setup was calibrated with a 20 nM solution of both Rh6G and Cy5 in water. The calibration solution was measured in a separate Attofluor chamber and on a glass slide previously cleaned according to the method described at page 120. The same cleaning procedure was also routinely applied to all Attofluor chamber after each measuring session. Additionally, the chamber used for calibration was kept separate from the ones used for sample measurement and cleaned in a separate environment. This was due to the use of Rh6G in said chamber, whose high cationic nature and notorious persistence in environments held a chance of contamination if mixed with the other systems.

$I(t)$ was typically recorded from 2.5 min, for diffusion in pure solvent with strong fluorescence, to up to 10 minutes in the iOpals, the longer measurement times being employed for the larger Qdots, which due to their size diffused through the iOpals in minor number, and the $G(t)$ of which presented larger deviation on smaller time scales, thus requiring longer measurement times to observe the required average behavior. These total accumulation times were subdivided in 30-seconds intervals in order to enable removal of occasionally erroneous signals due to aggregates.

All $G(t)$ curves were fitted excluding the data points up to ~ 10 µs for Alexa 647, beyond the triplet effect time range, thus allowing for an exclusion of the triplet contribution parameters from the fit. In the case of Qdots, on the other hand, it was my care to include as much of the signal as possible, especially at small times, since the characteristic signal artifact for quantum dot diffusion (*blinking*) is not limited to a time range. As a result, as detailed in section 7.3 following, the part of the experimental $G(t)$ in which the blinking effect is best observed is the non-baseline part in which the unperturbed $G(t)$ is flat, i.e. the beginning of the curve.

To this end, for Qdot diffusion $G(t)$ was fitted starting from ~ 1 µs, which is the near entirety of $G(t)$ excluding the first 2 - 3 data points, which usually suffer from setup-related artifacts and consequently add a further, unwanted degree of data dispersion.

Thanks to the double channel setup employed, both Alexa 647 and the Qdot species of choice for each measuring session could be observed diffusing at the same time in the system. Especially advantageous in this sense is the fact that all 3 Qdots species possessed emission spectra within the Channel 2 range of the setup, thus allowing for a clean separation of the Alexa and Qdot signals without trouble.

7.3.   Blinking effect and FCS theory re-engineering

Before delving into data analysis and simulation comparison, a necessary data extraction refinement needs to be addressed, concerning quantum dots, their peculiar fluorescent properties, and the optimal way to handle them in order to avoid experimental

artifacts. As the Experiment treated in this section has quantum dots as a pivotal element, the development of said refinement was an especially crucial step.

At the nanometer length scale, molecular dyes offer an optimal solution, provided they don't interact with the system. However, as different sized probes show heightened slowdown sensitivity to system features of comparable size, one may find themselves in need of probes order of magnitude larger, as it was our case.

Quantum dots easily answer to this requirement, as many varieties of species are commercially available, with size spanning the 10-100 nm range. Although originally engineered as biological staining agents rather than for FCS purposes, some of the FCS-crucial requirements they show are happy byproducts of their original purpose. For example, the original staining target makes them available in a number of differently functionalized variants, which usually grants the presence of a uniform surface charge. This, in turn, both prevents aggregation and unwanted adhesion to same-sign charged environments. Even more crucial, since the quantum effect responsible for their fluorescence is regulated by quantum spatial confinement, their monodispersity is granted by the necessity to have them emit at a specific wavelength.

Despite such favorable features, the use of quantum dots as FCS probes has been so far extremely marginal, if not nonexistent. The main reason for this can be attributed to the intrinsic emission effect known as *blinking*.

Disturbance, intrinsic (i.e. not translational) signals are not new to the FCS user, as described in section 4.1 (page 21). However, blinking is more troublesome than the more common triplet, since whereas triplet exhibits a typical time, there is no recorded typical time for blinking: quantum-based fluorescents like quantum dots will exhibits on-off time ranging from nanoseconds up, the limit being the total measurement time itself in the case of immobilized quantum dots, or the maximum recorded time of flight through the focal volume in the case of diffusion.

Fig. 32 below illustrates, a one-component Fickian fit of monodisperse quantum dots in solution yields poor results. The materials are from the same stock as used in the rest of this thesis' experiments: the described HEPES buffer (section 5.3.2.3.2, page 37) and

quantum dots - the latter, specifically Qdots 545. The general expression for triplet-free $G(t)$ was used:

$$G(t) = 1 + \frac{1}{N} \frac{1}{\left(1+\dfrac{t}{\tau}\right)\sqrt{1+\dfrac{t}{S^2\tau}}} \tag{7.1}$$
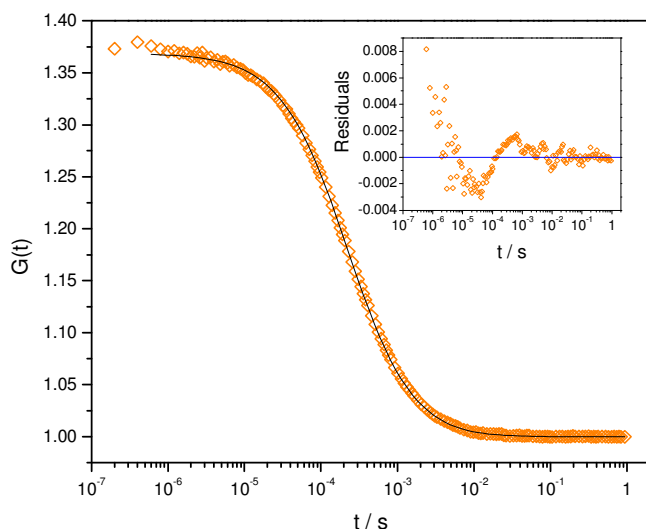

Fig. 32. $G(t)$ for Qdots 545 diffusing in HEPES buffer. Fit function: uncorrected for blinking effect. Solid line: fit curve. Inset: fit residuals

The above curve was fitted from the third data point (0.6 μs) to encompass the time range where triplet would present itself. Although curve and fit can appear acceptable at a glance, it is the fit's residuals that reveal the inaccuracy. In a pure, undisturbed diffusing regime and for monodisperse objects, in such range the function should present a flat plateau, as evidenced by the fit curve. Instead, a slope is present, and the residuals present a clear sinusoidal pattern.

Various empirical methods can be employed to clean the residuals of the clearly non-random pattern, and thusly efficiently use quantum dots as FCS probes, with various degrees of success and plausibility. These range from reintroducing an effective triplet

102

effect factor, to additional corrective decay components, to stretched exponentials (i.e. modeling the diffusion as non-Fickian), to simply ignoring the blinking disturbance.

Assuming for a moment to simply neglect the blinking effect, the diffusion time obtained from the above fit is 221.4 ± 0.8 µs.

Since the blinking handling methods described above were not felt to be grounded in plausible theory, relying mostly on empirical correction, I set to modify the fitting function otherwise.

As described in section 4.1 (page 21), a system's $G'(t)$ can be expressed as the product of a diffusional and an intrinsic component. This is the basis of the implementation of the commonly accepted triplet correction, and it is where I set to reengineer $G(t)$ in function of blinking.

Various studies[42,43,44] have been conducted on blinking luminescence, mostly focusing of immobilized quantum dots. The common result of these studies is the power-law dependence of time of the blinking effect, which matches with its lack of a characteristic time. Verberk et al.[43] derive a simple expression for the $G'(t)$ of immobilized quantum dots:

$$G'(t) = A\left(1 - Bt^{2-m}\right) \tag{7.2}$$

with A describing the overall amplitude of the effect, B the strength of the power law dependency, and m the dependency itself. For capped quantum dots, such as we use, m is known[42] to vary in the $1.7 - 1.9$ range depending on the system.

When factored with (4.15), (7.2) gives

$$G'(t) = A\left(1 - Bt^{2-m}\right)\frac{1}{N}\frac{1}{\left(1+\dfrac{t}{\tau}\right)\sqrt{1+\dfrac{t}{S^2\tau}}} \tag{7.3}$$

Since, ideally, no blinking should affect the function at time 0, we should have

103

$$G'(0) = \frac{1}{N} \frac{1}{\left(1 + \frac{0}{\tau}\right)\sqrt{1 + \frac{0}{S^2\tau}}} = \frac{1}{N} \qquad (7.4)$$

On the other hand,

$$G'(0) = A\left(1 - B0^{2-m}\right)\frac{1}{N} \frac{1}{\left(1 + \frac{0}{\tau}\right)\sqrt{1 + \frac{0}{S^2\tau}}} = A\frac{1}{N} \qquad (7.5)$$

We therefore set $A = 1$ for the purposes of (7.2) being used as blinking correction effect in our treatment, thusly normalizing the correction factor. Reintroducing the baseline and multiple components we obtain a general expression for $G(t)$ in a system affected by blinking:

$$G(t) = 1 + \frac{1}{N}\left(1 - Bt^{2-m}\right)\left(\sum_i \frac{F_i}{\left(1 + \frac{t}{\tau_i}\right)\sqrt{1 + \frac{t}{S^2\tau_i}}}\right) \qquad (7.6)$$

As the blinking properties are known[42] to vary depending on the quantum dots' structure, environment, excitation intensity, and observation time, both B and m were left as free fitting parameters, with the added constraint $B > 0$ in order to prevent unrealistic, divergent values for the corrective term,

Refitting the curve at Fig. 32 again with the newly modified function yields, for a one-component Fickian diffusion, the results at Fig. 33.
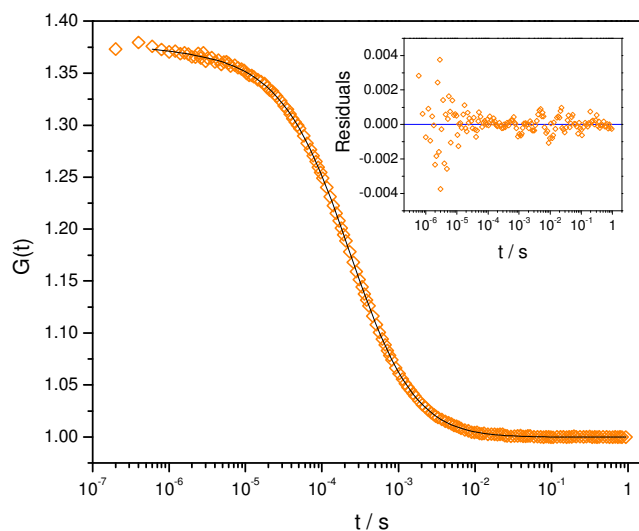
Fig. 33. $G(t)$ for Qdots 545 diffusing in HEPES buffer. Fit function: corrected for blinking effect. Solid line: fit curve. Inset: fit residuals

Notice, in Fig. 33, the much more contained, flat and random residuals. Concurrently, the initial slope of $G(t)$ is faithfully followed. The newly obtained diffusion value is 245 ± 4 µs. The larger fitting error of such value is explained in the light of the 2 additional parameters (m and B) included in the fit. Nonetheless, the obtained value differs by an 11% from the previously calculated value. The use of the implemented correction is therefore substantial to the ends of actual data evaluation, and as such was included in the standard method for all quantum dot based measurement in the treatment of the present Experiment.

Fitted values for the new parameters were, for the analyzed curve, $m = 1.85 \pm 0.05$ and $B = 0.7 \pm 0.2$. m, in particular, is in full agreement with data reported in literature[42].

As a final note concerning the employed blinking correction, it is recommended to include as many initial $G(t)$ points as possible for the fit when dealing with such cases, as this is the time range where the time dependence of the correction factor is most evident due to the plateau behavior of the undisturbed diffusional contribution. Therefore, the first data points are especially useful to fit a correct m and B values.

7.3.1. Data simulation

Simulations of the diffusion were conducted by Arash Nikoubashman (Vienna University of Technology) and Christos N. Likos (University of Vienna). In these, a standard Brownian dynamics simulation approach was adopted, in order to simulate the diffusive behavior of a small spherical particle (radius a), which is embedded into an iOpal the voids of which possess radius R and opening diameter L, where a, R and L were equated to the values reported in Table 1 (page 45) and Table 4 (page 99). A similar experimental approach was recently adopted by Loppinet et al. in the study of star-like micelle suspensions[45].

An example of the described formalism in relation to the physical configuration of the iOpals can be seen in Fig. 34, where on the left side only one opening is shown to simplify the notation, and on the right side one actual void (which display 12 holes) is reported. The angle of aperture is then defined as $\vartheta_0 = \arcsin\left(\dfrac{L}{2R}\right)$, and the distance of

the opening from the void's center as $h = \sqrt{R^2 - \dfrac{L^2}{4}}$.
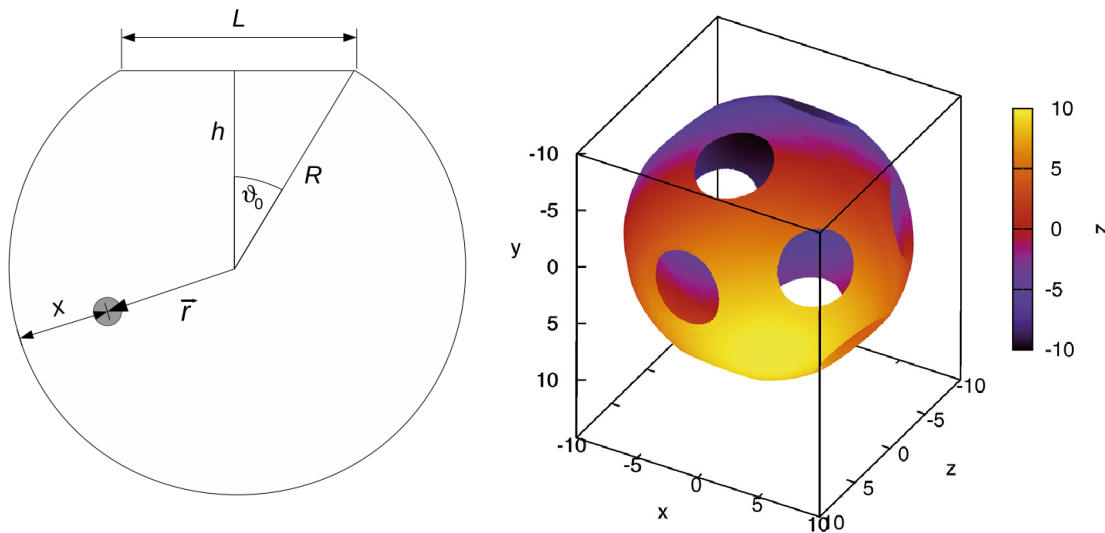

Fig. 34. Schematic representation of a confining capped sphere (an iOpal's constituting void) with one opening (left), and actual inverse opal employed in the simulations (right)

Since the Reynolds number, *Re* of such a colloidal system is rather small (i.e. viscous forces dominate over inertial forces), the movement of the particle can be considered as completely overdampened. Under these conditions, the equation of motion reduces to:

$$\vec{r}(t + \Delta t) = \vec{r}(t) + \Delta t \frac{D_S}{k_B T} \vec{F}(\vec{r}) + \vec{r}_G \tag{7.7}$$

Here, D_S denotes the short-time diffusion coefficient, k_B Boltzmann's constant, and $\vec{F}(\vec{r})$ the force exerted by the confining cavity. The vector $\vec{r}_G$ is a random variable drawn from a bivariate Gaussian distribution with zero mean value and variance given by $\sigma_r^2 = \sqrt{2 D_S \Delta t}$.

In the simulations, the particle-wall interactions were modeled via a shifted Yukawa-like potential[46], which constitutes the norm to represent screened electrostatic interaction such as we expect to have between out diffusants and the iOpals:

$$U(\vec{r}) = U(x) = \varepsilon \frac{e^{-2\frac{x}{a}}}{(x-a)^2} \tag{7.8}$$

where *x* denotes the shortest distance between the particle's center and the inverse opal. Such a potential was chosen in order to simulate a simple short-range repulsive interaction between the diffusant bodies and the iOpal surface, thus preserving the Brownian nature of the diffusion inside the voids.

The Stokes-Einstein equation was used to relate the short-time diffusion coefficient D_S to the drag coefficient $\xi = 6\pi\eta a$, leading to rewriting the Stokes-Einstein equation in the form:

$$D_S = \frac{k_B T}{\xi} \tag{7.9}$$

in which a is naturally the radius of the body diffusing in the system. Evidently, for free particles, the long-time diffusion coefficient, D_{free}, coincides with D_S. However, this does not hold up anymore in the confined case.

In the simulated treatment, all lengths are expressed as fractions of R and it was put $\varepsilon = k_B T$ constant in (7.9).

The simulation process was based upon the transition between two limit cases based on the $\dfrac{L}{R}$ ratio which, together with the number of openings per void (12, for our iOpals) determines the likelihood that a diffusing body has of escaping the void. We can refer in this sense to the *escape area*: the available area on the void's inner surface through which a diffusant can escape the void. If the escape area approaches the surface area of the void (that is, in the limit, theoretical case in which the void's surface consisted only of holes, i.e. in which no solid surface existed), then the escape time for a body, τ_{esc}, would simply equal the time it takes said body to diffuse from one end of the void to the other. We can refer to this time as τ_{free}. The opposite extreme case would be an escape volume which is 0 (that is, in which there is no opening in the cavity). In such a situation τ_{esc} would diverge to infinity. The transition between the described limit cases is what was simulated by Nikoubashman and Likos. In the simulations, other than L and R determining the escape area conditions, the factor a plays two roles: the first, the determination of the diffusing bodies' D through the well-known Stokes-Einstein equation; the second, a modifier to the escape area: the larger a, the smaller one can consider the escape area to become at fixed L and R.

In order to analyze the transitional regime, the mean escape time $\langle \tau_{esc} \rangle$ of the embedded particle was simulated, where the brackets, $\langle ... \rangle$, denote an ensemble average. The diffusion in the inverse opal was then modeled as a random walk of step $\sim R$ and waiting time τ_{esc}, leading to the result $D = \dfrac{R^2}{6\tau_{esc}}$. In the case of a free particle, this leads to the well-known $D_{free} \propto a^{-1}$ proportionality through

$$\tau_{esc} = \tau_{free} = \frac{R^2 \pi \eta a}{k_B T} \qquad (7.10)$$

Also, a timescale τ_0 was extracted from this relation, defined as

$$\tau_0 = \frac{\pi \eta R^3}{k_B T} \qquad (7.11)$$

to rewrite equation (7.10) in the form $\tau_{esc} = \frac{a}{R} \tau_0$, which is exact for a free particle ($\tau_{esc} = \tau_{free}$). In an aqueous solution at room temperature values can be predicted as $\tau_0 \sim$ 1ms for environment such as we have (approximating $R \sim 100$nm).

No hard-and-fast equations are available for the explicit relationship between a, R and L towards the calculation of τ_{esc} for a confined (non-free) body, as the simulation method relies on numerical simulations through the aforementioned Yukawa potential. In this sense, the reader is invited to refer to the reported references[45,46] for additional insight.

Fig. 35 exemplifies typical results of simulations. In it, it was put $L = \frac{2}{3} R$ as a first, tentative approximation of the values in Table 1.

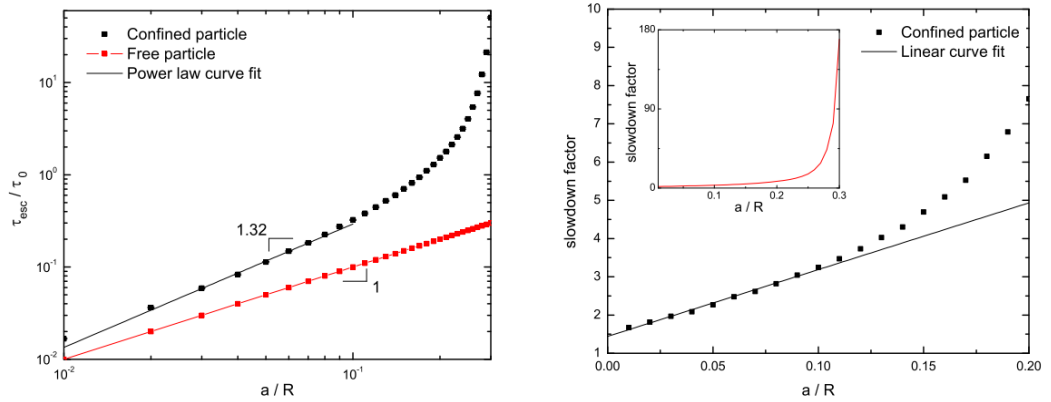
Fig. 35. Example of calculated τ_{esc} and τ_{free} (left) and their ratio, the slowdown factor (D_0/D, right). Inset to right graph: long a/R range representation of slowdown factor behavior. Sample values used: $L = \frac{2}{3} R$

In Fig. 35 one can observe a consistent power-law behavior for $\dfrac{\tau_{free}}{\tau_0}$, as it was expected. A power-law behavior also approximates $\dfrac{\tau_{esc}}{\tau_0}$ for the confined particle, but only at small values. As a/R increases beyond ~ 0.1 (that is, as the diffusing body's size becomes more comparable with the system's size) a power law is unable to represent $\dfrac{\tau_{esc}}{\tau_0}$ for the confined particle. Indeed, in the general case $\dfrac{\tau_{esc}}{\tau_0}$ would logically need to diverge to infinity for $a = \dfrac{L}{2}$ (diffusing body too large to fit through a hole) which, in this case ($L = \dfrac{2}{3}R$), equates $a = \dfrac{R}{3}$, as confirmed by the inset to the right graph in the Figure.

The slowdown factor Fig. 35 refers to is simply $\dfrac{\tau_{esc}}{\tau_{free}}$, and equates to what, experimentally, I refer to in terms of diffusion coefficients as D_0/D, where D_0 is the diffusion coefficients of a diffusing body as experimentally observed in the free solution, and D its diffusion coefficient as experimentally observed in the iOpal.

Notice, however, that the graphs at Fig. 35 are purely reported as examples of the simulation output, and being based on arbitrary numbers are not meant to represent diffusion in the experimentally employed iOpals.

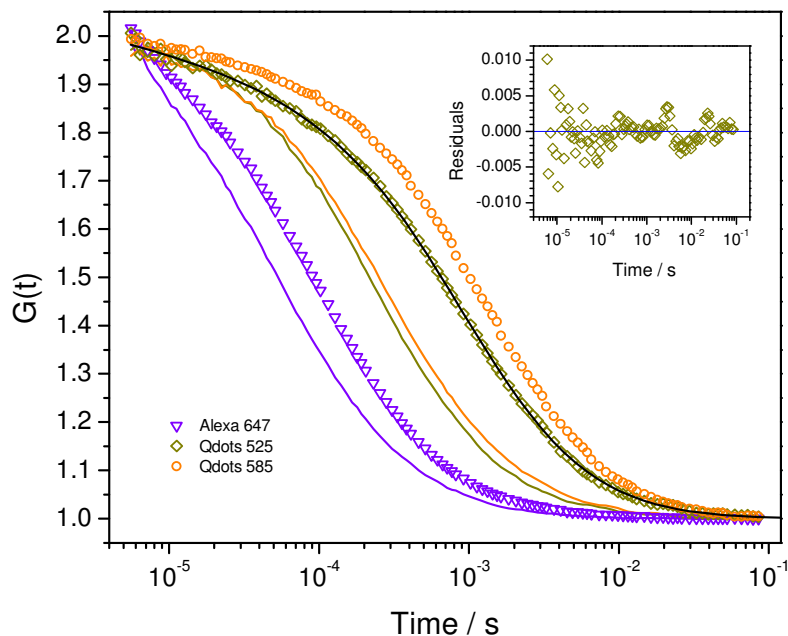## 7.3.2. Diffusion in iOpals and experimental-simulation comparison

Fig. 36. $G(t)$ of differently-sized probes in $180SiO_2$ iOpal (symbols) and free solution (continuous lines). Inset: residuals from the blinking-corrected, single Fickian component fit of $G(t)$ for Qdots 525 in the iOpal, which is also reported in black in the main graph

Fig. 36 shows examples of $G(t)$ curves for the diffusion of typical probes into $180SiO_2$. Symbols refer to diffusion in the iOpal, while continuous lines to diffusion in the solvent. The incremental slowdown with increasing particle size is evident. The inset reports an example of typical residuals for the fitting of $G(t)$ in an iOpal. In this case, Qdots525. The mentioned fitting was calculated for one Fickian component, corrected for the blinking effect.
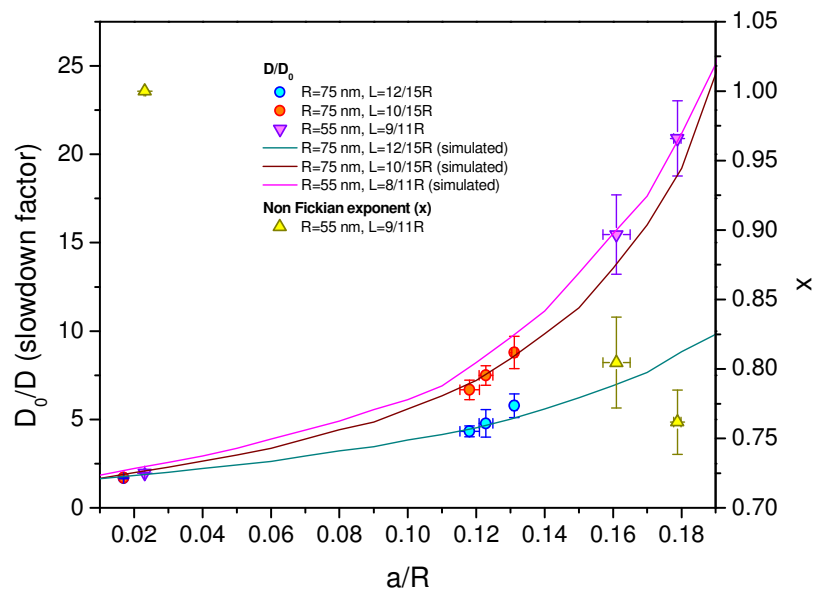
a)
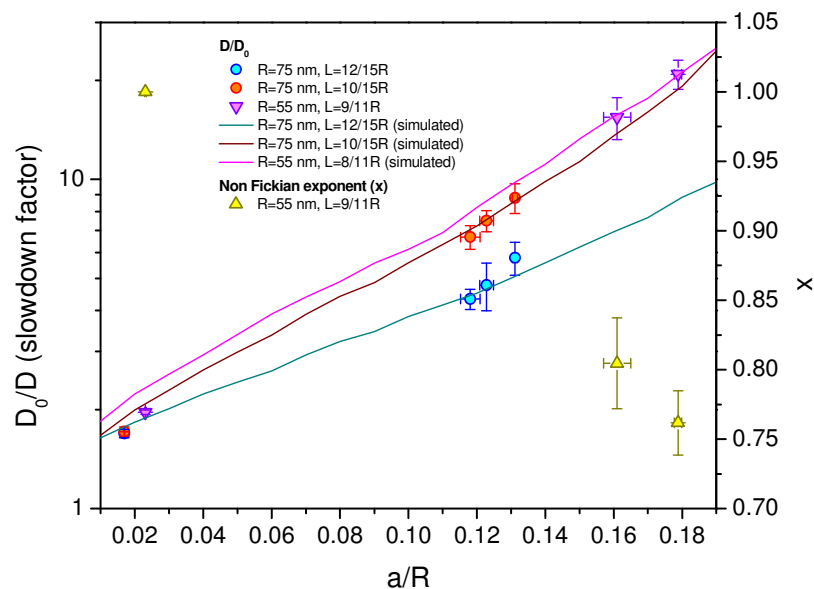
b)

Fig. 37. Comparison of slowdown factor as function of a/R for the three iOpals: symbols correspond to experimental data; continuous lines to simulation data. D_0/D axis: a) linear b) logarithmic. b) evidences the poorer experimental-simulation matching at low a/R as compared with high a/R

Fig. 37 above provides a comparison between experimental data and theory-based simulation. The three iOpals described in section 5.3.5 (page 43) were employed. Slowdown has been plotted as function of diffusant radius a, normalized to void radius R. All diffusion results as one-component Fickian, expect for what observed in the 130SiO$_2$ iOpal. For this, only Alexa 647 gives one Fickian diffusion process, while quantum dot diffusion yields results that can be best fitted either as a single non-Fickian signal. The diffusion time for the latter was fitted through a modified version of the $G(t)$ function:

$$G(t) = 1 + \left(1 - Bt^{2-m}\right)\frac{1}{N}\frac{1}{\left(1 + \left(\frac{t}{\tau}\right)^x\right)\sqrt{1 + \frac{1}{S^2}\left(\frac{t}{\tau}\right)^x}} \tag{7.12}$$

Which is the blinking-corrected version of $G(t)$ modified for non-Fickian processes:

$$G(t) = 1 + \frac{1}{N}\frac{1}{\left(1 + \left(\frac{t}{\tau}\right)^x\right)\sqrt{1 + \frac{1}{S^2}\left(\frac{t}{\tau}\right)^x}} \tag{7.13}$$

The material 130SiO$_2$ is composed of - silica - is the same as the other two iOpals, and as all other material elements - buffer and diffusants - are also the same, the different behavior needs be attributed to the different length scales.

Also noteworthy is how experimental slowdown for the 130SiO$_2$ iOpal diffusion is best simulated, as seen in Fig. 37, with a L value smaller than the real one. This might hint to a stronger repulsion effect that assumed actually being in effect between the diffusing bodies and the iOpals, the effect of which manifests in a sensible fashion at high a/R (and therefore a/L) values.

The non-Fickian nature of high a/R diffusion deserves a small commentary, since it is in apparent contradiction with the previously mentioned statistical nature of diffusion in the iOpals. We can attribute the non-Fickian behaviour at high a/R to the increasingly

dominant shape effect coming to being in such a regime. That is, at low a/R the diffusants can be thought of as a point-like object, and therefore can experience the environment simply as a probabilistic ensemble of obstacles, and therefore the dominant slowdown mechanism is random, Brownian collision. At high a/R, on the other hand, The diffusants are large enough to be influenced in their motion by the shape of both chambers and holes. A much higher chance is present, in other words, for them to "roll around" a chamber until they can enter the next through a hole. In such a regime, direction of motion plays a much more important role than in the low a/R case.

Indeed, the smaller a/R, the larger the number of allowed directions of diffusion a particle has to pass through a hole, which leads to a greater chance of a large number of deflections in the next chamber before the next hole is entered, which ensures a random trajectory over the ~10 chamber the diffusant crosses before exiting the focal volume.

Conversely, the higher a/R, the smaller the number of allowed directions for the diffusion through a hole. In the limit $a = \dfrac{L}{2}$, i.e. diffusant size equal to hole size, the only way for the diffusant to pass to the next chamber would be to "bullseye" the hole in a trajectory perpendicular to the chamber-chamber separation wall. This, in turn, given the regular geometry of the chambers, would lead to the next chamber being passed immediately, and so on. In other words, every first "bullseye" event would determine the rest of the diffusion, assuming a perfectly regular structure. That is, a much larger number of regular chambers is necessary to effectively randomize the diffusion of particles in the case in which a is close to $\dfrac{L}{2}$.

In the real case, $a < \dfrac{L}{2}$, and therefore the result is not as extreme as in the $a = \dfrac{L}{2}$ case, and therefore the result is in between the $a = \dfrac{L}{2}$ case and the point-like case, as observed.

7.4. Conclusions

The experiment yielded good results both in terms of adherence between theory and experimental data, and subsequent extrapolation of a model. Furthermore, the fact that the model is dependent on a relatively simple, relatively intuitive theory makes it a good candidate to indeed function as a general model for diffusion in more complex systems.

Interestingly, the model adheres best to experimental data in the large probe range, whereas the simulated D_0/D curve fail to reproduce the behavior of the smallest diffusant, Alexa 647. In particular, the substantial independence, for Alexa 647, of D_0/D on L, with just a dependence, if relatively weak, on R.

8. Experiment 3: PNIPAAm hydrogel nanostructure and dynamics for biosensing implementation

8.1. Motivation

Hydrogels, three-dimensional crosslinked polymer networks capable of imbibing huge quantities of water, have recently gained large exposure thanks to their properties, which are placing them center stage for such diverse applications as drug delivery systems[47,48,49,50,51,52] sensors[2,3,4,5,6,53,54,55,56], and synthetic tissue[57]. In the field of sensors in particular, interest has raised concerning surface attached, quasi-1D swelling gels. Biosensors gels need to be easily stored and replaced, and to allow fast diffusion of solutions. To these ends, the physical form of thin, anchored discs is optimal. Despite relatively widespread usage of 1D-swelling gels in current sensing technology, however, an intimate understanding of the mechanisms and detailed architectures underlying the known properties is still missing[58].

Also, the existence of both asserted behavioral resemblances[59] of the gels in swollen state to polymer solutions beyond the overlap concentration (transient networks) and differences[30] from said solutions make further fundamental research necessary.

Among hydrogels, poly-N-isopropylacrylamide (PNIPAAm) has proven of particular interest due to the high swelling ratio R_S and stability[29a], and the presence of a well-defined, easily accessible lower critical solution temperature (LCST) exhibited at around 32 ºC, above which the chains switch from hydrophilic to hydrophobic, phase separation is attempted by the crosslinked structure, and the gel collapses. Grafted PNIPAAm layers on solid substrates, in particular, offer a platform for sensor applications. Parameters known to alter the behavior of gels in general, and of PNIPAAm gels in particular, are temperature[55,29a,9,60,11], the solvent they're swollen in[61], and pH in case of water-based buffers[53,8,62,11], and efforts towards model-based, multi-variable structural and dynamic analysis have been attempted[63,64,65].

Particularly attention is being paid to how the gel behaves in different solvents because of the impact on relevant properties like R_S and, consequently, microscopic- and submicroscopic-scale behavior. Of paramount importance for the mentioned sensor applications is the penetration and mobility of analytes, which in turn intimately depend on the hydrogels structure at different length scales. For a disordered soft system this structural elucidation requires a spatiotemporal study of the hydrogel/diffusant system, since the gel structure can impact differently the guest mobility due to specific host-guest interactions. The charged nature of hydrogels makes the system complex with a rich behavior, also considering its response to several external stimuli.

A number of studies have been conducted in order to investigate the structure and dynamics of hydrogels, covering a scale range from the macroscopic down to molecular level. One of the pivotal aspects of hydrogels is the structure and the dynamics at the submicroscopic and nanoscopic scale. In this context, the concept of *mesh size* plays a pivotal role.

The average mesh size of a gels is a structural parameter characteristic of the hydrogel "porosity", the controlling role of which on diffusant diffusion in macromolecular systems and gels has been a topic of interest[12,66,67], in the last 30 years. A gel's mesh size is essentially what Experiment 2 (section 7, page 97) attempted to simulate through the use of void size and hole size.

However, a reliable prediction of the mobility dependence on the matrix concentration, diffusant size and shape, and their interactions is still missing, as is a deep inquiry about the effect of different temperatures and solvencies on such factors.

In this context, among the differences between polymer solutions and gel, it has notably been reported by Seiffert et al.[68] how mobility of rigid diffusants can be dramatically hindered by permanent crosslinking of a solution, as opposed to same-size linear polymer diffusants diffusing by reptation. Also, the presence of permanent inhomogeneities in crosslinked gels has been experimentally deduced with different techniques[69,70].

An integrated approach would require a static and dynamic study of the composite system at different length scales. Gianneli et al. have recently[30] developed a dynamic light scattering technique (μ-PCS) to estimate the mesh size of PNIPAAm gels anchored

on a glass substrate and swollen in a good solvent (ethanol) through the cooperative diffusion coefficient of the permanent network. Depending on the crosslinking density, the average mesh size of such ethanol-swollen gels (alcogels) varies between 2 to 5 nm. Expectedly, these alcogels allow the penetration and diffusion of non-matrix-interacting molecular tracers (Rhodamine 6G, hydrodynamic radius: $R_H = 0.8\,\text{nm}$) as revealed by fluorescence correlation spectroscopy.

Since a large use of hydrogels is being made in biological environments, however, deeper knowledge of the system's behavior in water is needed. In addition to the basis of a structure theory, the systematic engineering of hydrogels for sensing applications also has the potential to hugely benefit from a systematic understanding of the structure, dynamics and duration limits of the gels themselves. To this end, the present fluorescence correlation spectroscopy (FCS) study revolves around PNIPAAm anchored hydrogels, with multiple goals. These include primarily probing the gels' behavior in aqueous environments at different temperatures, encompassing the thermal-dependence, and providing a more coherent picture of the structure-dynamics relationship at the nanometer scale. Hence, the present work focus on the analysis of the swelling ratio R_S of and tracer diffusion in PNIPAAm hydrogels under different physicochemical conditions. These two quantities, which are obtained from the same experimental technique under equivalent conditions, represent space averaged quantities in the micrometer and submicrometer scales.

Finally, as touched in section 3 (page 17) the need for the implementation of gels into biosensors requires a gel's functionalization to still be working under the collapsing mechanism. This, together with the aforementioned aspects, was also addressed in the described Experiment.

8.2. Sample preparation

Hydrogels were observed anchored on glass slides described in section 5.2 (page 34). Since they were immobilized at the base in the XY plane, their swelling was assumed to be, in a first approximation, one-dimensional.

8.2.1. Substrate treating

In order for the gels to be anchored, the glass slides needed to be treated. First, the slides were cleaned according to the following protocol:

    i.   Pre-rinsing in ethanol

    ii.   15 minutes sonic bath in Hellmanex solution, 2% in MilliQ water

    iii.   10 rinsing cycles in MilliQ water

    iv.   15 minutes sonic bath in MilliQ water

    v.   10 rinsing cycles in MilliQ water

    vi.   15 minutes sonic bath in ethanol

Following cleaning, the slides were treated with the BP-silane solution (5 mg/ml) described in section 5.3.1.2 (page 36) according to the following protocol:

    i.   Overnight self-assembly at room temperature in inert Argon atmosphere

    ii.   60 minutes cooking at 50 ºC in a vacuum

    iii.   Rinsing of BP-silane excess via ethanol and subsequent drying via air gun

The hybrid method described above was developed in order to counteract a supposed deteriorating effect in the BP-silane stock solution. The deteriorating effect was later found to be nonexistent. However, the new method did allow us to shorten the previously standard waiting time for slides treatment from 2-3 days to overnight, and therefore was adopted as new standard.

8.2.2. Gel spincoating and drying

Following slides treatment, a 10% mass/mass, PNIPAAm-in-ethanol solution was spincoated onto the substrates. The solution had previously been filtered clean of impurities via a Millipore Millex-FG, hydrophobic PTFE filter, having a pore size of 0.2 µm. It was also my care to discard the first solution droplets to pass through the filter, in order to dispose of possible, if improbable, manufacture residuals in the filter's pores.

The gel was spincoated onto the substrates for 1 minute. In order to obtain a good resolution during the experiments, which translates into a high gel thickness, the spincoating was purposefully performed at low speeds, 250 RPM being the norm. Although the drawback of this, a rippled dry surface, requires multiple-points averages in order to define a dry thickness, the thickness in the swollen state has proved nonetheless uniform.

Following the spincoating, gels were dried overnight in a vacuum oven at 50 ºC.

8.2.3. Gel crosslinking and gel-substrate grafting

Chain-chain crosslinking and chain-glass grafting were achieved simultaneously through UV irradiation. The spincoated and dried samples were irradiated with UV light at a wavelength λ = 365 nm via a Stratalinker 2400 model from Stratagene. Irradiation causes the benzophenone to form a diradical, which inserts into a neighboring available, non-aromatic C-H bond (which abound on the employed PNIPAAm chains) thus providing the required permanent crosslink points. Since irradiation is performed on PNIPAAm chains and glass slides both presenting benzophenone groups, we have the simultaneous creation of the hydrogel macromolecule and its permanent grafting to the functionalized glass.

The crosslinking equipment was calibrated to provide a dose of 6.28 $J \cdot cm^{-2}$ during one hour irradiation. The crosslinking apparatus was equipped with an internal sensor allowing for precise dosage of irradiation in terms of $J \cdot cm^{-2}$. The actual relevant parameter for the crosslinking degree is the UV dose. However, for simplicity, the gels will be referred to in the following treatment with the nominal equivalent crosslinking time in minutes, where 6.28 $J \cdot cm^{-2}$ is equivalent to 60 mins irradiation time.

The applied UV irradiation dose ranges from 1.05 to 12.56 J·cm^{-2} for non-annealed gels, corresponding to 10-120 minutes crosslinking duration.

The applied UV irradiation dose for the annealed specimen, which experience enhanced stability at low crosslinking degree and will be detailed further in this Experiment's treatment, ranges from 0.52 to 12.56 J·cm^{-2} (5-120 minutes crosslinking).

8.2.4. Pre-FCS gel characterization and rinsing

Prior to FCS characterization, crosslinked gels needed to be rinsed of uncrosslinked chains. As the degree of crosslinking plays a major role in the actual number of crosslinked chains, rinsing a newly prepared gel of its uncrosslinked fraction was essential in order to avoid having to deal with what, in absence of uncrosslinked chain removal, would have amounted to a mixture of permanently crosslinked gel and free chain solution.

    i.   Dry thickness measurement via step profiler

    ii.   Gel rinsing via subsequent swelling in 1 ml ethanol (full capacity of Attofluor chamber) followed by 1 minute rest, then removal of ethanol via same pipette. 15 repetitions

    iii.   Drying

    iv.   Dry thickness measurement via profiler

    v.   Dry thickness measurement via Z-scan

8.2.5. Gel annealing

As the present Experiment has a pivotal point in the study of the gels' inhomogeneities, an additional step was added to the preparation of a number of samples, in order to try and render said gels' structure more homogeneous. To this end, following the drying described in section 8.2.2 but prior to being crosslinked, said samples were annealed for 60 mins at 170 ℃ in a vacuum, with the aim of relieving the PNIPAAm

chains of possible residual mechanical stress due to the spincoating, thus rendering the nanometric structure more homogeneous.

Following the 60 mins annealing, the temperature was slowly brought back to room temperature (in order to not reintroduce additional stress), then the samples were crosslinked as per section 8.2.3.

8.2.6. Gel functionalization

The latter stages of the Experiment treated in this section revolved on diffusion in antibody-functionalized gels. To this end, functionalization was performed according to the following protocol, based on the method developed in house by Aulasevich et al.[71] and currently employed by Huang et al.[72]:

    i.   Hydrogel carboxylic group activation via swelling for 90 minutes in solution of TFPS (25 mg/ml) and EDC (75 mg/ml) in MilliQ water, in order to convert its carboxylic moieties into terminal TFPS ester moieties

    ii.   3 rinsing cycles of Acetate buffer, pH 4.0, in order to remove residual TFPS and EDC

    iii.   2 hours incubation of 90 μg/ml anti-GFP in Acetate buffer, pH 4.0

    iv.   30 minutes swelling in 1 M solution of ETA in MilliQ water, in order to block unreacted TFPS ester groups

    v.   15 rinsing cycles via PBS

8.3. Experimental

The FCS setup employed was the one described in section 5.1 (page 33) for Experiment 3. Attofluor chambers were employed for the measurements. Additionally, a thermal stage was mounted above the objective, upon which the Attofluor chambers were placed, so as to allow for temperature control in the samples.

Unless otherwise specified, all samples were measured at 16.3 ℃ in order to observe the gels in the well-swollen state, i.e. well below the LCST. Also, unless otherwise specified, all diffusion as described in this Experiment's treatment was performed with Alexa 647.

The employed thermal stage was a PE100-I model from Linkam, regulated via a PE94 controller and providing the desired temperature via a Peltier element. However, since the temperature in the sample did not correspond to the stage temperature, a Keithley thermocouple was used to probe the sample's temperature and control thermal equilibrium. In this context, a series of steel thoroids were especially manufactured and placed in the center on the chamber, so as to restrict to a minimum the portion of the samples not in direct contact with metal.

For this Experiment, the FCS setup was employed to measure two properties of the gels through two different techniques:

Property: swelling ratio (R_S). The hydrogel profile was obtained from the so-called Z-scan, which involves record of fluorescence intensity of the labeled tracer at various points in the Z direction, normal to the film / the glass substrate. In the absence of specific interactions between the tracer and the PNIPAAm segments, the intensity assumes its maximum in the free solvent and decreases due to excluded mass effect in the hydrogel matrix. The hydrogel's thickness is estimated with the resolution determined by the $2z_0$ (2 μm circa) from plotting the intensity versus the distance from the glass substrate. Typical examples of Z-scan gel profiles are reported in Fig. 55 (page 155). The swollen thickness was then normalized to the (post-rinsing) dry thickness of the gel, which yields the swelling ratio, R_S .

Property: tracer diffusion slowdown. Or rather, the inverse slowdown, i.e. the reduced diffusion coefficient, D/D_0 , where D is the diffusion coefficient inside the gel and D_0 the diffusion coefficient in the free solution. For each sample, the intensity correlation function $G(t)$ was recorded in the solution both above and inside the hydrogel. For gels displaying discontinuous morphology along the Z direction, such as density gradients, $G(t)$ could be recorded at different distances from the substrate inside the hydrogel. The present hydrogels, however, revealed a homogeneous structure at least within the

resolution range and a gradient-free behavior up to 10 μm above the glass substrate. For each Z position inside and outside the gel (in free solution), $G(t)$ was recorded at least at three different positions in the XY plane, at distances ranging from 200 to 800 μm apart, from which the averaged value of the diffusion coefficient was obtained. Such averaging process was applied to both the swollen and collapsed state of the PNIPAAm gels, as detailed further in this Experiment's treatment. Similarly, R_S was probed in the same XY spots, and averaged for the dry, swollen and collapsed states.

$I(t)$ was typically recorded from 2.5 min, for diffusion in pure solvent with strong fluorescence, to 10 minutes in the case of diffusion in dense gels where few particles could penetrate. These total accumulation times were subdivided in 30-seconds intervals in order to enable removal of occasionally erroneous signals due to aggregates. Prior to actual measurements, calibration was performed on both excitation channel, employing Cy5 for channel 1 and Rh6G for channel 2, as detailed in section 7.2 (page 98). Both dyes were diffused in MilliQ at the same time in a dedicated Attofluor chamber, and their diffusion times measured three times for each dye/channel while shutting the other channel close. Calibration was performed for each measuring temperature at the same temperature.

All $G(t)$ curves were fitted excluding the data points up to ~ 10 μs, beyond the triplet effect time range, thus allowing for an exclusion of the triplet contribution parameters from the fit.

Prior to the FCS experiment, as mentioned, all samples were rinsed 15 times *in situ* by swelling in ethanol and removal of ethanol solution, in order to remove uncrosslinked chains. The measurements in the swollen state were performed before and after thermal collapse, to examine possible squeezing of uncrosslinked chains out of the gel. However, this last passage proved superfluous, as the revealed differences were negligible and hence marks ethanol rinsing adequate for gel cleaning.

Alexa 647 has no specific interactions with PNIPAAm, as revealed by its free Fickian diffusion in both water and ethanol PNIPAAm solutions. It is therefore chosen for the present study as a neutral reporter of the role important variables play on the macroscopic

and nanoscopic structure and mobility of PNIPAAm hydrogel layers grafted on glass substrates. The swelling ratio R_S is measured via the Z-scan with a spatial resolution of the order of $2z_0 \sim 2\mu m$. The tracer diffusion D of the molecular dye is probed within a volume with a XY diameter $2x_0$ (~ 300 nm). The two quantities (R_S, D/D_0) should therefore yield complementary information on the structure and dynamics in the micron and submicron range.

8.3.1.   Non-annealed gels
8.3.1.1.   Variable: crosslink density

We first examined non-annealed PNIPAAm gels, swollen in MilliQ water under good solvency at 16.3 ºC, well below the LCST. Fig. 38a shows normalized experimental correlation functions for two hydrogels with different crosslinking density prepared for 10 min and 120 min UV exposure (corresponding to 1.05 to 12.56 J·cm^{-2} irradiation doses). In all the examined cases, Alexa 647 diffusion exhibits single component Fickian diffusion, with (4.21) with $n = 1$ representing very well (solid lines in Fig. 38a) the experimental $G(t)$. The anticipated linear time dependence, $\langle \Delta r^2(t) \rangle \propto t$ is revealed as seen in the inset to Fig. 38a. Also seen in the same Figure is how D expectedly slows down with crosslinking density and, hence, polymer concentration in the gel. The swelling ratio, R_S, decreases with crosslinking density as depicted in Fig. 38b together with data for annealed samples, which will be discussed further in this treatment concerning spatial inhomogeneities in the hydrogels.

As expected, the higher the crosslinking is, the weaker R_S is, and the tracer diffusivity also decreases with increasing crosslink density.

Addressing now R_S, behavioral differences in swelling are known to exist between unanchored gels (3D swelling) and their anchored counterparts (1D swelling). The anchoring restricts movement and swelling at the hydrogel-substrate interface and allows network expansion only away from the surface in a highly anisotropic fashion[10, 73]. A direct consequence of this surface confinement in the hydrogel layer is a reduced swelling

126

compared to the unrestricted 3D hydrogel by a factor of around 5 to $10^{[73b, 74]}$. For an unanchored gel, the volumetric swelling is given by [73b],

$$V_S \propto \lambda_C^{-\frac{3}{5}} = N_C^{\frac{3}{5}} \tag{8.1}$$

where, $\lambda_C = N_C^{-1}$ with N_C being the effective number of chain segments between crosslink points. On the other hand, for a linear swelling behavior of the same anchored gels,

$$R_S \propto \lambda_C^{-\frac{1}{3}} = N_C^{\frac{1}{3}} \tag{8.2}$$

Analogously, the two types of network display different cooperative diffusion coefficients as revealed by recent micro-photon correlation spectroscopy (μ-PCS) experiments[30], and the crosslinking of anchored PNIPAAm gel layers apparently reduces their mesh size much stronger than anticipated for transient networks in good solvents. In this context, differences between 3D and 1D systems have also been observed in permanent gels[73b].

In Fig. 38b, the supported PNIPAAm films containing the same concentration of crosslinking agents were exposed to different energy dose, ν, in order to vary the crosslinking density, λ_C. A direct relationship between λ_C and ν is, *a priori*, not known, and therefore nor can assumptions like $\nu \propto \lambda_C$ be taken for granted. In order to estimate λ_C, we therefore must rely on phenomenological dependences like $R_S \propto \nu^a$ (Fig. 38b) in the low ν range and the predicted scaling behavior as per (8.2). Fig. 38b also reports data for gels annealed previous to crosslinking.

Data points for R_S at low energy dose, ν, conform to the power law described above, with exponent $a = -0.61 \pm 0.04$ and -1.26 $\pm$ 0.01 respectively for the non-annealed and annealed samples, where the fitting (red and orange lines in Fig. 38b) was carried forward only on those data points in which the power law was applicable: 5 to 15 mins crosslinking for annealed gels, and 10 to 30 mins crosslinking for non-annealed gels.

At irradiation times / energy doses above the described ranges, UV irradiation appears to be less effective resulting in a weaker crosslinking density than predicted by the power law. This is easily attributed to the consumption of the BP groups already being converted into crosslink points at lower ν.

Interestingly enough, BP groups conversion saturation appears to be reached sooner in annealed gels, an aspect which will be addressed further in the treatment.
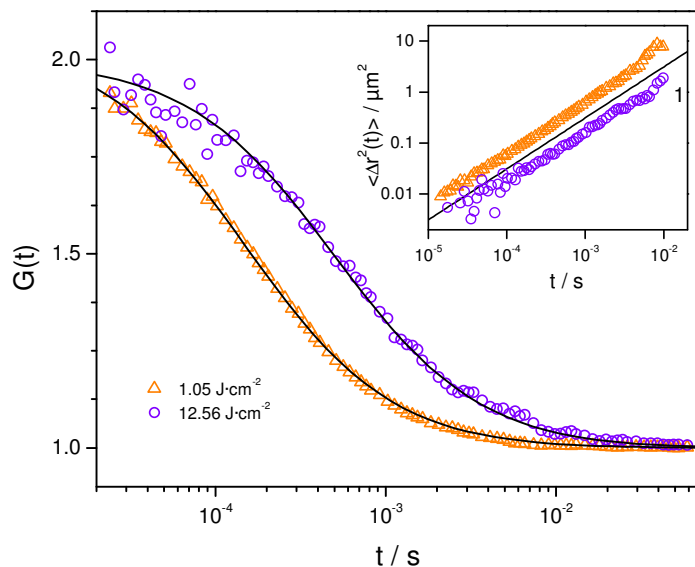
a)
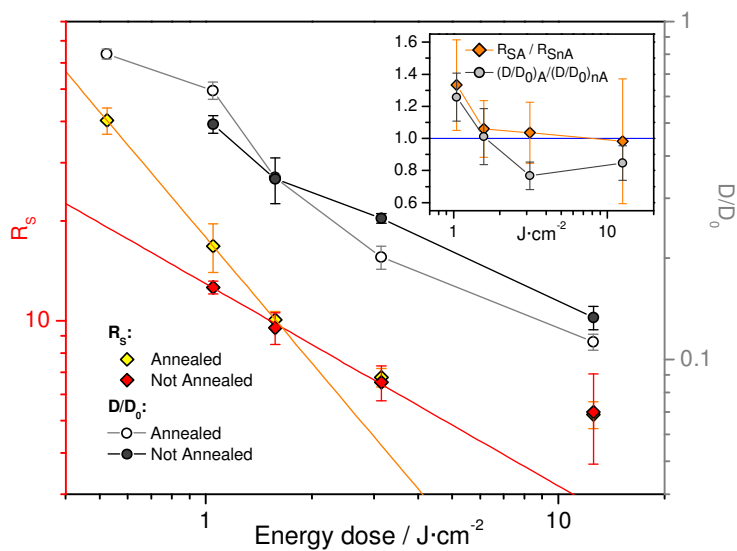
b)

Fig. 38. a) Normalized $G(t)$ of Alexa 647 diffusing in a low- and a highly crosslinked PNIPAAm gel swollen in MilliQ water at 16.3 °C. Inset: The mean square displacement conforms to single Fickian diffusion (indicated by the slope 1 of the solid line). b) Swelling ratio R_S and normalized diffusion D/D_0 of Alexa 647 in the PNIPAAm hydrogels (annealed and non-annealed) plotted against energy dose in the crosslinking procedure. For R_S, the solid lines denote

the power-law dependence on the energy dose v with exponents -0.61 and -1.26 for the non-annealed and annealed variants, respectively. Inset: Ratios of R_S and D/D_0 between annealed and non-annealed samples

Addressing now the diffusion coefficient, D, in Fig. 38b, the decreasing D/D_0 is logically envisioned as either a crowding effect due to increased polymer volume fraction, ϕ, and /or reduced porosity of the hydrogel due to the decrease of the gel mesh size, ξ, as the crosslinking degree increases.

An attempt on modeling D/D_0 dependency can be based on a hydrogel-solution comparison. For polymer solutions (transient networks) with $R_H < \xi$, the slowing down of D was recently found[75] to depend only on the concentration, irrespectively of the polymer molecular weight and hence the mesh size, ξ. D/D_0 for said effect can be found, as dependent on the solutions' ϕ, as the dashed line in Fig. 39. As depicted, the D/D_0 values fall on a single master curve[75] for the same molecular tracer in transient polymer networks, and D/D_0 can be parametrized[75] by a stretched exponential, $D/D_0 = \exp(-\alpha\phi^\beta)$, with $\alpha = 9.3$, $\beta = 1.35$.

Coming back to diffusion in the our hydrogels, tracer diffusion data addressed so far are also plotted in Fig. 39 (green diamonds, orange circles, first data point of both brown and purple triangles series) for comparison with the solutions' master curve. In addition to the data extracted by diffusion in gels treated so far, Fig. 39 also reports the rest of data treated further in this treatment, and as such acts as a summary to the rest of data comparison of this sort, which will be detailed in the rest of the treatment.

The gels are indicated by whether they are annealed previous to crosslinking (HGa) or not (HG), with the number following identifying the time equivalent (in minutes) of v.
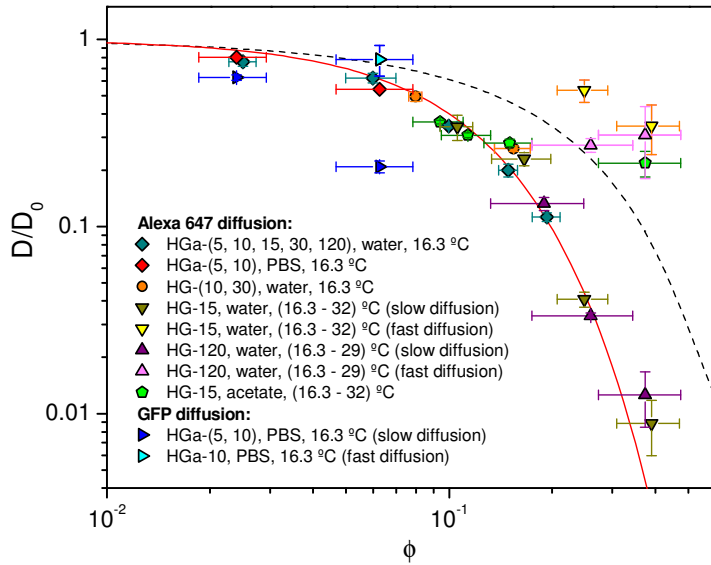
Fig. 39. Master curve for molecular tracer (Alexa 647) diffusion in several PNIPAAm hydrogels as indicated in the plot. The solid and dashed lines are stretched exponential fits (see in the text) of the normalized diffusion of the molecular tracer in the hydrogels and polystyrene homopolymer solutions[75], respectively. D/D_0 is plotted against the polymer volume fraction, ϕ. ϕ is, in its turn, determined by different combinations of crosslinking degree and temperature-induced collapse, as will be detailed in subsequent Figures. Deviations from the master curve are observed for the diffusion of the larger (GFP) probe, the fast Alexa 647 diffusion in PNIPAAm swollen in MilliQ water near the collapse transition (notice the "fast zone" above the master curve) and in PNIPAAm swollen in acetate buffer.

As one can see, in Fig. 39 D/D_0 in gels is plotted as a function of the volume fraction, ϕ. However, the estimation of ϕ for a gel is not trivial, an issue which was addressed as follows.

ϕ for the observed gels was calculated from the measured R_S. Specifically, the relation $\phi = R_S^{-1}$ was employed, the basis for which is the assumed one-dimensional swelling for the anchored gels, together with the fixed value $\phi = 1$ for a dry gel.

Of course, a confirmation of such hypothesis was in order. In order to obtain an independent information on ϕ, waveguide spectroscopy[76,77,78,79] measurements were performed for four samples in MilliQ water at 16.3°C following the same treatment as for the FCS experiment; the samples were low- and highly-crosslinked, both annealed and

130

not annealed, thus representing a reasonable sample population of the samples employed in the FCS measurements. The refractive index profile for these gels is given in Fig. 40.
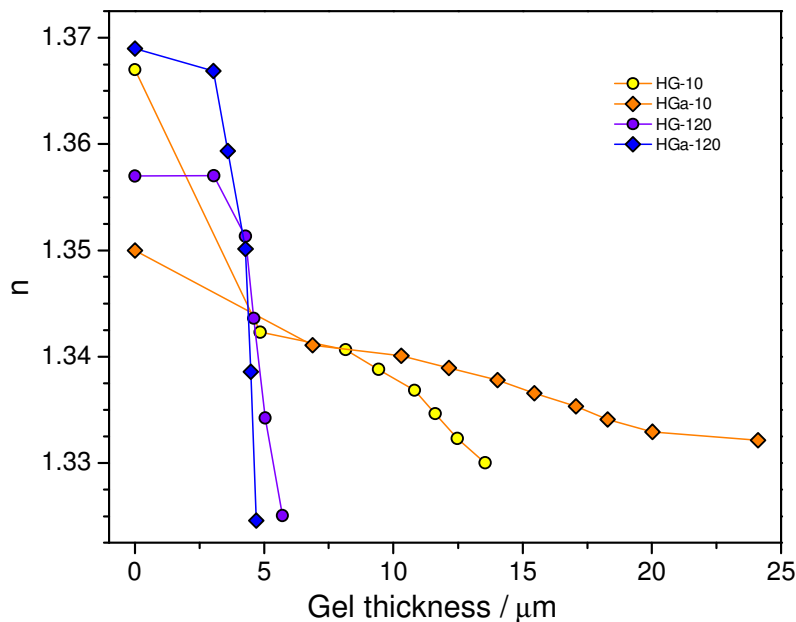

Fig. 40. Refractive index profile of four hydrogels in MilliQ water at 16.3°C. Annealed and non-annealed samples prepared under short and long UV-exposure times as indicated in the plot

Data in Fig. 40 were obtained through the reversed Wentzel-Kramers-Brillouin (rWKB) approximation method[80],[81]. Measurements were conducted in house at the MPIP by Isabel Hopp and fitted by Isabel Hopp and Bernhard Menges. The rWKB method is a well-tested approximation used for planar waveguide gradient index profile analysis[29,29b], the fundamental idea behind which is that different waveguide modes probe different areas of the film because of the different field distributions. In detail, at the position of the electromagnetic field distribution, for which the oscillating and evanescent solutions of the wave equation are identical, the physical refractive index n is equal to the measured effective refractive index for each mode determined by the angular minimum position of the modes.

Based on the refractive index profile a multilayer model is performed, which is the basis for the evaluation of both parts of the complex refractive index.

Once the refractive index profile is obtained, the polymer volume fraction ϕ can be calculated from it. In the effective medium description, it is for a porous system in a fluid of gaseous environment that $\phi = \dfrac{n_s - n_w}{n_d - n_w}$, where n_s is the refractive index of the system plus the environment medium, n_d the refractive index of the system alone, and n_w the refractive index of the environment medium. In the present case, n_s is the refractive index of the hydrogels in the swollen state inclusive of water (obtained from data at Fig. 40 by linear interpolation at height 0, for which actual experimental data do not represent the gel alone due to the technique probing the substrate underneath and the functionalization layer), n_d =1.498 for dry PNIPAAm[29a], and $n_w = 1.332$ for MilliQ water at 16.3 °C. The computed volume fraction based on said waveguide spectroscopy experiments is in very good agreement with the values obtained from R_S in the FCS experiment, as indicated by the values in Table 5.

v (J·cm^{-2})	ϕ, not annealed gels		ϕ, annealed gels	
	From WKB	From FCS	From WKB	From FCS
1.05	0.077	0.079 ± 0.004	0.063	0.06 ± 0.01
12.56	0.151	0.19 ± 0.06	0.210	0.19 ± 0.02

Table 5. PNIPAAm volume fraction in hydrogels as obtained from the WKB and FCS experiments

Thus $\phi = R_S^{-1}$ was assumed correct for all used samples in the FCS experiments, leading to the construction of Fig. 39. As seen in the Figure, for the hydrogels treated until now and in general for the vast majority of hydrogel diffusion data, D/D_0 superimposes on a single curve which can be also represented by a stretched exponential using the same $\beta = 1.35$ value as for the transient polymer networks, but assumes now a clearly larger value $\alpha = 20.5 \pm 0.7$. Still, diffusion of molecular tracers ($R_H < \xi$) in hydrogels observed until now allows for a safe prediction of the molecular tracer diffusion in swollen hydrogels. Fig. 41 reports data points for diffusion in non-

annealed hydrogels probed at 16.3 ºC, and the physical property determining ϕ for the various samples is the crosslinking degree.
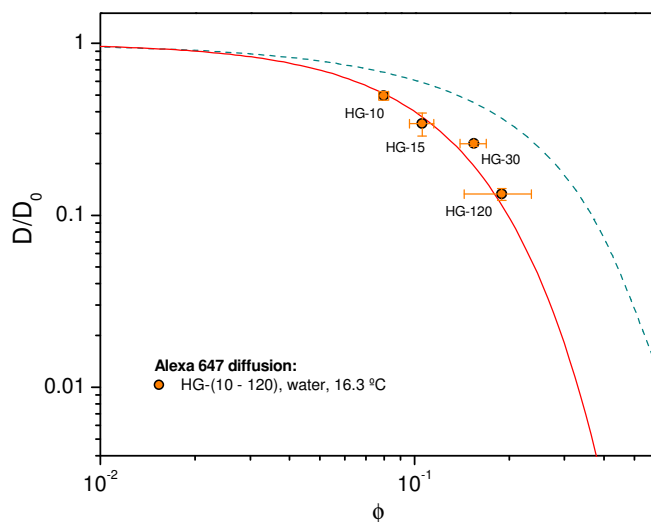

Fig. 41. Master curves at Fig. 39 (continuous lines), with data points for non-annealed gels at Fig. 38. As depicted, increased irradiation time determines ϕ consistent with the master curve

However, inspection of Fig. 39 reveals deviations from the master curve in case of thermally-induced collapse and for the diffusion of larger than Alexa 647 tracers (e.g. GFP). Such effects are addressed below.

8.3.1.2. Variable: temperature

Thermal collapse, the specific property of PNIPAAm hydrogels which was to be addressed as main aim of the project, was then studied in MilliQ water for two specimens, HG-15 and HG-120. Different states of the gels were observed at fixed temperature (thermal equilibrium) below and above 32 ºC. For each, the macroscopic collapse was directly monitored by measuring R_S, while the dynamics were probed by FCS. Fig. 42 shows the experimental $G(t)$ for Alexa 647 diffusion in HG-15 at two temperatures, one far below and the other very close to the hydrogel collapse transition.

As discussed in the preceding section, $G(t)$ at 16.3 °C is very well represented by a single Fickian diffusion (solid line) as seen in the residual plot (Fig. 42a). At 32 °C, $G(t)$ clearly becomes a double decay function which is best represented ($n = 2$ in (4.21), solid line, resulting in the random residual plot, Fig. 42b) by two Fickian processes. The contribution of the fast component accounts to about 50% of the total $G(t)$.
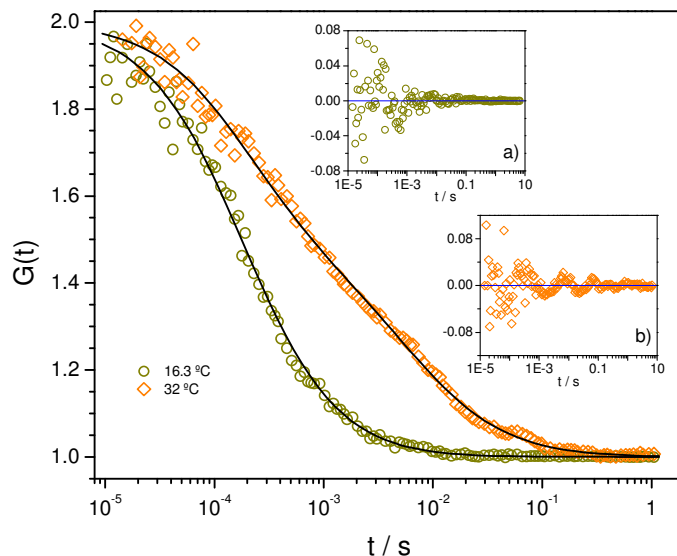

Fig. 42. Normalized FCS functions $G(t)$ for Alexa 647 diffusing in HG-15 at two different temperatures. Solid lines indicate the representation of the $G(t)$ by a single Fickian component ($n = 1$ in (4.21)) at 16.3 °C and two components ($n = 2$) at 32 °C in (4.17). The fit residuals at 16.3 °C and 32 °C are shown in insets a) and b), respectively.

For the HG-15 and HG-120 grafted layers, the swelling ratio and the normalized D/D_0 of Alexa 647 is shown in Fig. 43 as a function of temperature. Note that two Fickian processes are required above 29 °C for HG-15 and above 25 °C for HG-120; these two D/D_0 are also plotted against ϕ in Fig. 39, as well as separately in Fig. 44. Above 32 °C for HG-15, and above 29 °C for HG-120, no dye could be detected inside the hydrogels; the fluorescence intensity was at the background noise level, and a featureless $G(t)$ undistinguishable from the baseline was recorded.
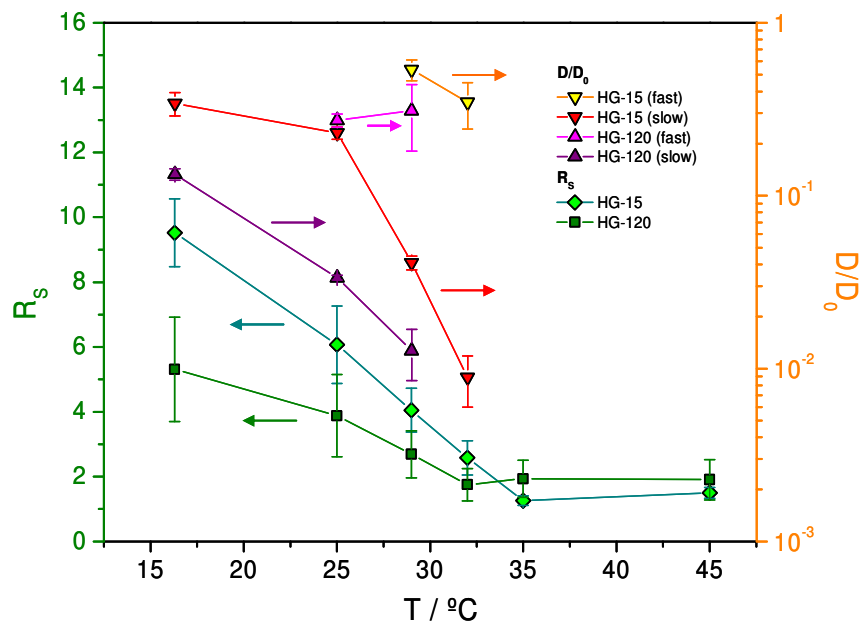
Fig. 43. R_S (left axis) and normalized Alexa 647 diffusion D/D_0 (right axis) as a function of temperature for HG-15 and HG-120 in MilliQ water.

These observations corroborate the notion that both lowly and highly crosslinked PNIPAAm, achieving collapse at higher temperatures, squeezes even molecular diffusants out of the gel, the absence of autocorrelation signal being the proof. In fact, if this weren't the case, two things might happen. In the case of diffusant entrapment, a progressively decreasing average intensity signal would have highlighted immobilized fluorescently molecular diffusants being bleached. On the other hand, absence of bleaching but presence of autocorrelation would have indicated molecular diffusants still moving in water pockets inside the collapsed PNIPAAm structure. Since neither phenomenon is present, we infer therefore that no sufficiently large space is available for Alexa (2.6 nm diameter) in the gel, and that collapse of the PNIPAAm grafted layer causes squeezing out rather than trapping.
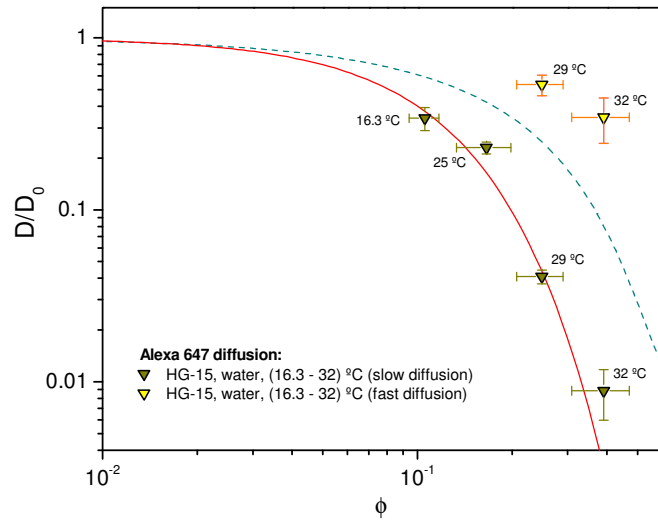
a)
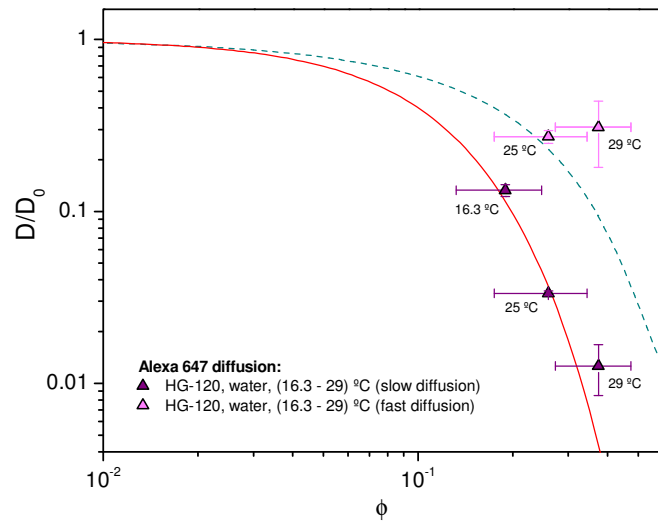
b)

Fig. 44. Master curves at Fig. 39 (continuous lines), with data points for gels at Fig. 43. Increasing temperature determines ϕ consistent with the master curve for the slow diffusion component. The fast diffusion component generates points above the curve, with D/D_0 in the order - when not of higher value - of D/D_0 at 16.3 ºC. a) Data for a 15 minutes crosslinked gel; b) data for a 120 minutes crosslinked gel

Of the two diffusion processes contributing to $G(t)$ of HG 15 at 32°C in Fig. 42, the slow D/D_0 appears to follow the average volume fraction of the hydrogel as obtained from R_S (Fig. 39, Fig. 44). The slow tracer diffusion therefore reflects an effective medium behavior of the gel structure on the submicrometer ($\sim 2x_0$) scale and D/D_0 conforms to the master plot. On the other hand, the fast Alexa 647 diffusion falls above the master curve of D/D_0, in a "fast mobility zone" with D values in the range of $4 \cdot 10^{-7}$ - $8 \cdot 10^{-7}$ cm^{2}s^{-1}. Albeit the origin of this fast process is to be discussed, some hypotheses can be taken out. Among these, a possible relation to cooperative diffusion (D_{coop}) of the network, a process which also appears at high ϕ values, should be excluded. First, it is highly questionable whether D_{coop} can be probed[82] by FCS; second, D_{coop} measured by μ-PCS[30] for PNIPAAm hydrogels is clearly slower (from 3 10^{-7} cm^2/s at 20 °C to 2.10^{-8} cm^2/s at 33 °C).

We can relate this fast process to the formation of structural inhomogeneities within increasing temperature towards the collapse transition. As previously mentioned, as the hydrogel collapses a tendency towards phase separation is countered by permanent structural constraints, and nontrivial structures are formed. An inhomogeneous collapse is therefore to be expected.

The conformity of the slow tracer diffusion to the master curve suggests that the hydrogel undergoes, on average, one-dimensional collapse, increasing its volume fraction and thereby reducing the mobility. Based on Fig. 39 and Fig. 44, however, there should also exist shallower (solvent-rich) regions with 2-3 times lower volume fraction than the average, allowing for fast diffusivity in the pretransition regime. Note that these shallow regions must extend over sizes being comparable with the lateral dimension of the focal volume (~300 nm) in order to impact $G(t)$ but not the swelling ratio measurements. Also, the similarity of D/D_0 values in such shallow regions and in the swollen state (16.3°C) suggests similar local volume fractions, implying that the collapsing phenomenon is essentially local in nature, with the shallow regions remaining essentially unaltered from the swollen state until complete collapse is achieved.

The two drawn trajectories (1 and 2) for the molecular tracer provide a pictorial rational for the slow diffusion sensing an average concentration ϕ (path 1) and the fast diffusion (path 2) that resembles the single tracer diffusion in the homogeneous swollen hydrogel.
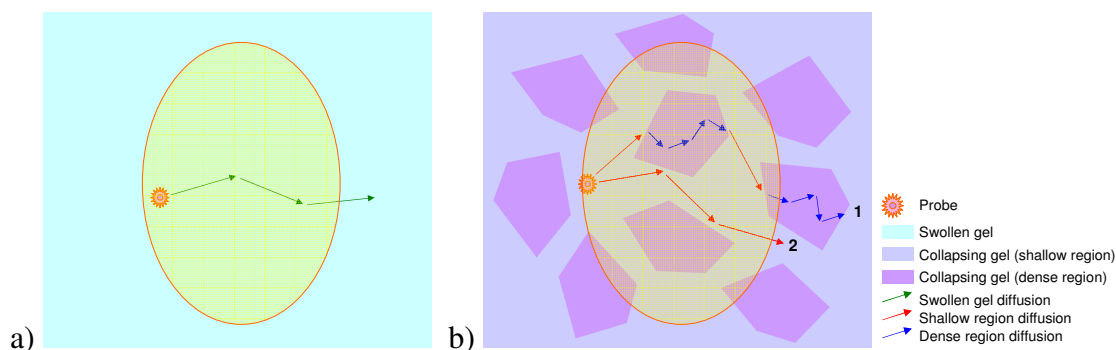

Fig. 45. Diffusion in water-swollen gel. The structure of the swollen gel, perceived by Alexa 647 on the mesoscale. (a) Structure appears uniform justifying the observation of a single diffusion process. (b) A collapsing hydrogel develops structural inhomogeneities which Alexa 647 diffuses through with different times. Diffusion trajectories 1 (reflecting the macroscopic, average R_S behavior) and 2 (fast region diffusion) can rationalize the slow and fast tracer diffusion contributions in the experimental $G(t)$

As a confirmation of the reported findings, the existence of two dynamic features for dissolved molecular species diffusing in the hydrogel films was also observed for the same hydrogel systems via electron paramagnetic resonance spectroscopy by Junk et al.[70], and the presence of inhomogeneities is also known for gel systems through the work of Saalwächter et al.[83,84] and different equipes[85]. In the reported experiment by Junk et al., rotational dynamics of a paramagnetic tracer molecule showed two distinct regions of fast and slow dynamics in the collapsing material, the ratio of which shifted with temperature increase (and concomitant hydrogel collapse) from an excess of the fast to an excess the slow component, which indicates the coexistence of hydrophilic and hydrophobic polymer network regions with temperature dependent volume ratio. The conjecture of spatial inhomogeneities to account for the dynamic heterogeneities in the PNIPAAm hydrogels is further examined by considering subtle interaction effects in the next section.

Quoting previous work[12], an estimation of the mesh size can also be attempted through the relation

$$\tau_D \propto \left(\frac{\xi}{b}\right)^{-\frac{5}{3}}$$

(8.3)

where b is the diffusants' size. In terms of D/D_0, this is equivalent to

$$\frac{D}{D_0} \propto \left(\frac{\xi}{b}\right)^{\frac{5}{3}}$$

(8.4)

Through this, a relative estimation of ξ can be attempted via D/D_0 comparison. Calling $\left(\dfrac{D}{D_0}\right)_F$ and ξ_F the D/D_0 and ξ correspondent to the fast diffusion, and analogously $\left(\dfrac{D}{D_0}\right)_S$ and ξ_S those for the slow/average diffusion, we see that for the same system and diffusant we can arrive, through (8.4), to

$$\frac{\xi_F}{\xi_S} = \left(\frac{\left(D/D_0\right)_F}{\left(D/D_0\right)_S}\right)^{\frac{3}{5}}$$

(8.5)

Similarly, a mesh size ratio, R_ξ, can be estimated between ξ in the low-temperature, well swollen state and during collapse:

$$R_\xi = \left(\frac{\left(D/D_0\right)_T}{\left(D/D_0\right)_{T_{ref}}}\right)^{\frac{3}{5}}$$

(8.6)

where T_{ref} is a reference temperature for the swollen state. Taking $T_{ref} = 16.3\,°C$, R_ξ data can be computed as seen in Fig. 46:
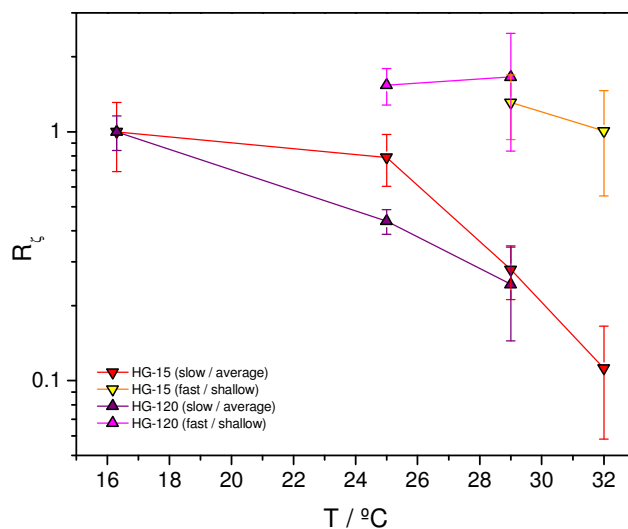

Fig. 46. Mesh size ratio R_ξ between ξ during thermal collapse and ξ at 16.3 °C for slow diffusion (average ξ) and fast diffusion (shallow ξ). Data displayed for both HG-15 and HG-120

The data at Fig. 46, however, should be taken with a grain of salt, since, if previous experiment in ethanol[12] are of any indication, the mesh size in the swollen state should be in the 3 - 5 nm range. Fig. 46 therefore implies mesh sizes going down to 0.3 - 0.5 nm during thermal collapse. For Alexa 647 (diameter 2.6 nm) to be a probe in this system, a substantial mechanical deformation of the meshes is implied. Barring this eventuality, the one-order-of-magnitude decrease of D during collapsing should be attributed to a modified, more complex gel geometry rather than simple, hard-and-fast mesh size decrease. Previous work of colleagues[70] also appears to suggest the complex geometry thesis. In such an optic, the slow/average data points in Fig. 46 refer more to an apparent - *effective*, if one wants - mesh size than an *actual* one.

Other than the considerations above, and keeping to the simple model it is based upon, Fig. 46 is most notable at, giving a quantitative estimate of the mesh size in the shallow

regions: in the order of, and slightly bigger, than that of the swollen state. It is easy to derive from this an image of a moderately elastic gel in the swollen state, with mesh chains outside the dense regions either not collapsing or failing to collapse due to being then stretched to shallow region configuration during thermal collapse.

8.3.1.3. Variable: buffer

As a further step in the hydrogel analysis, behavior in a buffer was addressed, the motivation being the ultimate goal of hydrogels engineering into biosensors. That is, the application of said gels in solvent environments other than pure water.
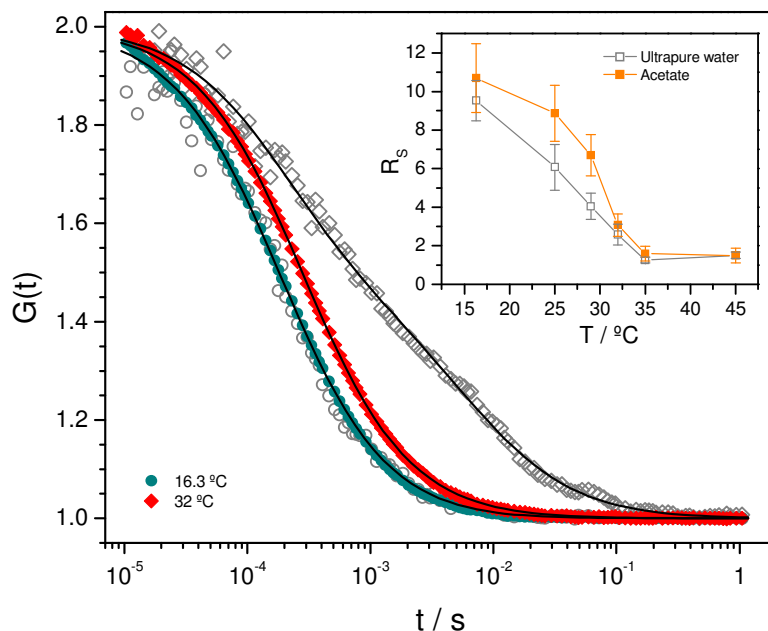
Fig. 47. Normalized $G(t)$ for Alexa 647 diffusing in HG-15 swollen in acetate buffer (solid symbols) and MilliQ water (open symbols) at two temperatures. The solid lines denote the fits. Inset: R_S in the two solvents as a function of temperature

In Fig. 47 we first compare the experimental $G(t)$ of HG-15 in acetate buffer (Biacore, pH 5.0) and MilliQ water (as seen in Fig. 42) at 16.3 °C and 32 °C (notice the double $G(t)$ decay for the hydrogel at 32 °C). While at 16.3 °C the two hydrogels exhibit very similar and single-component $G(t)$, a qualitative disparity appears at higher

temperatures as seen at 32 °C, near the collapse transition. In MilliQ water, $G(t)$ becomes bimodal near the collapse transition temperature and the slow diffusion in HG-15 at 32°C ($D/D_0 = 0.009 \pm 0.003$) is much longer than the single diffusion ($D/D_0 = 0.34 \pm 0.05$) at 16.3 °C while the fast diffusion at 32°C ($D/D_0 = 0.3 \pm 0.1$) is comparable with the latter. In acetate buffer, HG-15 displays only a fast tracer diffusion being marginally slower ($D/D_0 = 0.22 \pm 0.03$) than the single diffusion at 16.3 °C ($D/D_0 = 0.36 \pm 0.01$).

An interpretation of this phenomenon can be given as the formation of structural inhomogeneities being more severe in the acetate buffer, rendering the dense regions inaccessible as inferred by the absence of the slow diffusion. Indeed, while the single process in acetate buffer (green pentagons in Fig. 39, reported alone in Fig. 48) at 16.3°C conforms to the master plot, the single fast process at higher temperature clearly fall in the "fast region" dynamics, like the fast process of the same gel in MilliQ water. Notably a slow process conforming to the master plot of Fig. 39 / Fig. 48 is absent during the hydrogel collapse.
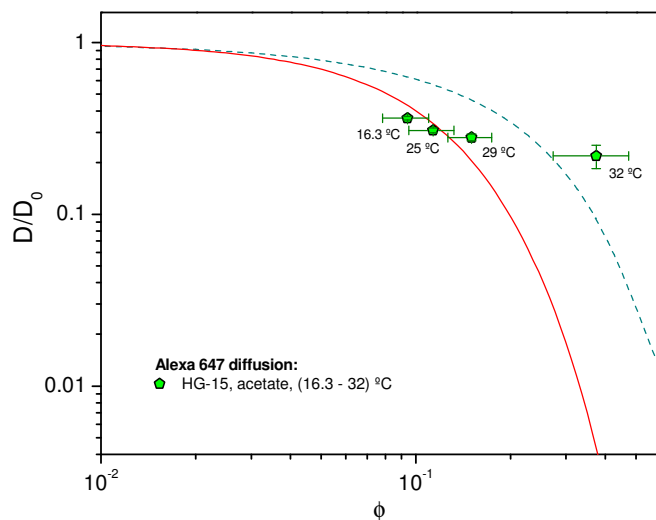

Fig. 48. Master curves at Fig. 39 (continuous lines), with data points for gel referred to in Fig. 47. Contrary to what observed in Fig. 44 for water selling, here a single diffusion process

generates data points exiting the master curve to go into the fast diffusion zone as temperature increases

In contrast to the dynamics, the limited swelling R_S (inset to Fig. 47) in the two solvents near the collapse transition is quite similar, emphasizing the sensitivity of the tracer diffusivity to subtle structural changes.
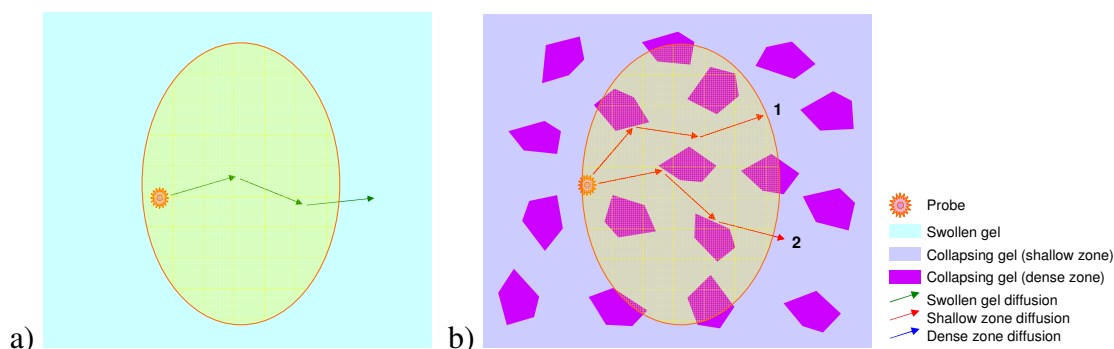

Fig. 49. Diffusion in acetate buffer-swollen gel. The structure of the swollen gel, perceived by Alexa 647 on the mesoscale. (a) Structure appears uniform justifying the observation of a single diffusion process. (b) The structural inhomogeneities of the collapsing gel feature meshes too small for Alexa 647 to diffuse through. Dense region diffusion is absent

In order to rationalize the observed effect, one can try and separate the two main effects a buffer can have on a charged system such as ours. The first effect is charge alteration; the second, an alteration due to salt presence. Of these, charge alteration would suggest a less swollen, more rigid gel in acetate buffer than in water, due to the presence of H^+ ions shielding the previous anionic-based chain-chain repulsion. The result of this would be both a lessened R_S (the chains having a lesser tendency to distantiate) and larger perceived meshes (more neutrally-charged chains possessing a higher tendency to aggregate due to minimization of surface energy, thus resulting in larger meshes). Since neither of these effects is seen in the swollen state, the conclusion is that charge alteration is negligible in this context.

As for a salt-based effect, a non-linear dependency in R_S and inhomogeneity degree was recently reported by Junk et al.[86] as dependent salt concentration in PNIPAAm-based hydrogels. While the degree of inhomogeneity was monotonously increasing with buffer

concentration, a maximum in R_S was achieved for a concentration of 0.01 M, which corresponds to the concentration of acetate buffer as used in the present Experiment.

As was mentioned, in the thermal transition region (32 - 35 °C), R_S assumes very similar values in both solvents.

Indeed, for a PNIPAAm gel swollen in water, it has been found[10,87] that the refractive index n can be plotted as a Boltzmann function of temperature, T:

$$R_S^{-1} = \phi \propto n = Z_2 + \frac{Z_1 - Z_2}{1 + e^{\frac{T-T_0}{\Delta T}}} \tag{8.7}$$

where T_0 describes the function's half-height temperature, and ΔT the function's width and Z_1 and Z_2 are adjustable parameters. (8.7) can represent the experimental swelling ratio as shown for HG-15 in MilliQ water and acetate buffer in Fig. 50. In both solvent systems, T_0 is the same within errors ($T_0 = 305 \pm 2$ K for MilliQ water, $T_0 = 306.0 \pm 0.6$ K for acetate buffer) and so is the width ΔT (2 ± 1 K in water, 1.6 ± 0.3 K in acetate). These data point towards a macroscopic behavior, on the macroscale, substantially analogous between water and acetate swelling.

In order to quantitatively characterize the solvent quality as a function of temperature, an attempt was then done at modeling R_S on a finer scale.

R_S is determined, other than buffer quality as seen in this section, primarily by crosslink density. The latter can, in turn, be linked to the average effective number of repetition units, N_{eff}, between crosslink points; the first, to the effective interaction parameter $\chi_{eff}(\phi,T)$, which represents the solvent quality. Approximating the gel with a perfect phantom network, the equilibrium swelling state is described by[59]

$$\frac{\mu_S}{kT} = 0 = \ln(1-\phi_e) + \phi_e + \phi_e^2\left[\chi_{eff} - (1-\phi_e)\frac{\partial\chi_{eff}}{\partial\phi}\right] + \frac{\phi_0}{N_{eff}}\left(\frac{\phi_0}{\phi_e} + \frac{\phi_e}{2\phi_0}\right) \tag{8.8}$$

where ϕ_0 is the polymer volume fraction in the dry state and ϕ_e the volume fraction in the equilibrium (swollen) state. $\chi_{eff}(\phi,T)$ can be computed as a function of ϕ_e and temperature via:

$$\chi_{eff}(T,\phi) = (A_0 + B_0 T) + (A_1 + B_1 T)\phi + (A_2 + B_2 T)\phi^2 \qquad (8.9)$$

The six (A_i and B_i) parameters in (8.9), which characterize the gel and solvent interaction, have been reported for PNIPAAm gels swollen in water[88].

In order to check the reliability of these parameters, N_{eff} for HG-15 swollen in MilliQ water was computed using (8.8) and (8.9). A temperature independent $N_{eff} = 530 \pm 150$ was obtained in the temperature range 16.3 - 29 ℃ in which the good solvent assumption is tentatively valid. For the high crosslinked HG-120, the obtained $N_{eff} = 150 \pm 30$ is clearly smaller than in the lower crosslinked HG-15. For the two highest temperatures approaching the collapse transition, the computed N_{eff} assumes negative values: as the gel starts to heavily collapse, the phantom network approximation is no longer valid, and the obtained values for N_{eff} are not only not consistent anymore, but physically nonsensical, assuming seemingly random values above and below zero.

A tentative, quasi-quantitative study of $\chi_{eff}(\phi,T)$ in acetate buffer can now be attempted, with the caveat of having its treatment resting on two assumptions: the first, that the described phantom network model be still valid in a charged environment such as the acetate buffer; the second, that we can assume N_{eff} to be a structural invariant under different solvent conditions. Whether the first assumption is debatable, it is the second which requires special caution, since N_{eff} as an *effective* quantity dramatically depends on the chains' conformation and a system presenting an altered geometry, such as we expect the acetate-swollen buffer to be, could make the assumption invalid to begin with.

Assuming N_{eff} to be independent on the solvent, the different swelling behavior of the same gel in acetate buffer (inset to Fig. 47) should be attributed to the change of $\chi_{eff}(\phi,T)$ and/or the collapse transition temperature in this system. The temperature

dependence of R_s (above 32 °C) of HG-15 in the two solvents (inset to Fig. 47) suggests very similar collapse transition temperatures.

To estimate $\chi_{eff}(\phi,T)$ in acetate buffer from (8.9), the knowledge of N_{eff} alone does not suffice, since $\chi_{eff}(\phi,T)$ is dependent on both T and ϕ. Since ϕ itself is dependent on T, it is not possible to attempt a fit of $\chi_{eff}(\phi,T)$ simply as a function of T.
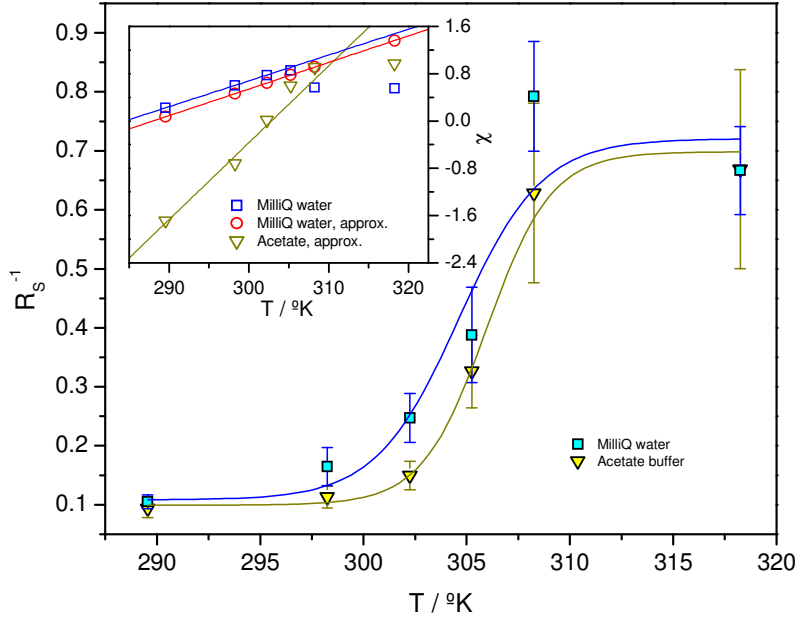
Fig. 50. The inverse swelling ratio R_s^{-1} for HG-15 in MilliQ water and acetate buffer represented (solid lines) by (8.7). Inset: the effective interaction parameter, presented in both the complete ($\chi_{eff}(\phi,T)$) and approximated ("approx.", $\chi_{eff}(T)$) forms for MilliQ water swelling, and in the approximated form for acetate swelling. Continuous lines denote fits of (8.9) and 4 to the experimental data where N_{eff} assumes a meaningful value

In order to reverse-engineer the calculation, and derive $\chi_{eff}(\phi,T)$ from N_{eff}, it was chosen to adopt a linearized version of (8.9), in which the four ϕ-dependent terms were neglected. What was sought after, therefore, was $\chi_{eff}(\phi,T) \approx \chi_{eff}(T)$:

$$\chi_{eff}(T) = A_0 + B_0 T \tag{8.10}$$

This, in turn, also causes $\dfrac{\partial \chi_{eff}}{\partial \phi}$ to vanish in (8.8). A linear fitting following such simplification could now be performed, as it was for the HG-15/water experimental points, restricting the fitting range to the temperatures where the computed N_{eff} values were consistent. This lead to a slight decrease of the interaction parameter: $\chi_{eff}(T) = -12.4 + 0.044 \cdot T$. The value of $\chi_{eff}(T)$ for the HG-15/acetate system, computed in the same manner, is $\chi_{eff}(T) = -39 + 0.13 \cdot T$, and curves are shown in the inset to Fig. 50. Assuming the assumptions made are correct, the values of $\chi_{eff}(T)$ for the HG-15 in the two solvents indicate the a difference in the solvent quality which is observed at the nanometric scale (inset to Fig. 50):below the collapsing temperature range, acetate buffer is a better solvent and swells HG-15 more than MilliQ water does; above, a worse one. Said result is consistent with the behavior theorized in Fig. 49, in which thermal collapse causes collapsing region to collapse in tighter configuration - that is, in this interpretation, to become more hydrophobic upon temperature increase.

8.3.2. Annealed gels

In order to further address the properties of the gels, and their possible tuning for specific biosensing applications, a permanent alteration of the inhomogeneity degree was attempted.

The permanent alteration was carried forward through thermal annealing, as described in section 8.2.5 (page 122), with the aim of relaxing residual mechanical stress in the PNIPAAm chains - and therefore creating a more homogeneous ensemble - previous to crosslinking and the subsequent creation of a permanent structure.

The comparison of the experimental R_S and the normalized D/D_0 for the non-annealed and annealed hydrogels in MilliQ water at 16.3 °C is visualized in Fig. 40b. At low crosslinking densities, the annealed specimen exhibit a larger swelling, while the difference is less felt at high crosslinking. This is in line with what expected from the

addition of the annealing step: more relaxed chains previous to crosslinking, and a minor number of chain bundles, leading to a macroscopically more elastic gel, an effect which is felt more at low crosslinking degrees. Additionally, annealed gels proved themselves stable down to 5 mins crosslinking, while non-annealed ones have a lower stability limit around 10 mins crosslinking.
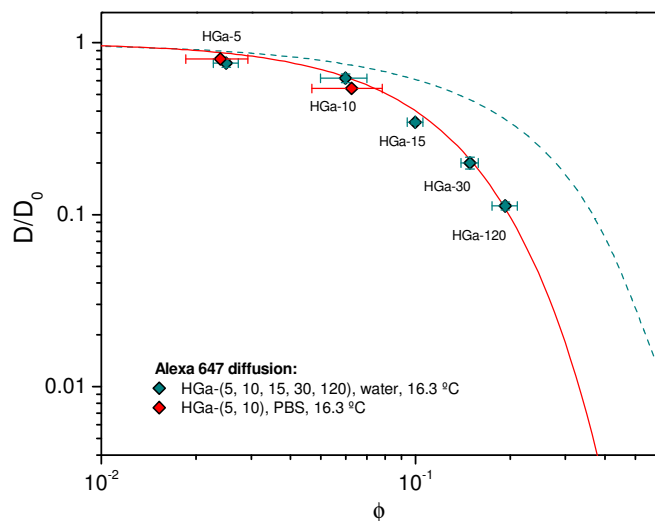

Fig. 51. Master curves at Fig. 39 (continuous lines), with data points for annealed gels. Depicted: the adherence of annealed gel data points to the master curve, and the strikingly close behavior of water-swollen and PBS-swollen gels

If we observe D/D_0 for the same gels, however, we see again larger values below 15 minutes crosslinking (D/D_0 larger for the annealed gel, following R_S) while the tendency is inverted above 15 minutes crosslinking. One can argue that above 15 minutes crosslinking the R_S difference becomes less and less pronounced. In such a regime, when the macroscopic behavior does not dominate any more, the nanometric-scale quantity D/D_0 is determined by a different mechanism, which now plays the major role. What D/D_0 shows at high crosslinking degrees is an average smaller mesh size for the annealed gels. A possible interpretation of this is another aspect of the relaxing effect of the annealing on chains. In such a picture, annealing relaxes denser and shallower (less

dense) zones to a more uniform, average conformation, which includes the relaxation of larger meshes of chains previously present in bundles. Thusly, the picture of a more homogeneous annealed state is painted by the smaller average mesh size accessible by tracers.

Returning to the analysis of gels described performed in section 8.3.1.1 (page 126), we can now compare the different power laws describing R_S for the annealed and non-annealed gels. The fitted value, $a \sim -3/5$ for non-annealed hydrogels leads, together with (8.2), points to a relation $N_c \propto \nu^{-9/5}$ for ν less than about 5 Jcm^{-2} (before the BP conversion saturation). For annealed hydrogels, the experimental value $a \sim -5/4$ suggests $N_c \propto \nu^{-15/4}$. It appears therefore that the UV irradiation is more efficient (lower N_c) for the annealed hydrogels as, prior to the UV crosslinking, the PNIPAAm chains assume conformations and packing closer to the thermodynamic equilibrium. Hence, crosslinking is more efficient, faster, and deviation from power law is achieved at lower ν values than for the non-annealed hydrogels (Fig. 40b).

The higher R_S for the annealed gels at low ν, meaning larger number of chain segments between crosslink points, appears however to be at odds with their larger crosslinking efficiency, implying a lower N_C value.

To solve this apparent contradiction, one should recall that N_C doesn't represent the actual number of monomers between crosslink points on a chain. It instead represents a statistical, effective number of segments between crosslink points. That is, its nature is similar to what we refer to as N_{eff} in the previous section. In the annealing case, the different geometry (or, in other words, the different packing) of the annealed systems is sufficient to explain both a larger R_S and a larger N_C: they both are characteristics of a gel being comprised of more relaxed chains. In this context R_S is the physical macroscopic datum reflecting the higher gel elasticity, and N_C is a statistical parameter, the larger value of which denotes the meshes' higher flexibility in the annealed gels. Both

these characteristics can be envisaged as an expression of less inhomogeneities and chain bundles being present in the annealed gels, thus making gel meshes less rigid.

If observed in the collapsed state, annealed gels reveal further properties. While, as observed for the non-annealed counterparts, no dye could be detected inside the specimens in the collapsed state, something can be inferred by the observation of R_S. In this sense, as reported in Fig. 52, three effects are noticed as induced by the interaction of thermal collapse, annealing, and crosslinking degree.
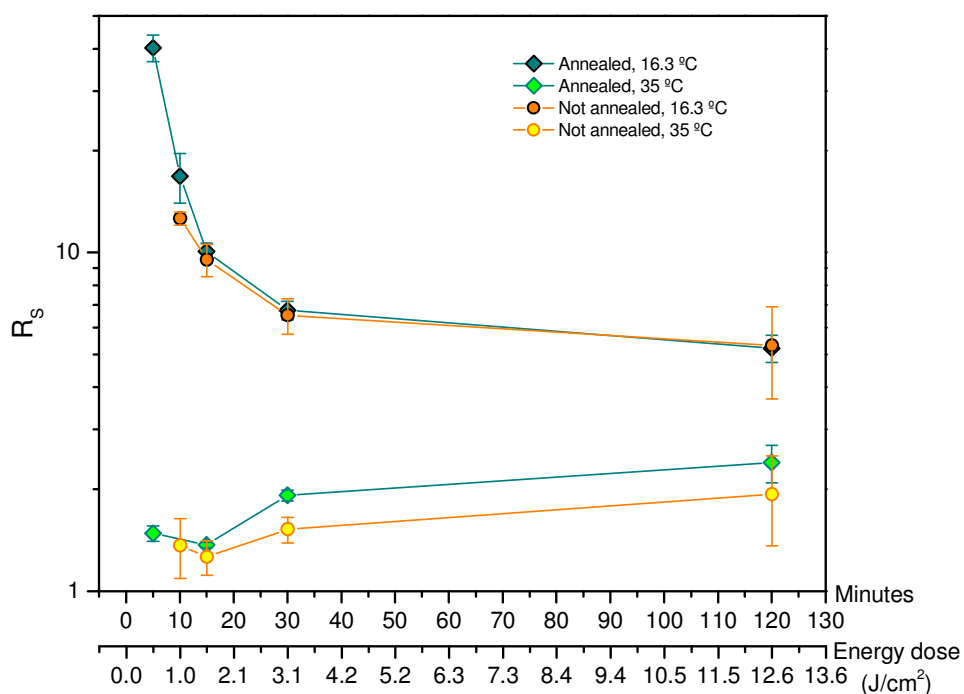
Fig. 52. R_S of annealed and non-annealed gels in MilliQ water versus crosslinking degree, both in the swollen and collapsed state

The first and already reported effect is the decreasing R_S in the swollen state with increasing crosslinking time, shown again here for comparison purposes.

Passing now onto the data points for the collapsed state, we can see a second effect in the form of an inability of the gels, both in the annealed and non-annealed version, to collapse back to its dry thickness ($R_S > 1$). That is, a volume fraction is still occupied by

the solvent (despite the gel being able to squeeze out any trace of diffusants). Again, this is known from previous experiments[29a]. Notice, however, a third effect: an inverse dependency on the crosslinking degree of the collapsed R_S. That is, higher crosslinked gels exhibit higher R_S in the collapsed state than lower crosslinked gels. This can be interpreted as an effect of the permanent structure of crosslinked gels preventing the architecture from fully collapsing, the effect being more marked the heavier the crosslinking and the more complex the permanent structure. In other words, the smaller number of locally closely-packed bundles in annealed gels, in combination with a high number of crosslink points, make for a more stable structure, which is more able to counteract the tendency of the chains to phase separate above LCST.

8.3.2.1.   Variable: protein diffusion and probe size dependence

The following part of the Experiment, focusing on Green Fluorescent Protein (GFP, R_H = 3.1 nm) diffusion, was conducted on annealed gels, due to the increased homogeneity and low-crosslink stability of such specimens (GFP data reported in Fig. 39 as sideways blue triangles, and in Fig. 54). The gels are now swollen in PBS, necessary to prevent denaturation of GFP. Additionally, weakly crosslinked gels were used for this part of the experiment due to the necessity of allowing for large bodies such as GFP to diffuse in. Both swelling ratio and Alexa 647 tracer diffusivity are hardly influenced by the use of PBS over MilliQ water.

The observed very clean, single-component Fickian behavior for GFP diffusion in HGa-5 can be taken as proof of principle of GFP non-interactivity with the gel. This was not trivial in the first place, as structure and subsequent charge distribution on GFP is much more complex and on a molecular dye such as Alexa 647, and therefore localized charges could lead to attractive interactions. However, due to the very smooth nature of the obtained $G(t)$, we can infer attractive interaction to be negligible, and therefore we can treat GFP as a non-interactive probe in the same fashion as Alexa 647.

On the other hand, the experimental $G(t)$ for GFP displays deviations from a single Fickian diffusion for a weakly crosslinked gel (HGa-10) at 16.3 °C. As shown in the inset to Fig. 53, $\langle \Delta r^2(t) \rangle$ appears to have a linear dependency at both short and long times, and an intermediate behavior in between.
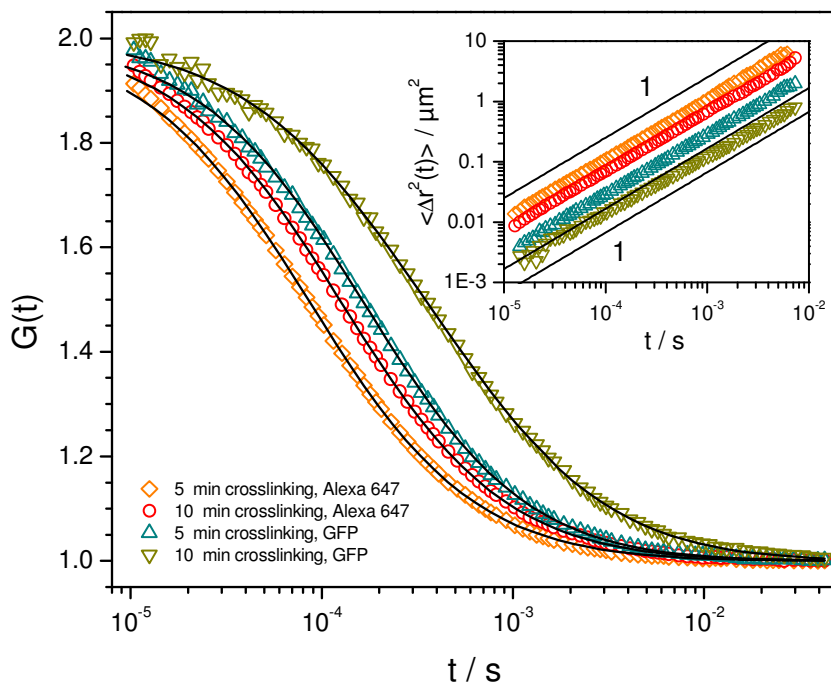
Fig. 53. Comparison of normalized $G(t)$ for Alexa 647 and GFP in two annealed hydrogels gels (HGa-5 and HGa-10) swollen in PBS buffer (pH 7.4) at 16.3 ºC. Single ($n = 1$) and double ($n = 2$) Fickian components in (4.21) were used to represent (solid lines) the fast and (for HGa-10) slow experimental functions, respectively. Inset: Mean square displacement for the two tracers

Two Fickian components were used for an optimal fit of $G(t)$ for GFP diffusion dynamics in this gel. For comparison, the experimental $G(t)$ for Alexa 647, simultaneously recorded in the same hydrogel, not only is markedly faster (as expected) but only presents only a single diffusion process. The two-component representation of $G(t)$ for the GFP tracer diffusion in HGa-10 highlights a situation analogous to what probed by Alexa 647 in the thermally collapsed hydrogel: some of the probes appear to travel through shallower zones. What distinguishes, however, the two cases is the probe

size that now more sensitively discriminates spatial inhomogeneities in these hydrogels. Larger diffusant size enables, therefore, the observation of different scale of inhomogeneities, not completely eliminated by annealing; the 2.6 nm large Alexa 647 cannot perceive such inhomogeneities (it's small enough to perceive mesh size above its own as an average) but the twice larger GFP can.
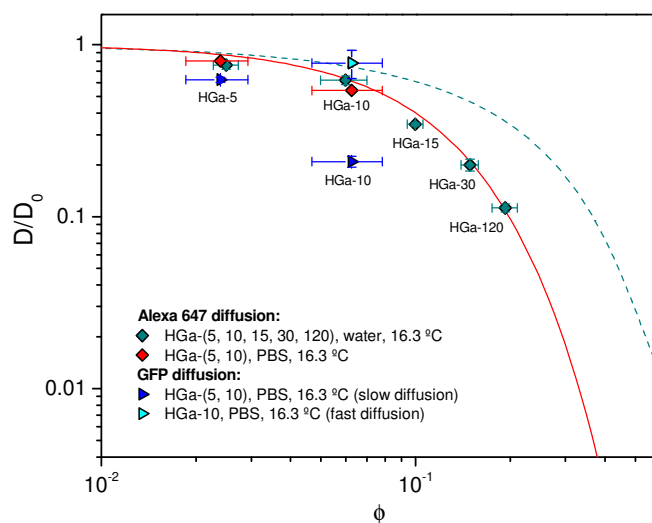
Fig. 54. Addition to GFP diffusion and comparison to data points in Fig. 51. Depicted: the different behavior of data points from GFP diffusion. Concerning the latter, two effects are evidenced: 1) the heightened slowdown due to GFP's size (lower D/D_0 values in the same conditions than for Alexa 647); 2) the presence of diffusion signal splitting in a 10 minutes crosslinked, swollen gel

As mentioned, in order to prevent GFP denaturation, the system had to be investigated as swollen in PBS rather than in MilliQ water. The change of solvent, however, offered the chance to prove a minor theory of mine. It had been a point of discussion whether gel-probes electrostatic repulsion would have resulted in a sensible alteration of the perceived structure. That is, whether electrostatic repulsion from the chains lead probes to perceive a tighter system. PBS in this case is especially indicated, since its stabilized pH of 7.4 allows for a close comparison with MilliQ water. Although MilliQ water has typically a pH around 5, this is due to CO_2 contamination from the atmosphere, and the

concentration of actual H^+ ions is relatively low - the environment is still by and large neutral due to substantial lack of ions. The use of PBS allows for a comparison with an environment whose neutral pH is achieved through high ion concentration. This rationalization finds agreement with what observed for the acetate buffer swelling and collapse (section 8.3.1.3, page 141), where the structure of the gel appears to be influenced by the salt presence, but not by the charge. As a consequence of this, one can see how a change in net charge between water and PBS makes a difference concerning the quantity of dyes entering the gel, but not concerning the structure of the gel itself as perceived by the dyes. This reasoning, of course, also implies that the salt effect of PBS also be negligible. As a result, measured differences in D/D_0 for Alexa 647 diffusing in the same gel swollen in MilliQ water and PBS should be dominated by, and attributed to the interactions between the dye and the chains.

Notably, values for R_S and Alexa 647 D/D_0 in MilliQ water and PBS at the same crosslink density are consistent, if with minor fluctuations, suggesting a comparable perceived structure in the two solvents. For a comparison in this sense, see the very similar values of HGa data point for PBS and MilliQ water diffusion in Fig. 39 and Fig. 54.

More noteworthy is the difference brought by the different solvents to diffusants concentration inside the gels. In Fig. 55, the normalized Z-scan intensity I/I_0 is plotted in linear and logarithmic scale for fluorescents diffusion into a 5 minutes crosslinked, annealed gel, where I is the fluorescence intensity in kHz and I_0 the fluorescence intensity in kHz in the free solvent. As one can see, I/I_0 suffers a drastic dip inside the gel for Alexa 647 diffusion in MilliQ water. In fact, fluorescence drops two orders of magnitude, and single diffusion peaks can be distinguished above the background noise in the recorded $I(t)$.
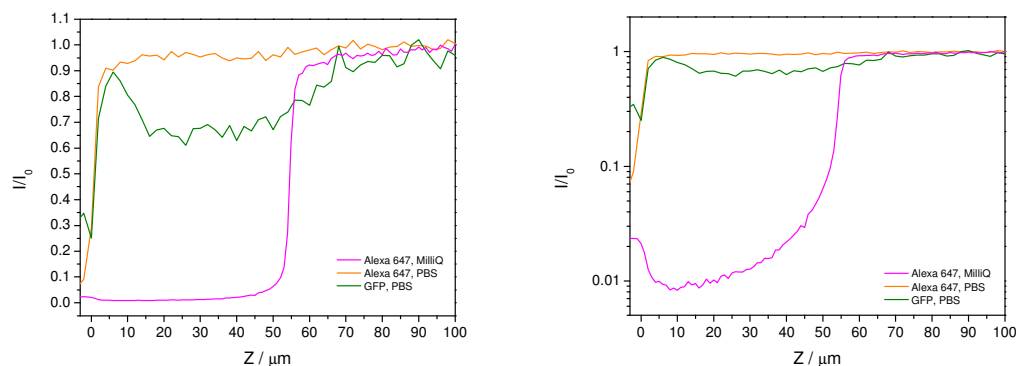
Fig. 55. Comparison of Z-scans obtained from small and large probe diffusion in MilliQ water and PBS buffer. Left: Linear scale. Right: logarithmic scale

We infer therefore that Alexa 647 molecules have a particularly hard time diffusing through the gel. This is not the case of diffusion in PBS, though, where an analogous diffusional behavior is accompanied by such a high in-gel fluorescence as to render the Z-scan virtually useless to establish a profile. Indeed, to establish the profile of the gel is such conditions it is necessary to use the Z-scan from the larger GFP, which still encounters larger difficulties than Alexa 647 to get in due to its size. Clearly, the repulsion preventing the greater part of Alexa 647 from diffusing in the gel in MilliQ water are much lessened in PBS. The high presence of ions in PBS also suggests a possible charge shielding of the otherwise anionic chains, thus facilitating Alexa 647 diffusion. Still, once the molecules manage to enter both gels, the diffusion is very similar.

We infer from this a picture in which the electrostatic repulsion of the system on the diffusants has a sensible effect only when the diffusants are outside and, while inside, act as a zero-sum effect, thus further corroborating the assumptions of our general method, and corroboration the zero-sum effect first mentioned in the Conclusions section to the Experiment 1 treatment (section 6.5, page 96).

8.3.2.2. Variable: antibody functionalization

As a final part in this Experiment, diffusion of GFP was measured in hydrogels functionalized with anti-GFP. The employed antibody is described in section 5.3.4.1 (page 42), while the functionalization protocol is reported in section 8.2.6 (page 123). Following functionalization, the gels were swollen in PBS at 16.3 ºC and GFP was diffused through.

The presence of residual antibodies in solution presented a problem in a first moment, as the coupling of such with our probe GFP would of course alter the parameters of the experiment. In order to get rid of such antibodies, the procedure was changed to rinsing the gel with GFP-in-PBS solution rather than simple PBS. This presented the double advantage of efficiently getting rid of free antibodies (only a 3%, long-time, easily separable signal was routinely detected in $G(t)$ after 10 rinsing cycles) and loading the antibodies with which the gel was functionalized with GFP. Following this, the gels could effectively be studied. All samples used in this section were 5 minutes crosslinked, annealed gels.
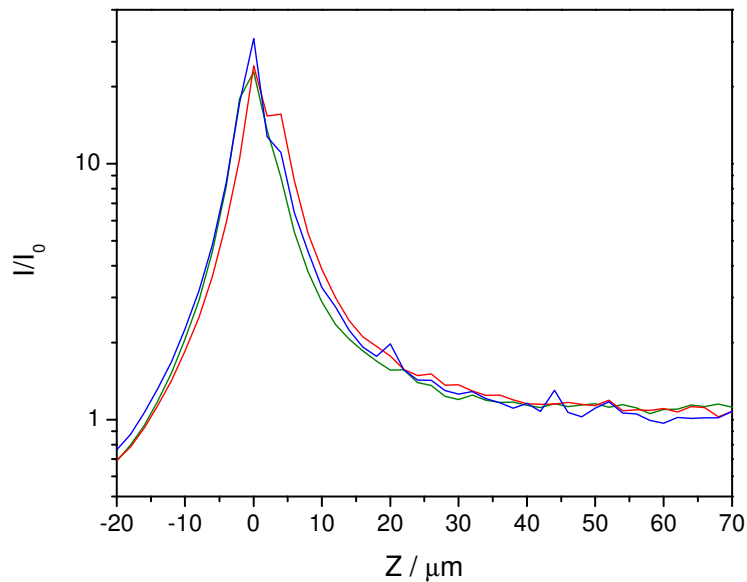

Fig. 56. Z-scan of a single gel in three different XY positions. $I(t)$ is normalized to the $I(t)$ above the gel, I_0

156

Fig. 56 shows both the effectiveness of antibody functionalization and the uniformity of antibody distribution in a gel on the micrometer scale. Contrary to what observed in unfunctionalized gels, the intensity inside the gel is now more than one order of magnitude larger than the intensity outside, which signals GFP being captured by the functionalized matrix. Also, different spots in a gel (hundreds of μm apart) present the same Z-scan intensity profile, thus proving a uniform antibody distribution.

A second confirmation of successful functionalization was the GFP bleaching upon excitation, observed as a continuous decrease towards a baseline in the recorded $I(t)$, signaling immobilized GFP inside the gels. All gels were bleached at the transmission (2%) normally used to investigate diffusion processes, in different spots in the XY plane and at a fixed height of 5 μm above the glass slide

On the minus side, as one can see from the Figure, it is more problematic to establish a functionalized gel's thickness than it was to establish an unfunctionalized one's (compare Fig. 55). A way to do it, although less precise than the sharp Z-scan of unfunctionalized gels, is to record $I(t)$ at different heights in the gel until no bleaching can be recorded. This method, employed by me on the samples, allowed for an estimate of a swollen thickness of 40 μm circa. However, such an evaluation method is less than optimal, as minor bleaching in the low chain density threshold region of a gel can be easily overlooked.

Parallel SPR measurements were lead by Jakub Dostalek and Chun-Jen Huang at the Austrian Institute of Technology (AIT), Vienna, on gels prepared in house at the MPIP following the same preparation method up until crosslinking. The only difference was dry thickness, as SPR measurements benefit from a lesser thickness than optimal in FCS. To this end, the specimen studied in Vienna had an unrinsed dry thickness of 120 ± 1 nm. The last part of said gels's preparation took place at AIT, where they were rinsed, dried, functionalized, and GFP was diffused in them. After rinsing, the Vienna gels exhibited a dry thickness of 46 nm, 38% the unrinsed one, in accord with the 40 ± 2 % measured by me on the thicker, FCS specimen, thus supporting the underlying hypothesis that the different dry thickness plays a secondary role in this comparison.

The gels' n was measured in the dry and swollen state via SPR, the experimental data fitted vi a box model. Swollen-state n was measured both in the unfunctionalized and functionalized, GFP-loaded state, thus allowing to quantify the difference in swelling ratio between the two and the antibody concentration in the functionalized gel.

SPR measurements for such gels revealed $R_S = 28$ for the functionalized gel, less than the $R_S = 40 \pm 4$ for the unfunctionalized variant. When factored with the dry thickness for the equally functionalized, but thicker FCS-geared variant (1.7 $\pm$ 0.1 μm), $R_S = 28$ yielded a swollen thickness of 47 $\pm$ 3 μm. Such value is in good accord with the more approximate evaluation method via bleaching absence, enough to qualify both as a confirmation of each other, and establish itself as a reliable data source for the thickness of functionalized gels of the thick variety as well.

As for the antibody concentration, the surface concentration prior to functionalization, as calculated from n via effective medium theory, was 47.1 ng·mm^{-2}. Surface concentration after functionalization was calculated as 81.3 ng·mm^{-2}, which again by effective medium theory yields a surface concentration of antibodies given by the simple difference, 34.2 ng·mm^{-2}. This, translated into molar concentration, gives a concentration of 165 μM for the antibodies in the functionalized, swollen gel.

Bleaching could be observed in a progressive decrease in $I(t)$, which could be fitted as a double exponential. This is a first indication that the release time of the captured GFP is long enough to safely study the systems as purely bleaching during the observation window.

As seen in Fig. 57, a single exponential fit is insufficient to properly fit the bleaching, and while the double exponential itself presents some residual deviations, it's acceptable.
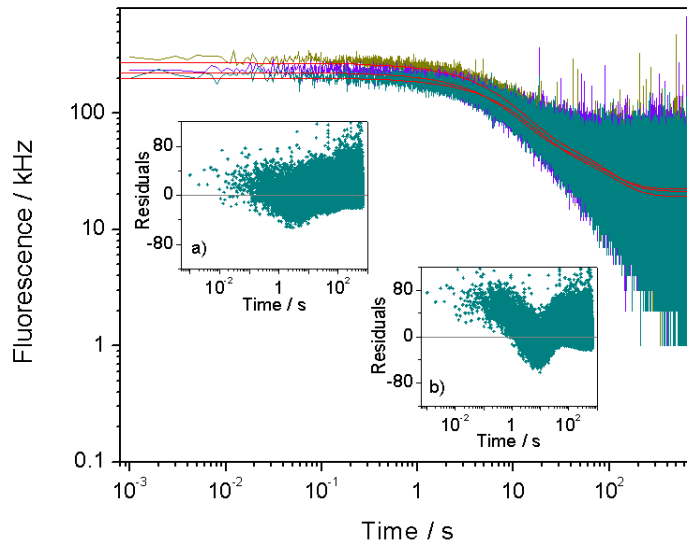
Fig. 57. $I(t)$ for a single sample, probed in different XY spots at constant Z (5 μm). Red lines: fit curves. Insets: fitting residuals for one of the signals: a) double exponential fit; b) single exponential fit
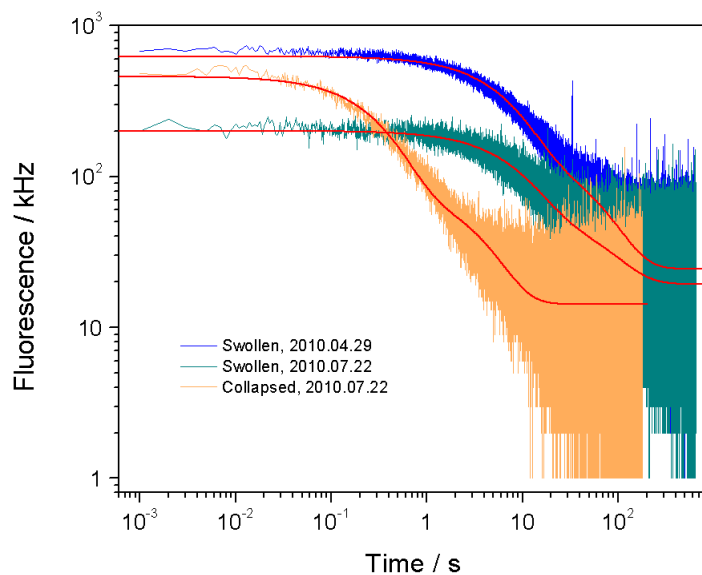
Fig. 58. $I(t)$ for two different samples. Blue and green: two specimens measured in different sessions at 16.3 ℃. Green and orange: single specimen, measured respectively at 16.3 ℃ and 45 ℃ in the same session. Red lines: fit curves

Fig. 57 and Fig. 58 illustrate functionalized sample reproducibility and the effect of collapsing. In Fig. 58, bleaching for different samples is compared in the same swollen

state, and bleaching for the same sample is compared in the swollen and collapsed state (as measured in different XY positions).

As seen in Fig. 58, the starting $I(t)$ for different gels, prepared under the same condition, is less than precisely reproducible. One possible reason for this is the sharpness of the fluorescence peak in the functionalized gels (as can be observed in Fig. 56). Since minor thickness variations occur naturally during the preparation of different specimens, and considered the high R_S of 5 minutes crosslinked gels, it is likely that small the observed difference in starting $I(t)$ be due to said difference in thickness (and therefore in the profile of the Z-scan peak) combined with the fixed Z position taken as measuring height for the bleaching measurements (5 μm).

However, as reported in Table 6 below, the characteristic bleaching times are the same, as are the relative amplitudes of the two exponential components, hinting at a comparable situation at the nanoscale.

	2010.04.29 specimen	2010.07.22 specimen	
	Swollen	Swollen	Collapsed
I(∞) (kHz)	24.6 ± 0.2	21 ± 1	14.23 ± 0.02
I₁ (kHz)	498 ± 17	170 ± 24	378 ± 1
t₁ (s)	6.9 ± 0.3	7.8 ± 0.9	0.331 ± 0.002
I₂ (kHz)	128 ± 5	46 ± 5	69.8 ± 0.6
t₂ (s)	56 ± 2	63 ± 4	3.52 ± 0.03
I₁ + I₂ = I(0) (kHz)	625 ± 44	217 ± 56	448 ± 5
I₁ / I(0)	0.80 ± 0.06	0.8 ± 0.2	0.844 ± 0.009
I₂ / I(0)	0.20 ± 0.01	0.21 ± 0.05	0.156 ± 0.002

Table 6. Bleaching data for the gels reported in Fig. 58

In the Table above, $I(\infty)$ indicates the average $I(t)$ value at long times for bleaching in gels, i.e. the exponential baseline; I_1 and I_2 indicate the average $I(t)$ values for the two exponential components, and t_1 and t_2 their respective decay times. $I_1 + I_2 = I(0)$ indicate the total initial $I(t)$, and $\dfrac{I_1}{I(0)}$ and $\dfrac{I_2}{I(0)}$ the normalized values of I_1 and I_2.

If one observes the swollen and collapsed state on the 7.22 gel, two differences are marked: the first, the radically different bleaching times between the two states; the

second, the higher $I(0)$ in the collapsed state, especially compared with the lower baseline if compared to the swollen state. If one now considers Fig. 57 for comparison, one sees that bleaching in the swollen state for different XY positions in the same gel is consistent in all its features. As a result, I can conclude that the higher $I(0)$ value for the collapsed state is a product of the increased concentration caused by the collapse.

Two data are immediately evident from these results. The first is a very well marked bleaching inside the gel, easily visible in the fluorescence signal, confirming the presence of GFP immobilized in the gel; the second is a still-present autocorrelation signal, which exists both superimposed to the rapidly bleaching-decaying fluorescence baseline, and in the long-time flat region. If fitted, such signal gives comparable data, which show a particularly weak slowdown. Moreover, the diffusion for this process is Fickian, which paints a picture in which the non-captured GFP diffuses devoid of nonspecific interactions.

The picture we can obtain from this is one where a portion of GFP is fixed in place, while the rest diffuse non-interactively in the gel. We infer from this that GFP effectively occupied all antibody sites, leaving a non-interactive system for the rest of GFP to travel through. D/D_0 for GFP diffusing in this system is 0.96 ± 0.03. That is, the only mesh size perceived by GFP is large enough that, statistically, it is almost not perceived at all. This leads us to conclude that either the antibody presence, or another factor in the functionalization process, permanently alters the electrostatic properties of the gel, analogously of how observed during the thermal collapse in Acetate buffer (section 8.3.1.3, page 141). this, coupled with the already mentioned reduced R_S (compared to the unfunctionalized R_S) describes a system substantially more rigid, and possessing a longer-ranged geometry, than the unfunctionalized one: the reduced R_S translates into a reduced elasticity on the micrometer scale; the surprisingly high D/D_0, into a nano- to suprananometric structure which is essentially comprised entirely of chain bundles (the thickness of which easily justifies the structural stiffness) inaccessible to GFP, leaving meshes large enough to cause minimal slowdown.

While, therefore, a functionalized gel is essentially a different system (and thusly cannot be trivially compared on a quantitative level to a non-functionalized one in terms of R_S and D/D_0, the effective functionalization is nevertheless verified, and can be studied in the context of this new system.

A study of the dissociation constant, k_D, of the employed anti-GFP in our gels was attempted, by probing the same spots in the gel at various time spans after bleaching, the target being the observation of full fluorescence recovery, which would signal a complete release of bleached GFP from the anti-GFP and a subsequent refilling of anti-GFP sites with unbleached GFP. However, the desired complete recovery could not be observed within the experimentally available time window, since after six hours circa the water droplet between objective and glass slide evaporated. Since replacement of the water droplet requires the sample to be momentarily dismounted from the setup, and since the reinsertion is performed manually, probing again in the previously-bleached spot after droplet replacement was impossible.

Whether this failed observed recovery was due to the antibodies' high efficiency (low k_D) or to a change in the GFP's structure upon bleaching impeding its release, is not clear.

Following the study in the swollen state, the functionalized specimens were thermally collapsed at 45 °C.

Thermal collapse of the functionalized gel reveals, again, different properties from the unfunctionalized variant, similarly to what observed between the two variant in the swollen state. While R_S of the functionalized variant is analogous to that of the unfunctionalized one, two differences are observed upon analysis of the fluorescence signal: the first is the presence of bleaching, analogously to what observed in the swollen state; the second, the presence of a correlation signal.
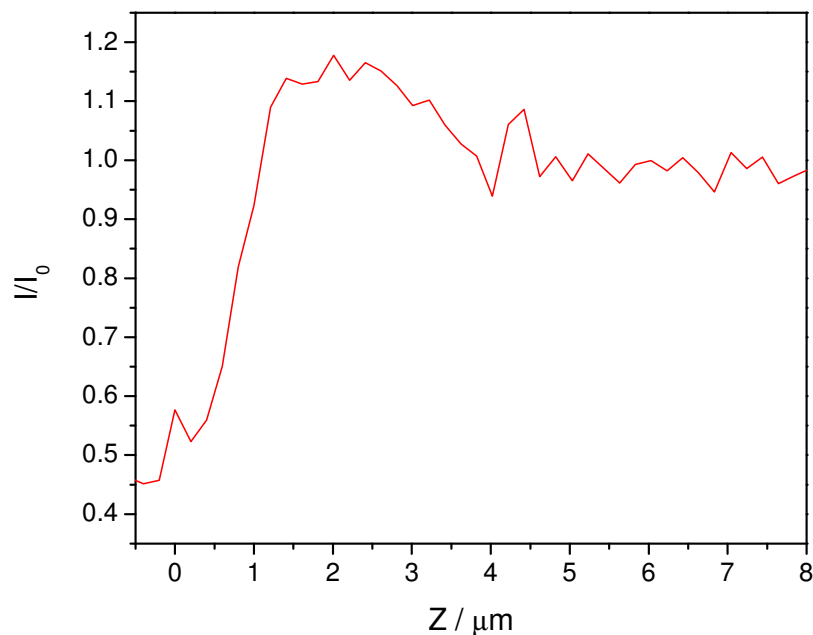
Fig. 59. Normalized z-scan of a functionalized gel, after GFP diffusion at 16.3 ºC and subsequent temperature raise to 45 ºC

As seen in Fig. 59 above, the determination of a collapsed functionalized gel's profile is not trivial, as a bump appears at the gel's edge. The nature of this bump is not certain and, if probed, no bleaching is recorded in this region. This seems to exclude the possibility of skin effects due to the gel collapsing. Also, the diffusion times recorded in the bump are similar to those far above the gel, if a little shorted. This can lead to associate the bump to an abundance of GFP directly above the gel, which is also apparently faster than both GFP in the gel and far above. Furthermore, the presence of analogous bumps can be seen in Z-scans for unfunctionalized, collapsed gels as well. One possible answer to this small paradox can lie in the combination of the presence of uncrosslinked chains in solution, the chains' charge, and the high density of the collapsed gels: since the chains' charge generates chain-chain repulsion, the gels will consequently tend to repel whatever amount of uncrosslinked chains are hovering above them in the solution, thus tending to create a free chain depletion zone above the gel's threshold, which in turn would be seen as the intensity bump in the Z-scans. Said depletion zone would be characterized by a higher average number of fluorescents (the available space

being occupied by less chains) which would also diffuse faster than in the rest of the solution due to the reduced viscosity. The fact that said bump/depletion zone is not observed in the case of swollen gels can be attributed to the comparatively low chain density of the gels in the swollen state, thus leading to a weak chain repulsion. In the collapsed state, on the other hand, repulsion would be much higher.

Getting back to the collapsed functionalized gel features, the first of these highlights the functionalized gel's capability to retain the captured bodies upon forced collapse; the second, the radically different structure compared to the unfunctionalized gel, again analogously to what seen in the swollen state: while all the unfunctionalized specimen displayed a squeezing mechanism capable of expelling the molecular dye Alexa 647, the functionalized gel still featured meshes in the collapsed state large enough to allow for the diffusion of a large body such as GFP. Furthermore, the aforementioned diffusion signal can be quantified by fitting $G(t)$ as obtained after the bleaching of captured GFP. The main observed component displays $D/D_0 = 0.835 \pm 0.001$ and a signal fraction 91.1 %, while the secondary one displays $D/D_0 = 0.0112 \pm 0.0003$ and a signal fraction 8.9 %. This is, again, radically different from the unfunctionalized gels: the observed D/D_0 values are analogous to what previously seen in Alexa 647 diffusion in unfunctionalized gels during thermal collapse, hinting at a structure possessing typical lengths in the same ratio with GFP dimensions as the ratio was with Alexa 647 dimensions in the unfunctionalized, thermally collapsing case. Also, while for the unfunctionalized case the signal fractions of the fast and slow diffusion components were comparable, we notice for the functionalized and collapsed case a large predominance of the fast component. This paints a picture, in accordance to what seen in the swollen state, of the functionalized gel as an entity in which the chains are predominantly, if not exclusively, arranged in bundles, leading to a lowered elasticity compared to the unfunctionalized case (as seen in the reduced swollen R_S) and to a massively large mesh size. The latter is, indeed, large enough that the majority of diffusing GFP hardly perceives it in the swollen state, and still large enough to allow for diffusion in the fully collapsed state.

Inhomogeneities and nontrivial geometry of the system are also evidenced in the collapsed state through the splitting of the signal.

Admittedly, the fast diffusion component in the collapsed gel, as described above, needs to be taken with a grain of salt, since as it evident from Fig. 59, the collapsed state reveals both a very low thickness and a gradient in density. Thusly, it is possible that the observed fast diffusion component is influenced by threshold effects, and therefore one should be caution in assuming such as a sold quantitative value for the collapsed state without further confirmation. Nonetheless, the presence of the slow diffusion component and the observed bleaching still stand as confirmation of both the functionalized gel's peculiar structure and functionalization effectiveness.

8.4. Conclusions

In this Experiment and its treatment, by restricting the experimental conditions to the simplest attainable (non-interactive, monodisperse probes), the complex, multi-variable behavior of notoriously impervious PNIPAAm hydrogels could be studied. Especially important, characteristics of said behavior could be studied in conditions which are both crucial to the knowledge the system's nature, and seldom investigated in literature, due to the charge-interactive properties of the material itself in water-based conditions.

Furthermore, the method applied to the study, FCS, allowed us to observe the system in quasi-ideal conditions, since the experimental requirements for the very working of FCS (small number of probes, system in a solvent) are what was required to intimately, yet non-intrusively probe the system. This is especially crucial for a system such as a hydrogel, since the intimate geometry of it is often determined by *single molecular strands*, therefore rendering more invasive techniques, such as cryo-TEM, of dubious value to begin with.

By achieving this, a twofold objective could be reached: a more profound inquiry into the underlying structure and dynamics of a system which, although currently in use in applied science, is not yet fully understood; and, through the study of functionalized gels

and subsequent bleaching, a practical, field test of the feasibility of the system for biosensing application, which was the inspiring principle of the study in the first place.

Lastly, the technique put in use both probed the system at the nanometric scale, and did so in a statistical fashion (over the span of hundreds of nanometers), therefore giving an estimate of said nanometric-scale behavior on the meso- and macroscale.

9.   Concluding remarks and outlook

Through the use of Fluorescence Correlation Spectroscopy, the presented thesis has focused on three different physical aspects of a single applied science issue - the engineering of hydrogels for the purposes of biosensors development and improvement. This was approached through both direct observation of the system concerned (Experiment 3), and modelization carried on different, but related systems and complementary questions (Experiments 1 and 2, focusing respectively on fine tuning / artifact separation in the measuring technique, and a general predictive model).

In the presented thesis, as is common in science, not all was covered which could be thought of, and therefore many opportunities remain for the experimental threads started therein to be expanded and branched into new investigations.

Concerning Experiment 1, the developed theory could benefit from both independent confirmation of the obtained values for the considered system, and an extension of the experiment itself to include different two-species, or even multiple-species interacting systems. As an example of the latter, the results of Experiment 1 can find a practical application, and even being systematically engineered, in a system where the fluorescent signal is produced not from a molecular dye, but rather from a dye-tagged body A, interacting with an untagged body B. More concretely: the treatment of Experiment 1 already provides a phenomenological interaction model and a means to include positively interacting probes into diffusion experiments such as Experiments 2 and 3; furthermore, the method can also be applied to systems where the interaction between A and B has a more direct real-life relevance. One possible application can be the quantification of especially low-efficiency body-antibody interactions.

More interestingly, one could systematically apply the results of the Experiment 1 treatment to the measurement of charges of nanometer scaled objects, provided that the objects to be evaluated are fluorescently tagged and that they are diffused in solution together with reference particles of known charge - as a very easy example, metal nanospheres. By using reference particles of different charge and size, thus providing stronger/weaker interactions, the experimenter could evaluate the investigated bodies'

charge from the hybrid diffusion coefficient and signal fraction, provided that the model be expanded to include the explicit dependency between residence time, attachment likelihood, and charge.

Concerning Experiment 2, what was developed is a model to predict the size-dependent confined diffusion behavior of monodisperse spherical bodies in a periodic structure. The exact geometry of the structure, including factors such as the number of holes in the iOpals' voids, plays a crucial role in the slowdown calculation. Also, as detailed in Experiment 2's treatment, the employed simulated potential needs further refinement, as does the model for the limit of point-like diffusants. As a result of these factors, in order to accurately represent diffusion in hydrogels, the method detailed in Experiment 2's treatment still needs both adjustments in the general predictive behavior model, and to be generalized to the nanometer-scale irregular, macroscopically statistical structure of hydrogels.

Finally, Experiment 3 succeeds in achieving the intended target, as detailed in its treatment. A further objective, in addition to evaluating the gels' nanometric structure and dynamics, and the gel's collapse as biosensing enhancement, is the fine tuning and engineering of hydrogel for specific applications. In a way, this constitutes reverse engineering on the gel structural inquiry part of the Experiment, in that instead of evaluating a gels' mesh size and mesh size polydispersity as dependent on preparation and environment conditions, such quantities could ideally be fine-tuned based on the accumulated knowledge of their dependency. Of course, a far more extensive body of knowledge is required in order to do this. And of course, a precise, fully quantitative mesh size and mesh polydispersity evaluation method needs to be finalized before being able to pass on such next step.

On a more imminent level, many aspects of the studied hydrogel remain to be investigated which are beyond the specific scope of this thesis. As a brief rundown, without venturing into non-PNIPAAm territory, variables to be investigated concerning the gels' structure include different chain length, different chain length polydispersity (preliminary studies of which suggest a reverse influence on a gel's homogeneity, i.e. high polydispersity leading to more homogeneous gels), alternative solvents to ethanol (believed to be able to tune a gel's pre-crosslinking structure by better/worse solvency

properties) and alternative functionalizations to enable alternative means of collapsing/swelling to thermal, and combinations thereof.

10. Acknowledgements

Dr. Jakub Dostalek

Dr. Chun-Jen Huang

PNIPAAm synthesis, sample preparation introduction,

and endless priceless interaction

Dr. Robert F. Roskamp

Additional hydrogel discussion

Dr. Annette Brunsen

Protocol refinements, interactions and mutual assistance

Dr. Robert F. Roskamp

Dr. Maria Gianneli

Dr. Annette Brunsen

Markus Plum

Biological and functionalization expertise

Dr. Sandra Ritz

Dr. Jakub Dostalek

Dr. Chun-Jen Huang

Inverse opals, SEM

Dr. Markus Retsch

Complementary projects and fruitful interactions

Dr. Thipphaya Cherdhirankorn

Abstract translation, SEM

Cornel Wolf

Moral support

Véronique Schwartz

Cornel Wolf

Sascha Pihan

Dr. Robert F. Roskamp

Dr. Annette Brunsen

Dr. Jan Dorn

Marc Großerüschkamp

Luis Duque

Luis Heritier

Julia Lips

Alexander Lotz

My mother

Dr. Fréderic Laquai

Dr. Gabriella Santonicola

Martin Heller

Dr. Shi Feng

Dr. Ann Junghans

Melanie Dröge

Dr. Slavoj Kresak

Nicolas Vogel

Daniel Klinger

Stefanie Utech

Christian Scherer

… and all those of the German Support Team who weren't mentioned here

(You know who you are)

11.   References

1.   Tanaka, T., Phase-Transitions in Gels and a Single Polymer. *Polymer* **1979,** *20* (11), 1404-1412.
2.   Schneider, B. H.; Dickinson, E. L.; Vach, M. D.; Hoijer, J. V.; Howard, L. V., Highly sensitive optical chip immunoassays in human serum. *Biosens Bioelectron* **2000,** *15* (1-2), 13-22.
3.   Vaisocherova, H.; Yang, W.; Zhang, Z.; Cao, Z. Q.; Cheng, G.; Piliarik, M.; Homola, J.; Jiang, S. Y., Ultralow fouling and functionalizable surface chemistry based on a zwitterionic polymer enabling sensitive and specific protein detection in undiluted blood plasma. *Anal Chem* **2008,** *80* (20), 7894-7901.
4.   Wark, A. W.; Lee, H. J.; Corn, R. M., Long-range surface plasmon resonance imaging for bioaffinity sensors. *Anal Chem* **2005,** *77* (13), 3904-3907.
5.   Lakhiari, H.; Okano, T.; Nurdin, N.; Luthi, C.; Descouts, P.; Muller, D.; Jozefonvicz, J., Temperature-responsive size-exclusion chromatography using poly(N-isopropylacrylamide) grafted silica. *Bba-Gen Subjects* **1998,** *1379* (3), 303-313.
6.   Kanazawa, H.; Yamamoto, K.; Matsushima, Y.; Takai, N.; Kikuchi, A.; Sakurai, Y.; Okano, T., Temperature-responsive chromatography using poly(N-isopropylacrylamide)-modified silica. *Anal Chem* **1996,** *68* (1), 100-105.
7.   Kuckling, D., Responsive hydrogel layers-from synthesis to applications. *Colloid Polym Sci* **2009,** *287* (8), 881-891.
8.   Harmon, M. E.; Kuckling, D.; Frank, C. W., Photo-cross-linkable PNIPAAm copolymers. 2. Effects of constraint on temperature and pH-responsive hydrogel layers. *Macromolecules* **2003,** *36* (1), 162-172.
9.   Kuckling, D.; Hoffmann, J.; Plotner, M.; Ferse, D.; Kretschmer, K.; Adler, H. J. P.; Arndt, K. F.; Reichelt, R., Photo cross-linkable poly(N-isopropylacrylamide) copolymers III: micro-fabricated temperature responsive hydrogels. *Polymer* **2003,** *44* (16), 4455-4462.
10.   Harmon, M. E.; Kuckling, D.; Pareek, P.; Frank, C. W., Photo-cross-linkable PNIPAAm copolymers. 4. Effects of copolymerization and cross-linking on the volume-phase transition in constrained hydrogel layers. *Langmuir* **2003,** *19* (26), 10947-10956.
11.   Kuckling, D.; Richter, A.; Arndt, K. F., Temperature and pH-dependent swelling behavior of poly(N-isopropylacrylamide) copolymer hydrogels and their use in flow control. *Macromol Mater Eng* **2003,** *288* (2), 144-151.
12.   Gianneli, M.; Beines, P. W.; Roskamp, R. F.; Koynov, K.; Fytas, G.; Knoll, W., Local and global dynamics of transient polymer networks and swollen gels anchored on solid surfaces. *J Phys Chem C* **2007,** *111* (35), 13205-13211.
13.   Schwille, P.; Bieschke, J.; Oehlenschlager, F., Kinetic investigations by fluorescence correlation spectroscopy: The analytical and diagnostic potential of diffusion studies. *Biophys Chem* **1997,** *66* (2-3), 211-228.
14.   Petersen, N. O.; Elson, E. L., Measurements of Diffusion and Chemical-Kinetics by Fluorescence Photobleaching Recovery and Fluorescence Correlation Spectroscopy. *Method Enzymol* **1986,** *130*, 454-484.

15.   Schwille, P.; MeyerAlmes, F. J.; Rigler, R., Dual-color fluorescence cross-correlation spectroscopy for multicomponent diffusional analysis in solution. *Biophys J* **1997,** *72* (4), 1878-1886.

16.   Kinjo, M.; Rigler, R., Ultrasensitive Hybridization Analysis Using Fluorescence Correlation Spectroscopy. *Nucleic Acids Res* **1995,** *23* (10), 1795-1799.

17.   Schwille, P.; Oehlenschlager, F.; Walter, N. G., Quantitative hybridization kinetics of DNA probes to RNA in solution followed by diffusional fluorescence correlation analysis. *Biochemistry-Us* **1996,** *35* (31), 10182-10193.

18.   Schuler, J.; Frank, J.; Trier, U.; Schafer-Korting, M.; Saenger, W. A., Interaction kinetics of tetramethylrhodamine transferrin with human transferrin receptor studied by fluorescence correlation spectroscopy. *Biochemistry-Us* **1999,** *38* (26), 8402-8408.

19.   Wohland, T.; Friedrich, K.; Hovius, R.; Vogel, H., Study of ligand-receptor interactions by fluorescence correlation spectroscopy with different fluorophores: Evidence that the homopentameric 5-hydroxytryptamine type 3(As) receptor binds only one ligand. *Biochemistry-Us* **1999,** *38* (27), 8671-8681.

20.   Borsch, M.; Turina, P.; Eggeling, C.; Fries, J. R.; Seidel, C. A. M.; Labahn, A.; Graber, P., Conformational changes of the H+-ATPase from Escherichia coli upon nucleotide binding detected by single molecule fluorescence. *Febs Lett* **1998,** *437* (3), 251-254.

21.   Berne, B. J.; Pecora, R., *Dynamic Light Scattering*. John Wiley & Sons: 1976.

22.   Aragon, S. R.; Pecora, R., Fluorescence Correlation Spectroscopy as a Probe of Molecular-Dynamics. *J Chem Phys* **1976,** *64* (4), 1791-1803.

23.   Widengren, J.; Mets, U.; Rigler, R., Fluorescence Correlation Spectroscopy of Triplet-States in Solution - a Theoretical and Experimental-Study. *J Phys Chem-Us* **1995,** *99* (36), 13368-13379.

24.   Schwille, P.; Kummer, S.; Heikal, A. A.; Moerner, W. E.; Webb, W. W., Fluorescence correlation spectroscopy reveals fast optical excitation-driven intramolecular dynamics of yellow fluorescent proteins. *P Natl Acad Sci USA* **2000,** *97* (1), 151-156.

25.   Schild, H. G., Poly (N-Isopropylacrylamide) - Experiment, Theory and Application. *Prog Polym Sci* **1992,** *17* (2), 163-249.

26.   Yu, H.; Grainger, D. W., Thermosensitive Swelling Behavior in Cross-Linked N-Isopropylacrylamide Networks - Cationic, Anionic, and Ampholytic Hydrogels. *Journal of Applied Polymer Science* **1993,** *49* (9), 1553-1563.

27.   Xue, W.; Hamley, I. W., Thermoreversible swelling behaviour of hydrogels based on N-isopropylacrylamide with a hydrophobic comonomer. *Polymer* **2002,** *43* (10), 3069-3077.

28.   Roskamp, R. F. Functional Hydrogels. Johan Gutenberg Universität, Mainz, 2009.

29.   (a) Beines, P. W.; Klosterkamp, I.; Menges, B.; Jonas, U.; Knoll, W., Responsive thin hydrogel layers from photo-cross-linkable poly(N-isopropylacrylamide) terpolymers. *Langmuir* **2007,** *23* (4), 2231-2238; (b) van den Brom, C. R.; Anac, I.; Roskamp, R. F.; Retsch, M.; Jonas, U.; Menges, B.; Preece, J. A., The swelling behaviour of thermoresponsive hydrogel/silica nanoparticle composites. *J Mater Chem* **2010,** *20* (23), 4827-4839.

30.   Gianneli, M.; Roskamp, R. F.; Jonas, U.; Loppinet, B.; Fytas, G.; Knoll, W., Dynamics of swollen gel layers anchored to solid surfaces. *Soft Matter* **2008,** *4* (7), 1443-1447.

31.   (a) Retsch, M.; Zhou, Z. C.; Rivera, S.; Kappl, M.; Zhao, X. S.; Jonas, U.; Li, Q., Fabrication of Large-Area, Transferable Colloidal Monolayers Utilizing Self-Assembly at the Air/Water Interface. *Macromol Chem Physic* **2009,** *210* (3-4), 230-241; (b) Li, Q.; Retsch, M.; Wang, J. J.; Knoll, W. G.; Jonas, U., Porous Networks Through Colloidal Templates. *Top Curr Chem* **2009,** *287*, 135-180.

32.   Subramanian, G.; Manoharan, V. N.; Thorne, J. D.; Pine, D. J., Ordered macroporous materials by colloidal assembly: A possible route to photonic bandgap materials. *Adv Mater* **1999,** *11* (15), 1261-+.

33.   Collier, G.; Vellore, N. A.; Latour, R. A.; Stuart, S. J., Development of molecular simulation methods to accurately represent protein-surface interactions: Method assessment for the calculation of electrostatic effects. *Biointerphases* **2009,** *4* (4), 57-64.

34.   Krotova, M. K.; Vasilevskaya, V. V.; Leclercq, L.; Boustta, M.; Vert, M.; Khokhlov, A. R., Salt Effects on Complexes of Oppositely Charged Macromolecules Having Different Affinity to Water. *Macromolecules* **2009,** *42* (19), 7495-7503.

35.   Cole, M. A.; Jasieniak, M.; Voelcker, N. H.; Thissen, H.; Horn, R.; Griesser, H. J., Switchable surface coatings for control over protein adsorption - art. no. 641606. *Biomedical Applications of Micro- and Nanoengineering III* **2007,** *6416*, 41606-41606 492.

36.   Ise, N., Like likes like: counterion-mediated attraction in macroionic and colloidal interaction. *Phys Chem Chem Phys* **2010,** *12* (35), 10279-10287.

37.   Truzzolillo, D.; Bordi, F.; Sciortino, F.; Sennato, S., Interaction between like-charged polyelectrolyte-colloid complexes in electrolyte solutions: A Monte Carlo simulation study in the Debye-Huckel approximation. *J Chem Phys* **2010,** *133* (2), -.

38.   Cherdhirankorn, T.; Retsch, M.; Jonas, U.; Butt, H. J.; Koynov, K., Tracer Diffusion in Silica Inverse Opals. *Langmuir* **2010,** *26* (12), 10141-10146.

39.   Kasianowicz, J. J.; Brandin, E.; Branton, D.; Deamer, D. W., Characterization of individual polynucleotide molecules using a membrane channel. *P Natl Acad Sci USA* **1996,** *93* (24), 13770-13773.

40.   Muthukumar, M.; Kong, C. Y., Simulation of polymer translocation through protein channels. *P Natl Acad Sci USA* **2006,** *103* (14), 5273-5278.

41.   (a) Han, J.; Craighead, H. G., Separation of long DNA molecules in a microfabricated entropic trap array. *Science* **2000,** *288* (5468), 1026-1029; (b) Nykypanchuk, D.; Strey, H. H.; Hoagland, D. A., Brownian motion of DNA confined within a two-dimensional array. *Science* **2002,** *297* (5583), 987-990.

42.   Stefani, F. D.; Knoll, W.; Kreiter, M.; Zhong, X.; Han, M. Y., Quantification of photoinduced and spontaneous quantum-dot luminescence blinking. *Phys Rev B* **2005,** *72* (12), -.

43.   Verberk, R.; van Oijen, A. M.; Orrit, M., Simple model for the power-law blinking of single semiconductor nanocrystals. *Phys Rev B* **2002,** *66* (23), -.

44.   Stefani, F. D.; Zhong, X. H.; Knoll, W.; Han, M. Y.; Kreiter, M., Memory in quantum-dot photoluminescence blinking. *New J Phys* **2005,** *7*, -.

45.   Loppinet, B.; Fytas, G.; Vlassopoulos, D.; Likos, C. N.; Meier, G.; Liu, G. J., Dynamics of dense suspensions of star-like micelles with responsive fixed cores. *Macromol Chem Physic* **2005,** *206* (1), 163-172.

46.   Likos, C. N., Effective interactions in soft condensed matter physics. *Phys Rep* **2001,** *348* (4-5), 267-439.

47.   Coughlan, F. M.; Lewis, H. J., A study of electrically conductive adhesives as a manufacturing solder alternative. *J Electron Mater* **2006,** *35* (5), 912-921.

48.   Kim, S. Y.; Lee, S. C., Thermo-responsive injectable hydrogel system based on poly(N-isopropylacrylamide-co-vinylphosphonic acid). I. Biomineralization and protein delivery. *Journal of Applied Polymer Science* **2009,** *113* (6), 3460-3469.

49.   Qiu, Y.; Park, K., Environment-sensitive hydrogels for drug delivery. *Adv Drug Deliver Rev* **2001,** *53* (3), 321-339.

50.   Lu, S. X.; Anseth, K. S., Release behavior of high molecular weight solutes from poly(ethylene glycol)-based degradable networks. *Macromolecules* **2000,** *33* (7), 2509-2515.

51.   Bromberg, L. E.; Ron, E. S., Temperature-responsive gels and thermogelling polymer matrices for protein and peptide delivery. *Adv Drug Deliver Rev* **1998,** *31* (3), 197-221.

52.   Lewis, G.; Coughlan, D. C.; Lane, M. E.; Corrigan, O. I., Preparation and release of model drugs from thermally sensitive poly(N-isopropylacrylamide) based macrospheres. *J Microencapsul* **2006,** *23* (6), 677-685.

53.   Guenther, M.; Kuckling, D.; Corten, C.; Gerlach, G.; Sorber, J.; Suchaneck, G.; Arndt, K. F., Chemical sensors based on multiresponsive block copolymer hydrogels. *Sensor Actuat B-Chem* **2007,** *126* (1), 97-106.

54.   Liu, Y.; Meng, S.; Mu, L.; Jin, G. Y.; Zhong, W.; Kong, J. L., Novel renewable immunosensors based on temperature-sensitive PNIPAAm bioconjugates. *Biosens Bioelectron* **2008,** *24* (4), 710-715.

55.   Gant, R. M.; Hou, Y. P.; Grunlan, M. A.; Cote, G. L., Development of a self-cleaning sensor membrane for implantable biosensors. *J Biomed Mater Res A* **2009,** *90A* (3), 695-701.

56.   Wang, Y.; Brunsen, A.; Jonas, U.; Dostalek, J.; Knoll, W., Prostate Specific Antigen Biosensor Based on Long Range Surface Plasmon-Enhanced Fluorescence Spectroscopy and Dextran Hydrogel Binding Matrix. *Anal Chem* **2009,** *81* (23), 9625-9632.

57.   Kopecek, J.; Yang, J. Y., Review - Hydrogels as smart biomaterials. *Polym Int* **2007,** *56* (9), 1078-1098.

58.   Knoll, W., *Handbook of Biofunctional Surfaces*. Pan Stanford Publishing: Singapore, 2010.

59.   Vidyasagar, A.; Majewski, J.; Toomey, R., Temperature induced volume-phase transitions in surface-tethered Poly(N-isopropylacrylamide) networks. *Macromolecules* **2008,** *41* (3), 919-924.

60.   Kuckling, D.; Harmon, M. E.; Frank, C. W., Photo-cross-linkable PNIPAAm copolymers. 1. Synthesis and characterization of constrained temperature-responsive hydrogel layers. *Macromolecules* **2002,** *35* (16), 6377-6383.

61.   Gianneli, M. Structure and Dynamics of Thin Anchored Hydrogel Layers by Fluorescence Correlation and Photon Correlation Spectroscopy. Johan Gutenberg Universität, Mainz, 2008.

62.   Brunsen, A. Johan Gutenberg Universität, Mainz, 2010.

63.   Zustiak, S. P.; Boukari, H.; Leach, J. B., Solute diffusion and interactions in cross-linked poly(ethylene glycol) hydrogels studied by Fluorescence Correlation Spectroscopy. *Soft Matter* **2010,** *6* (15), 3609-3618.

64.   Zustiak, S. P.; Leach, J. B., Hydrolytically Degradable Poly(Ethylene Glycol) Hydrogel Scaffolds with Tunable Degradation and Mechanical Properties. *Biomacromolecules* **2010,** *11* (5), 1348-1357.

65.   Canal, T.; Peppas, N. A., Correlation between Mesh Size and Equilibrium Degree of Swelling of Polymeric Networks. *J Biomed Mater Res* **1989,** *23* (10), 1183-1193.

66.   Chalal, M.; Ehrburger-Dolle, F.; Morfin, I.; Vial, J. C.; de Armas, M. R. A.; Roman, J. S.; Bolgen, N.; Piskin, E.; Ziane, O.; Casalegno, R., Imaging the Structure of Macroporous Hydrogels by Two-Photon Fluorescence Microscopy. *Macromolecules* **2009,** *42* (7), 2749-2755.

67.   Han, J.; Ruan, R. R.; Park, C. H., Prediction of Hydrogel Pore-Size by Pulse Nmr and Neural Networks. *Biotechnol Tech* **1995,** *9* (9), 637-642.

68.   Seiffert, S.; Oppermann, W., Diffusion of linear macromolecules and spherical particles in semidilute polymer solutions and polymer networks. *Polymer* **2008,** *49* (19), 4115-4126.

69.   Ikkai, F.; Shibayama, M., Inhomogeneity control in polymer gels. *J Polym Sci Pol Phys* **2005,** *43* (6), 617-628.

70.   Junk, M. J. N.; Jonas, U.; Hinderberger, D., EPR spectroscopy reveals nanoinhomogeneities in the structure and reactivity of thermoresponsive hydrogels. *Small* **2008,** *4* (9), 1485-1493.

71.   Aulasevich, A.; Roskamp, R. F.; Jonas, U.; Menges, B.; Dostalek, J.; Knoll, W., Optical Waveguide Spectroscopy for the Investigation of Protein-Functionalized Hydrogel Films. *Macromol Rapid Comm* **2009,** *30* (9-10), 872-877.

72.   Wang, Y.; Huang, C. J.; Jonas, U.; Wei, T. X.; Dostalek, J.; Knoll, W., Biosensor based on hydrogel optical waveguide spectroscopy. *Biosens Bioelectron* **2010,** *25* (7), 1663-1668.

73.   (a) Suzuki, A.; Wu, X. R.; Kuroda, M.; Ishiyama, E.; Kanama, D., Swelling properties of thin-plate hydrogels under mechanical constraint. *Jpn J Appl Phys 1* **2003,** *42* (2A), 564-569; (b) Toomey, R.; Freidank, D.; Ruhe, J., Swelling behavior of thin, surface-attached polymer networks. *Macromolecules* **2004,** *37* (3), 882-887; (c) Tokarev, I.; Minko, S., Stimuli-responsive hydrogel thin films. *Soft Matter* **2009,** *5* (3), 511-524.

74.   Harmon, M. E.; Jakob, T. A. M.; Knoll, W.; Frank, C. W., A surface plasmon resonance study of volume phase transitions in N-isopropylacrylamide gel films. *Macromolecules* **2002,** *35* (15), 5999-6004.

75.   Cherdhirankorn, T.; Best, A.; Koynov, K.; Peneva, K.; Muellen, K.; Fytas, G., Diffusion in Polymer Solutions Studied by Fluorescence Correlation Spectroscopy. *J Phys Chem B* **2009,** *113* (11), 3355-3359.

76.   Tien, P. K., Integrated-Optics and New Wave Phenomena in Optical-Waveguides. *Rev Mod Phys* **1977,** *49* (2), 361-420.

77.   Smith, R. E.; Houdewalter, S. N., Leaky Guiding in Nontransparent Wave-Guides. *J Opt Soc Am A* **1995,** *12* (4), 715-724.

78.   Schasfoort, R. B. M.; A.J., T., *Handbook of Surface Plasmon Resonance*. RSC Publishing.

79.   Horn, N.; Kreiter, M., Plasmon Spectroscopy: Methods, Pitfalls and How to Avoid Them. *Plasmonics* **2010**.

80.   Pochi, Y., *Optical waves in layered media*. Wiley: 1988.

81.   Karthe, W.; Müller, R., *Integrierte Optik*. Akademische Verlagsgesellschaft Geest & Portig: Leipzig, Germany, 1991.

82.   Zettl, U.; Hoffmann, S. T.; Koberling, F.; Krausch, G.; Enderlein, J.; Harnau, L.; Ballauff, M., Self-Diffusion and Cooperative Diffusion in Semidilute Polymer Solutions As Measured by Fluorescence Correlation Spectroscopy. *Macromolecules* **2009,** *42* (24), 9537-9547.

83.   Saalwachter, K., Proton multiple-quantum NMR for the study of chain dynamics and structural constraints in polymeric soft materials. *Prog Nucl Mag Res Sp* **2007,** *51* (1), 1-35.

84.   Saalwachter, K.; Kleinschmidt, F.; Sommer, J. U., Swelling heterogeneities in end-linked model networks: A combined proton multiple-quantum NMR and computer simulation study. *Macromolecules* **2004,** *37* (23), 8556-8568.

85.   Asnaghi, D.; Giglio, M.; Bossi, A.; Righetti, P. G., Quasi-ordered structure in highly cross-linked poly(acrylamide) gels. *Macromolecules* **1997,** *30* (20), 6194-6198.

86.   Junk, M. J. N.; Anac, I.; Menges, B.; Jonas, U., Analysis of Optical Gradient Profiles during Temperature- and Salt-Dependent Swelling of Thin Responsive Hydrogel Films. *Langmuir* **2010,** *26* (14), 12253-12259.

87.   Anac, I.; Aulasevich, A.; Junk, M. J. N.; Jakubowicz, P.; Roskamp, R. F.; Menges, B.; Jonas, U.; Knoll, W., Optical Characterization of Co-Nonsolvency Effects in Thin Responsive PNIPAAm-Based Gel Layers Exposed to Ethanol/Water Mixtures. *Macromol Chem Physic* **2010,** *211* (9), 1018-1025.

88.   Afroze, F.; Nies, E.; Berghmans, H., Phase transitions in the system poly(N-isopropylacrylamide)/water and swelling behaviour of the corresponding networks. *J Mol Struct* **2000,** *554* (1), 55-68.

12. Curriculum Vitae

Name: Riccardo Raccis
Place of birth: Florence, Italy
Date of birth: December 19th 1979
Address: Richard-Schirrmann-Strasse 14, apt. 256, 55122 Mainz, Germany
Italian fiscal code: RCCRCR79T19D612K
Member of: MPIP, IMPRS program
PhD student: at the Faculty of Physics, Mathematics and Informatics of the Johannes Gutenberg-Universität Mainz since December 20th 2007. Matriculation number: 2662149

Formation and Scientific Career:
- Scientific High School, with experimental orientation. High school diploma in 1998.
- Master's Degree in Physics, specialization in Material Physics, obtained on March 20th 2007, with a research thesis within a joint project of the Department of Physics of the University of Florence, Institute of Anatomy of the University of Florence and CNR, and within the activities of the CNISM consortium (www.fis.uniroma3.it/cnism). The thesis' title is "Study of the structure of fragments of the protein, β-connectin via dynamic light scattering". Article available at:
  http://scitation.aip.org/getabs/servlet/GetabsServlet?prog=normal&id=PLEEE8000077000002021910000001&idtype=cvips&gifs=yes
- Since October 1st, 2007 working at the MPIP. Assigned to studying the structure and dynamics of water-swollen hydrogels (PNIPAAm-based) via Fluorescence Correlation Spectroscopy. Project branched to include:
  - Hydrogel characterization at the nanoscale
  - Hydrogel functionalization and subsequent characterization
  - Dye-gel chain interaction effects in a solution
  - Implementation of quantum dots as FCS probes
  - Particle diffusion in inverse opals and theory development of size-dependent slowdown effects in a regular network

Master's Degree specialization: academic career specifically structure-oriented, including:
- Low Temperature Physics
- Atomic Physics
- Solid State Physics
- Specialization in Liquid Physics (soft matter Physics, complex liquids, micelles, polymer suspensions)
-

Attended Master's Degree courses:
- Mathematical Analysis I
- Physics Experimentation I
- General Physics I
- Geometry
- Mathematical Analysis II
- General and Inorganic Chemistry
- Physics Experimentation II
- General Physics II
- Rational Mechanics with Statistical Mechanics Elements
- Physics Experimentation III
- Nuclear and Sub Nuclear Physics Institutions
- Theoretical Physics Institutions
- Mathematical Methods of Physics
- Structure of Matter
- Atomic Physics
- Liquid Physics
- Low Temperature Physics
- Solid State Physics
- Material Physics Laboratory

Attained skills:
- **Master's Degree:**
    - Use of: laser light sources; light intensity detectors; digital correlators; refractometers; spectrometers
    - Light scattering: both dynamic (Photon Correlation Spectroscopy, PCS) and static
    - Analysis techniques of correlation functions (fitting, cumulants expansion, CONTIN algorithm)
    - Organic samples management
    - Water and sample cleaning
    - Cleaning and sanitizing of laboratory material
    - Statistical analysis of data
    - Electrical and logical circuits; fundaments of electronics
    - Problem solving
- **PhD work:**
    - Fluorescence Correlation Spectroscopy (FCS)
    - Preparation of hydrogels: sonic cleaning, functionalization of glass, spin-coating, cross-linking, annealing, functionalization of gel
    - Depulverization via acetone fountains, vacuum oven
    - Fundaments of Surface Plasmon Resonance
    - Antibody management
    - Fluorescent protein management
    - Dialysis

- o IR spectroscopy
- o UV-VIS spectroscopy
- o Theory modelling and reengineering

Publications:
- **Master's Degree:**
  - o Marchetti, S.; Sbrana, F.; Raccis, R.; Lanzi, L.; Gambi, C. M. C.; Vassalli, M.; Tiribilli, B.; Pacini, A.; Toscano, A., Dynamic light scattering and atomic force microscopy imaging on fragments of beta - connectin from human cardiac muscle. *Physical Review E* **2008**, 77 (2), 021910
- **PhD work:**
  - o Three in preparation, concerning the three experiments detailed in the thesis

Known languages:
- Excellent English knowledge, both written and spoken (8 years of study, 5 of which with a mother tongue teacher, and constant social interactions on an international level)
- German: learning in progress
- Italian mother tongue

Informatic knowledge:
- Microsoft Office package (high)
- Microsoft Frontpage (high)
- Origin (high)
- Brookhaven autocorrelation analysis package (high)
- Great ease with graphic tools like Photoshop, Paint Shop Pro
- Excellent ease to familiarize and rapidly learn the use of new software

Telephone numbers:
(+49) 15115774389
(+39) 3280824062

Email address: raccis@gmail.com